Design and Optimization Studies of Electroabsorptive and Carrier Injective Microring Resonators for Optical Switching and Logic Gate Applications

A thesis submitted

in partial fulfillment for the award of the degree of

Doctor of Philosophy

by

Fayza K A

Department of Avionics

Indian Institute of Space Science and Technology

Thiruvananthapuram, India

June 2022

Certificate

This is to certify that the thesis titled ***Design and Optimization Studies of Electroabsorptive and Carrier Injective Microring Resonators for Optical Switching and Logic Gate Applications*** submitted by **Fayza K A**, to the Indian Institute of Space Science and Technology, Thiruvananthapuram, in partial fulfilment for the award of the degree of **Doctor of Philosophy** is a bona fide record of the original work carried out by her under my supervision. The contents of this thesis, in full or in parts, have not been submitted to any other Institute or University for the award of any degree or diploma.

Dr. Sooraj Ravindran
Associate Professor
Dept of Avionics, IIST
Thiruvananthapuram, India

Dr. Deepak Mishra
Head of Department
Dept of Avionics, IIST
Thiruvananthapuram, India

Place: Thiruvananthapuram
Date: June 2022

Declaration

I declare that this thesis titled ***Design and Optimization Studies of Electroabsorptive and Carrier Injective Microring Resonators for Optical Switching and Logic Gate Applications*** submitted in partial fulfilment for the award of the degree of **Doctor of Philosophy** is a record of the original work carried out by me under the supervision of **Dr. Sooraj Ravindran**, and has not formed the basis for the award of any degree, diploma, associateship, fellowship, or other titles in this or any other Institution or University of higher learning. In keeping with the ethical practice in reporting scientific information, due acknowledgments have been made wherever the findings of others have been cited.

Place: Thiruvananthapuram
Date: June 2022

Fayza K A
(SC16D012)

This thesis is dedicated to my parents, Sanoop and Rahyl Sanoop.

Acknowledgements

I would like to express my greatest gratitude to my research advisor and mentor, Dr. Sooraj R, for his supervision, continuous support and timely guidance. He is such an amazing supervisor who not only steered my research works in right direction but also influenced me to grow as a better person in life. His openness to share knowledge, providing me the freedom to develop my own ideas in the area of research, responding patiently even to my fundamental questions has helped me at many stages of my research. His abiding faith in my efforts and skills helped me to complete my dissertation. I really admire his vibrant, humble and optimistic attitude, which always provided immense motivation for me.

I would also like to thank all the members in my doctoral committee, Prof. Srinivas Talabattula, Prof. Manoj B.S, Dr. Deepak Mishra, Dr. Solomon Ivan and Dr. Vineeth B.S for their suggestions, feedbacks and support during annual reviews. I acknowledge Prof. Srinivas Talabattula, IISc, for his valuable advice and providing me the simulation facilities at IISc Photonics lab. I thank Dr. Deepak Mishra, Head of Avionics department, Prof. Manoj B.S, former head of Avionics department for providing an invigorating research environment. I express my thanks to Dr. Vinay Kumar Dhadwal, the Director and Dr. K.S. Dasgupta, the former Director for their support. I express my gratitude to IIST for providing the fellowship during my research period. I am thankful to Prof. Pramod Gopinath and Dr. Seena V for worthful advices. I also owe to Prof. Narayanamoorthy, Prof. Raju K George, Dr. Palash Kumar Basu, Dr. Sakthivel, Dr. Umesh Kadhane and Dr. Jinesh K B for their lectures which helped me to strengthen several concepts related to my research work. I deeply thank Dr. Meena Dasan, she enlightened me the first glance of research and provided great inspiration.

This accomplishment would not have been possible without the encouragement and support from my family and friends. I am grateful to my parents who taught me the importance of education. I would like to give a profound gratitude to my mother, Rabiya P K, for her unconditional love, support, encouragement. She is the strongest woman I ever met in my life and I dedicate all my achievements to my mother. I owe to my father, Mohammedkutty, for what I am today. I also thank my in law parents, Liyakkath Alikhan and Shilaja Banu, for their support to complete my dissertation. I am indebted to my siblings, Fazil and Farzana for their love, support and prayers.

I am grateful to my brothers and sisters for their care and support. I am thankful to my dear Anfas for giving me happiness throughout my life. Mema always loves you to the moon and back. I am grateful to Minichechi and Deepachechi for inspiring me and being my wonderful teachers. I thank all my teachers at different stages of my education. My heartfelt thanks to my amazing friends Soumya, Anupama, Namitha, Praveen, Manu, Tina and Akshaya for their love, care, moral support during my toughest periods, joyful rides and for making my research life so much enjoyable and memorable. I thank Yadhunath, Hajara and Kripa for their support. I would like to express my gratitude to everyone who knowingly or unknowingly helped me for the successful completion of my research. I thank the Almighty for the blessings bestowed upon me.

I owe to the deepest love, tremendous encouragement, immense support and sacrifice shown by my dearest better half and my best friend, Mr. Sanoop.V.L. I am blessed to have him for enlightening my life, to motivate and cherish me when I am down. Thank you for always being there for me as my greatest strength and shield. Last but foremost, I thank with love to my son, Rahyl Sanoop.

Fayza K A

Abstract

Optical interconnects are the promising solution to the drawbacks of electrical interconnects in integrated circuits (ICs). The demand for higher packaging density in ICs along with large bandwidth and high speed signal processing requirements can be satisfied by microring resonators (MRRs), which can act as modulator/switch and signal processing unit in optical interconnects. This thesis mainly focus on the design and optimization studies of MRRs based optical switches/modulators and optical logic gates with electroabsorption (EA) and carrier injection (CI) as the modulation mechanisms. EA and CI modulation mechanisms varies the absorption and refractive index of the light guiding region in the MRR configurations with respect to the applied bias and results in optical switching by shifting the resonant wavelength. The proposed group III-V semiconductor MRR switches/modulators are highly compatible for integration with other optoelectronic devices.

Optical switches in optoelectronic ICs demands for small footprinted devices which can provide with high contrast ratio (CR) and low insertion loss (IL) at low drive fields in optical window regime. We propose an approach to optimize the performance of resonant wavelength switching in quantum confined stark effect (QCSE) based double ring resonator. The waveguides of MRR are configured as p-i-n diode structure. Multiple InGaAsP/InP quantum wells (QWs) incorporated in the intrinsic region of MRR structure varies absorption in accordance with applied field and introduces switching. Our analysis on the proposed EA MRR portrays the dependency of switching performance characteristics over ring resonator coupling coefficients, applied field and operating wavelength quite apart from QW parameters. Performance analysis on conventional QW based EA modulator points out that the wider QWs attains higher absorption change with applied field and leads to better ON-OFF ratio at the output. However, the results in this thesis reveals that the QCSE based MRR optical switches can achieve higher CR for narrow wells by optimizing ring resonator parameters and operating wavelength.

The implementation of directed logic gates using EA and CI based p-i-n diodes embedded in the waveguiding regions of optical MRR is proposed and analysed. The optical logic gates are realized by representing the operands as the applied bias on the rings while the operation results of logic gates appears as in the form of light intensities at the output

ports of MRR. The light guiding core region of EA based MRR logic gate configuration is composed of InGaAsP/InP QWs and the cladding is made of InP. However, the intrinsic region in CI based MRR gate configurations are made of bulk GaAs with AlGaAs as the p and n type barriers to obtain refractive index variation due to bandfilling, bandgap shrinkage and free carrier absorption effects. The proposed configurations are optimized (in terms of coupling coefficient, operating wavelength and applied field) to achieve better performance in logic operations such as AND, OR, NAND, XOR, XNOR, Fredkin and inhibitor gates. EA modulation mechanism fails to implement OR and NOR gates on a parallel MRR configuration due to significant Q-factor reduction as the absorption increases with applied field is also investigated and the same configuration successfully realizes OR and NOR gate based on CI mechanism. A novel triple ring resonator configuration is proposed which can simultaneously realize optical OR and AND or NAND and NOR gates at the output ports. We propose CI based off axis MRR configuration to realize inhibitor logic gates and the dependency of output port intensities on the coupling coefficients and wavelength is optimized for performance enhancement.

We also analyze the dynamic behaviour of GaAs based p-i-n diode configured single MRR modulator with bias assisted CI as modulation mechanism. The output of the proposed MRR depends on the time dependent nature of injected carriers and resulting refractive index variations relative to the external applied voltages on the ring. Modulation characteristics depends on the electrical performance of p-i-n structure used in MRR to implement the bias. Transient response of p-i-n during turn ON and turn OFF is considered to analyze the overall performance of MRR modulator for high bit rate operations. We demonstrate numerically that the bit rate is limited by the time dependent behaviour of injecting carriers into intrinsic region through which light propagates. A deviation from expected output spectrum is observed when certain non-resonant wavelengths passes through this proposed modulator configuration and exhibits resonant characteristics during the switching transient period. Our analysis can provide a guide for suitable selection of operating wavelength by considering limitations imposed by carrier dynamics on modulator with wavelength division multiplexed signal as the input to the bus waveguide. We also depicts the dependency of applied field and coupling factors over rise time, fall time transients and memory effect of ring resonator over transmitted bits.

Contents

List of Figures

List of Tables

Abbreviations

IC	Integrated circuit
MRR	Microring resonator
SRR	Single ring resonator
DRR	Double ring resonator
EA	Electroabsorption
CI	Carrier injection
MQW	Multiple quantum well
QCSE	Quantum confined stark effect
FCA	Free carrier absorption
BF	Bandfilling
BGS	Bandgap shrinkage
FK	Franz Keldysch
CR	Contrast ratio
IL	Insertion loss
KK	Kramers Kronig
T port	Throughput port
D port	Drop port

Nomenclature

c	Speed of light
ω	Angular frequency
α	Absorption coefficient
n	Refractive index
τ	Transmission coefficient
κ	Coupling coefficient
Γ	Confinement factor
λ	Wavelength
R	Radius
ϕ	Phase
n_{eff}	Effective refractive index
F	Applied field
L_w	Well width
L_b	Barrier width
i-	Intrinsic
τ_1	Ring round trip time

Chapter 1

Introduction

Interconnects serve as the connecting elements between different components in integrated circuits. Device integration and interconnection strategy in a system determines the quality of service. Most of the existing interconnects are in electrical domain and are fabricated using the materials like Cu, Ag, Poly Si etc. Electrical interconnects fail to keep pace with device level developements in the chips because of the problems like failing to satisfy high bandwidth requirement, speed limitation, need for clock resynchronization, losses at high frequencies, electromagnetic interference, cross talk, power dissipation, skin effect, electromigration etc. As per Moore's law, advances undergoing in ICs to reduce the dimensions along with cost effective and faster performance. Greater integration complicates the interconnection networks further and cause reduced interconnection capacity [2]. This bottleneck scenario compel to focus on the performance of interconnection medium rather than the devices at either ends. Even International Technology Roadmap of semiconductors (ITRS) announced that the electrical interconnects as the major hindrance in the path of IC performance in semiconductor industry [3]. The quote 'It is like making cheaper, faster car but you can't go any faster on the roads' by David Miller, clearly suits to the current status of electrical interconnect in chip architecture [4]. The disadvantages of metal based electrical interconnect are clearly depicted in Figure 1.1 which shows the variation in figure of merits of interconnects with respect to scaling [1]. ILD and IMD represents interlayer dielectric and intermetal dielectric [5].

One of the trend going on to overcome this interconnect performance crisis is to change the physical means of interconnections by replacing electrical interconnects with optical interconnects [6, 7, 8, 9]. Photonic technology system can overcome the challenges faced by Moore's law well beyond the time when the device dimension scaling becomes impractical. The demand for high bandwidth for high performance computing systems can be met by optical interconnects [10]. Optical interconnects offers advantages like high

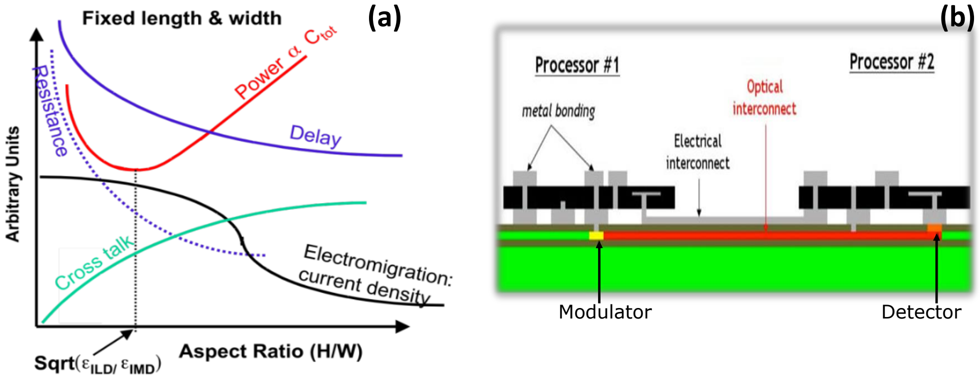

Figure 1.1: (a) Performance analysis plots of metal based electrical interconnnects with respect to aspect ratio [1]. (b) Schematic representation of On chip electrical and optical interconnect [**?**].

bandwidth, large data carrying capacity, high speed performance, real time configurability, low latencies, reduced power consumption, low loss at high frequencies, fault tolerance, no electromagnetic interference, absence of skin effect and electromigration effect etc. Resynchronization is not required for clock signal distribution because of low latencies and arrival time is reliable and predictable in optical interconnects. These characteristics of optical interconnects support dense packaging density in ICs and performance enhancement. Implementing wavelength division multiplexing (WDM) functionality on the optical devices of optical interconnects results in bandwidth density improvement [11]. Parallel computational efficiency is another major attracting feature of optical interconnects which increase the aggregate computing power of the systems.

The layout architecture of on-chip optical interconnect is shown in Figure 1.2, which carry out light generation, modulation, manipulation, amplification and detection [1]. Data is transferred from one logic module of the processor to the other through optical means. The electrical signal from the logic module will act as the driving input signal for the optical modulator/switch [12]. Optical modulator modulates the incoming laser signal according to drive signal by altering the properties like intensity, phase etc. An optical switch selectively switches the spatial or angular location based on drive signal. The optical output from modulator/switch is propagated through the waveguide or free space and routed towards the detector. The detected signal is amplified and reaches at the other logic module. The criti-

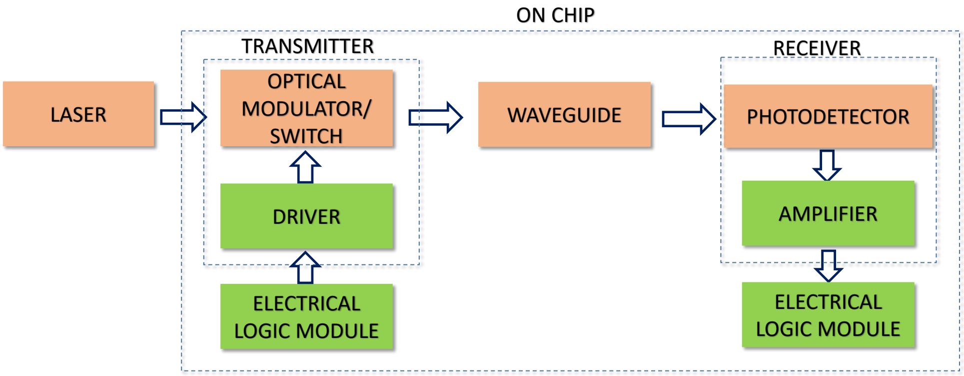

Figure 1.2: Block diagram of optical interconnect on chip architecture

cal issue facing by optical interconnect is the monolithic integration possibility with silicon VLSI chips. Nowadays, significant advanced fabrication technologies are available to grow GaAs substrate (for photonic components) over Si substrate [13, 14]. Optical interconnects can be leveraged to boost across the ranges of scales from global telecommunication industries to buses and clock distribution in high performance computing systems by proper selection of optical components in its layout architecture.

The distance×bandwidth/power of optical interconnect is around 25 times higher than electrical interconnect when the optical component used operates at 20Gb/s and is around 3.7 times higher than electrical interconnect when the optical components used operates at 10Gb/s [**?**]. Introducing wavelength division multiplexing (WDM) technology to the optical interconnect architecture can significantly improve the bandwidth of the system [**?**]. Figure 1.3 compares the bandwidth density of electrical interconnect with optical interconnect with and without WDM technology at different technology nodes. In the figure, the optical interconnect with WDM is initially having one channel in the waveguide at 90nm technology node, which is increased at the rate of four channels at each later technology nodes [**?**]. For interchip distances less than one meter, optical interconnect can accommodate THz bandwidth while only GHz bandwidth regime is attained by electrical interconnect [**?**]. The bandwidth of optical interconnect is not affected by increase in optical data path length due to insignificant attenuation unlike electrical interconnect in which increase in propagation path length results in reduced bandwidth.

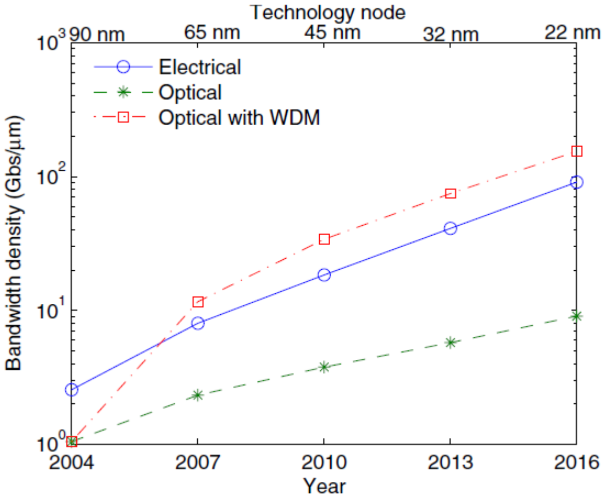

Figure 1.3: Bandwidth density of electrical and optical interconnect (with and without WDM technique) in different technology nodes [**?**].

1.1 Motivation

Optical modulator/switch plays a critical role in optical interconnect architecture (refer Figure 1.2). Optical modulators are classified based on their structures, modulation mechanisms, materials used and so on. Electro optic, electro absorption (EA), thermo optic, acousto optic, magneto optic etc are examples of the modulation mechanisms used in optical switching techniques. The optical modulator configurations are Mach-Zehnder interferometers (MZI), directional coupler waveguides, liquid crystals, cavities, plasmonics etc. The major materials used for the fabrication of optic switches are III-V semiconductors, lithium niobate ($LiNbO_3$), Si, Nitrobenzene etc. The major challenge of the conventional modulators like Mach-Zehnder modulator, directional coupler type modulator, EA ON-OFF modulators for using in chip architecture are their bulky nature (around few mm), inadequate sensitivity and low performance efficiency. Microring resonator (MRR) is attracting growing interest to act as a modulator and signal processing unit due to resonant nature, very small footprint, high speed operation, narrow band filtering effect, versatility, high Q factor, higher sensitivity and compactness. Another interesting benefits of MRR to be used as optical modulator in optoelectronic integrated circuits (OEIC) are low capacitance, low driving voltage and can be even configured as WDM filters to attain higher bandwidth operation [15, 16, 17]. Cascaded MRR modulators can enable independent wavelength modulation in WDM interconnection systems due to its wavelength dependent resonant nature. The ring resonator modulators can modulate light at specific wavelengths (the resonant wavelengths of the ring resonators) and allow all other wavelengths to bypass through the modulators without been affected. As MRR can work simultaneously as a modulator and a switch, conventional electronic switches are not required which causes network traffic and increased overall system cost due to optical-electrical-optical conversions of incoming optical signal. All these unique features of MRR configured modulators along with light confining structure suits perfectly to integrate in optical interconnect architecture. Light confined resonating structure are capable of enhancing the effect of refractive index change. In contrast to single pass devices like MZM, the resonant wavelength light travels multiple round trip through the ring resonator and interacts with the carriers repeatedly leading to low input drive power consumption because of lower carrier concentration requirement to obtain higher refractive index change. The technological progress achieved in electronic-photonic integration using MRRs spotlighted the optical interconnects as an appealing alternative to electrical interconnects.

MRR modulators can be classified based on order of rings and bus waveguides, incorporated modulation mechanism and plane of geometry arrangements. The modulator made up of materials like Si, $LiNbO_3$ are not compatible for integration with photonic components (like source, detectors, optical amplifiers etc which are mainly made up of III-V semiconductors). Despite to a large research effort has been invested for Si based optical source [18, 19], developing a promising performance along with process simplicity is seriously lagged behind that of III-V optical sources and also the modulation efficiency of Si modulators is inappreciable. Group III-V semiconductor based MRR modulators are highly recommended for monolithic integration feasibility in OEIC. Among the different modulation schemes applied on MRR, Quantum confined stark effect (QCSE) and carrier injection (CI) modulation mechanisms based MRR modulators has the potential to work efficiently using group III-V semiconductors in hybrid integrated systems. QCSE based ring resonator modulators have the potential for high frequency operation, higher sensitivity, low power consumption, compact size and facile resonance tunability. Major benefits of CI based MRR are polarization independent operation, large refractive index change, higher modulation depth, ability to work in low attenuation window using abundantly available fabrication matured III-V compounds, absence of limitation in operating wavelength selection. The p-i-n configured EA and CI MRR modulator can achieve light confinement feature and high speed operation, where the launched optical signal will be propagated through the intrinsic region. Design optimizations of MRR parameters, operating wavelength, applied bias are required to achieve performance enhancement in EA and CI MRR based modulators.

Logic gates are the building blocks in signal processing unit. EA and CI MRRs configured logic gates are significant in ICs with operands in electrical domain and operational output obtained in optical domain. Realization and optimization of these types of logic gates are required for successful implementation in ICs. Time dependent carrier dynamics studies help to understand the chirping and switching transients in CI MRR modulator rather than steady state analysis.

1.2 Objectives

The goals of this research are classified into three domains. Firstly, to focus on the parametrical optimization of QCSE based double ring MRR optical switches to attain high contrast ratio (CR) and low insertion loss (IL) at the output ports. The considered optimizing parameters are the coupling coefficient between ring-bus waveguides, ring radius, operating wavelength and QW properties like width and composition.

The second aspect is to design and optimize the performance of EA and CI based MRR configured logic gates. The realized logic gates using EA based mechanism include Buffer, NOT, Fredkin, AND, NAND, XOR and XNOR gates. While along with all the mentioned gates, OR and NOR gates are additionally realized using CI mechanism based MRR configurations. A novel MRR configuration to simultaneously realize OR and AND gates by EA mechanism, OR and AND/NAND and NOR gates by CI mechanism is also designed and optimized. The failure of OR and NOR gate realization in parallel MRR configuration is studied. Off axis MRR configuration is designed to realize inhibitor gates (NOT+OR and NOT+AND) with CI as the modulation mechanism.

The third objective is the transient performance analysis on a CI modulation based single MRR optical switch in a WDM system. Mathematical modelling and designing in time domain is conducted to study the rise and fall time transient behaviour and corresponding chirping effects in the modulator.

1.3 Thesis outline

Chapter 1 of this thesis describes the motivation and objectives of the research. An overview of the role of MRR in optical interconnects is discussed. A review about the theory, principle of operation, performance parameters, applications and types of MRR is presented in **Chapter 2**. Design and optimization studies of EA based double ring resonator optical switches is discussed in **Chapter 3**. We discuss the incorporation of QCSE into MRR operation and corresponding influence at the output port intensities. **Chapter 4** and **Chapter 5** deals with importance of hybrid electro-optical logic gates for signal processing in ICs. We design and optimize EA and CI modulation mechanism based MRR configured logic gates. The failure of OR and NOR gate realization using parallel EA double ring configuration is discussed and a novel configuration to realize OR and AND gate simultaneously using EA and CI based MRRs is introduced. The transient performance analysis of CI single MRR modulator in WDM system is mathematically modelled and analysed in **Chapter 6** for proper selection of WDM input wavelengths without resulting chirping at the modulated outputs. **Chapter 7** summarizes the accomplishments of this research and is followed by references.

Chapter 2

Microring resonators: features and functionalities

2.1 Introduction

In this chapter, the operational principle along with the features and functionalities of microring resonator is discussed. Microring resonators (MRRs) used in optical interconnect architecture have the potential to satisfy the demand for high performance computing and processing paradigm in integrated circuits. Analytical method based on node and loop field equations in MRR configurations are performed for investigating the operation, transfer functions and corresponding spectral response of the MRR switches/modulators.

2.2 Principle of operation of MRR

The idea of light transmission through ring resonator and its analysis was first proposed by Marcatili from Bell labs in 1969 [20]. Earlier to this invention, Rayleigh developed theories about whispering gallery waves in early 1900s which laid the foundation for invention and exploration of optical ring resonator structures. Optical resonators are optical cavities which are capable to exhibit discrete frequency resonances along with versatile and compact nature. An optical resonator mainly consists of closed shaped waveguides which can loop back on itself and are closely coupled to straight bus waveguides. The bus waveguides introduce and extracts lights in resonator through coupling mechanism. The closed shaped optical waveguide can be of ring, racetrack, disk and sphere shapes. Resonance occurs when the whole number of propagating wavelength equals to the optical path length of the resonator. This leads to the phenomenon of supporting only a set of frequencies of light to propagate through the resonating structure. A resonator is defined as a closed volume which ideally have zero loss and highly reflecting surface, generates standing waves at particular frequencies. The optical resonator can act as a photon reservoir. The optical resonator can have any closed shapes like ring, disk, or sphere. A microring resonator (MRR) has a ring shaped resonator with the device dimensions in the range of micrometer. The bus waveguides in the MRR provides access to the resonating ring structure and helps to supply or extract energy from the ring resonator waveguide. The launched optical signal at the input port of MRR gets propagated through the waveguides by TIR phenomenon. When the optical signal reaches at the coupling region (where the bus waveguide and closed loop waveguide of MRR are in close proximity), the optical signal undergoes evanescent coupling and a part of the optical signal from the bus waveguide gets coupled to the closed loop waveguide. The multiple circulation of the coupled optical signal occurring in the closed loop waveguide can lead to interference with the existing coupled optical signal in the loop. If MRR satisfies resonant condition (ring circumference is an integer multiple of launched signal wavelength), the interfering optical signal will be in same phase and results in constructive interference at closed loop waveguide.

The working principle behind the optical resonators are total internal reflection (TIR), evanscent coupling or frustated TIR and interferences. The launched optical signal at the input port of MRR gets propagated through the waveguides by TIR phenomenon. When the optical signal reaches at the coupling region (where the bus waveguide and closed loop waveguide of MRR are in close proximity), the optical signal undergoes evanescent coupling and a part of the optical signal from the bus waveguide gets coupled to the closed loop waveguide. The multiple circulation of the coupled optical signal occurring in the closed loop waveguide can lead to interference with the existing coupled optical signal in the loop. If MRR satisfies resonant condition, the interfering optical signal will be in same phase and results in constructive interference at closed loop waveguide. The basic structure of an optical waveguide consists of core and cladding regions. The light propagates through the high refractive indexed core while low refractive indexed cladding provides the necessary optical confinement. The light propagation through the core region of optical waveguide occurs when the incident light satisfies TIR conditions. Snell's law in ray optics gives the degree of refraction undergone by light at the boundary between two media by relating the angle of incidence and angle of refraction. When light propagates from a denser to rarer medium (core (n_1) to cladding(n_2)) with angle of incidence (θ_i) greater than critical angle (θ_c), the light reflects back to denser medium and results in TIR phenomenon. Figure 2.1 shows the TIR in an optical waveguide resulting in light guidance through the core region

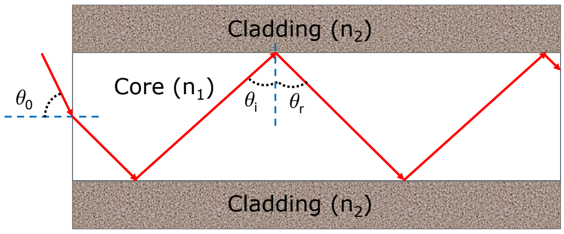

Figure 2.1: Light propagation through a waveguide based on TIR with n_1 and n_2 as the refractive index of core and cladding ($n_1 > n_2$).

where the angle of reflection is denoted as (θ_r). The acceptance angle (θ_a) determines the range of angles by which light enters into the waveguide from the surrounding media (refractive index as n_0) to undergo TIR inside the core. Critical angle and acceptance angle can be expressed as

$$\theta_c = \sin^{-1}(n_2/n_1) \tag{2.1}$$

$$\theta_a = \sin^{-1}\sqrt{(n_1^2 - n_2^2)}/n_0 \tag{2.2}$$

It is observed that under ordinary conditions, evanescent waves transmits zero net energy at the interface of two media (medium 1 and medium 2). But the evanescent waves behaves differently when a third medium (medium 3) with a refractive index greater than medium 2 is placed in close proximity to the boundary of medium 1 and medium 2. The evanescent waves transmits energy to the medium 3 through medium 2 and the phenomenon is termed as evanscent coupling. It is similar to quantum tunnelling effect. Evanescent coupling occurs in optical resonators resulting in light coupling between closed loop waveguide-bus waveguide (medium 1 and medium 3) and in between closed loop waveguides (medium 1 and medium 3) with the intermediate medium (medium 2) as the material filled in the gap between the waveguides. Constructive interference occurs in closed loop waveguide of optical resonators during on resonance condition while destructive interference occurs during off resonance.

For the present thesis work, we are considering only ring structured optical resonators as they deals with single mode while disk resonators supports multimode propagation. The ring shaped optical resonators with typical device dimensions of μm range is named as

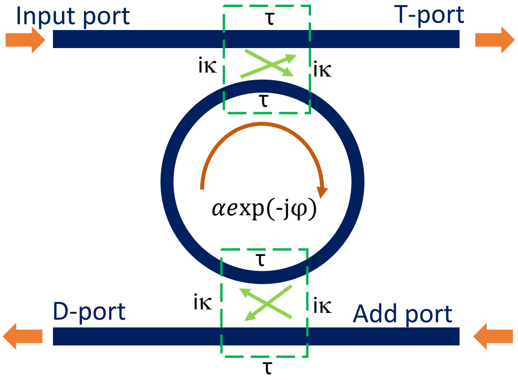

Figure 2.2: Schematic representation of a SRR.

MRRs. Straight forward fabrication processes is possible for optical MRRs because of the absence of mirrors, gratings etc like other types of conventional resonators. Figure 2.2 depicts the schematic diagram of a single ring resonator (SRR) which consists of a ring waveguide closely coupled to two straight bus waveguides. This type of configuration is also known as add-drop SRR filter. The ring waveguide act as a re-entrant waveguide. At resonance, the optical signal launched at the input port of the bus waveguide undergoes constructive interference at the ring waveguide. The resonance condition in a MRR is expressed as $m\lambda_R = 2\pi R n_{eff}$, where m is an integer, R is the radius of ring, n_{eff} is effective refractive index of ring and λ_R is the resonant wavelength. α, τ, κ and ϕ represents absorption, transmission coefficient, coupling coefficient between ring and bus waveguide, phase change as propagating through the ring, respectively [21]. The launched input wavelength $\lambda = \lambda_R$ appears at drop port (D port) while any non-resonant wavelength ($\lambda \neq \lambda_R$) appears at throughput port (T-port). Add port is used to launch additional signal into the ring resonator.

2.2.1 Types of geometrical MRR configurations

Different geometrical configurations are possible in MRRs based on the number of rings and bus waveguides present. The basic configurations of MRRs are shown in Figure 2.3. All pass MRRs are singly coupled MRR with a single ring waveguide coupled to a bus waveguide. All pass ring resonators are capable for introducing delay to the launched optical signal at the input port by temporarily storing in the resonating structure and are sent out through the T port. Add-drop MRR configuration can extract out the resonant wavelength through another port (D-port) by placing a second bus waveguide adjacent to

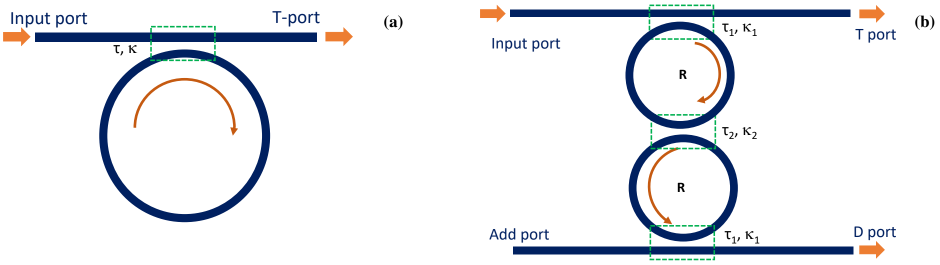

(a) All pass MRR (b) Series MRRs

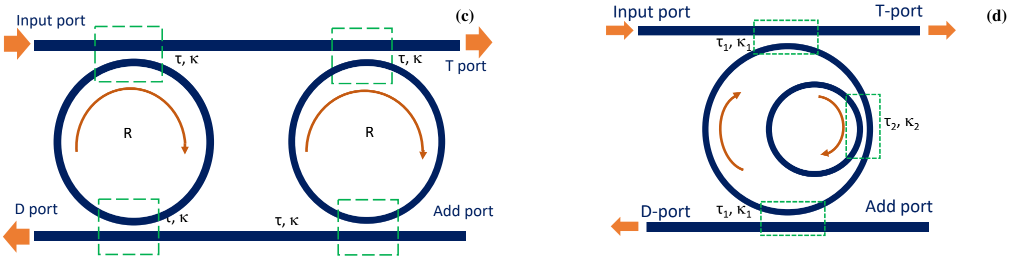

(c) Parallel MRRs (d) Off axis MRRs

Figure 2.3: Geometrical configurations of MRRs (a) All pass MRR (b) Series coupled double ring resonator (c) Parallel coupled double ring resonator (d) Double ring Off axis MRRs

the ring structure as shown in Figure 2.2. The propagation of resonant signal through the D port is in backward direction while the launched signal at input port and non-resonant signal collected at T port propagates in forward direction. Higher order MRRs represents multiple rings arranged in series or parallel configurations. Series coupled double ring resonator (DRR) configuration provides higher degree of designing freedom, maximize the isolation between T port and D port outputs, the input and the output optical signals propagates in the same direction. Degree of designing freedom in MRR configurations depends in the order of rings present in the respective configurations. Coupling between the rings occurs in parallel coupled MRR configuration if the gap between the rings is small. Compact sized filters and modulators can be designed using off resonance MRR configuration, which provides extra resonant notches due to inner off axis ring [22].

The output spectral response of MRR can be clearly understood by relating the output intensity to the incident intensity by deriving transfer functions. Analytical method based on solving node and loop equations in MRR configurations are utilized for obtaining respective transmission to the T port and D port in the add-drop MRR configuration shown in Figure 2.4. τ and κ represents the fraction of launched optical signal passes towards T port and the fraction get couples to the ring structure respectively. E_I,E_T,E_A and E_D corresponds to the field amplitude at input port, T port, add port and D port respectively. E_1,E_2,E_3 and E_4 are the fields at 4 different points in ring waveguide. The field expressions can be expressed as

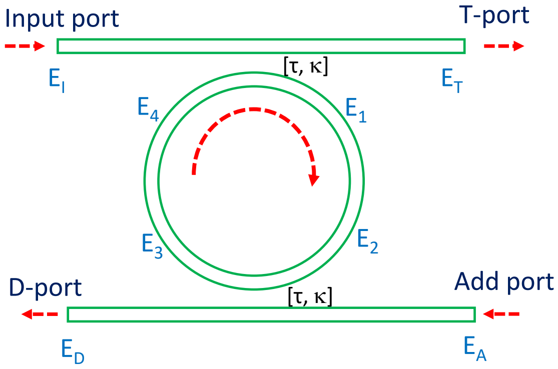

Figure 2.4: Top view perspective of SRR with two bus waveguides with the electric fields at each points represented.

$$E_T = \tau E_I + i\kappa E_4 \tag{2.3}$$

$$E_1 = \tau E_4 + i\kappa E_I \tag{2.4}$$

The phase change and loss (α) experienced by optical signal when passing through the ring waveguide is considered for the field expression at E_2 and E_4.

$$E_2 = \exp\left(\frac{i\omega L n_{eff}}{2c} - \frac{\alpha L}{4}\right) E_1 \tag{2.5}$$

$$E_4 = \exp\left(\frac{i\omega L n_{eff}}{2c} - \frac{\alpha L}{4}\right) E_3 \tag{2.6}$$

The constant c represents the speed of light in vacuum while ω is the angular frequency. The ring circumference is denoted as L, where L = 2πR. Assume that no additional field is applied at add port (E_A=0), hence the fields at E_D and E_3 are

$$E_D = i\kappa E_2 \tag{2.7}$$

$$E_3 = \tau E_2 \tag{2.8}$$

The coupling between the waveguides are assumed to be lossless for the add-drop filter configuration (i.e., $\tau^2 + \kappa^2 = 1$). By algebraic manipulations of these field expressions (Eq.2.3-2.8) yields the T port and D port output field power in terms of launched input field power. The output normalized power at T port (P$_T$) and D port (P$_D$) will be

$$P_T = \left|\frac{E_T}{E_I}\right|^2 = \left|\frac{\tau - \tau\exp(\frac{i\omega L n_{eff}}{c} - \frac{\alpha L}{2})}{1 - \tau^2\exp(\frac{i\omega L n_{eff}}{c} - \frac{\alpha L}{2})}\right|^2 \tag{2.9}$$

$$P_D = \left|\frac{E_D}{E_I}\right|^2 = \left|\frac{\kappa^2\exp(\frac{i\omega L n_{eff}}{2c} - \frac{\alpha L}{4})}{1 - \tau^2\exp(\frac{i\omega L n_{eff}}{c} - \frac{\alpha L}{2})}\right|^2 \tag{2.10}$$

The output transmission power spectrum of T port and D port for a ring radius of 5μm is shown in Figure 2.5 with n$_{eff}$=3.67. At resonant wavelength λ_R=1558.06nm, T port power diminishes while the D port power is higher. The filtering action of MRR can be realized from the spectrum behaviour in Figure 2.5. At critical coupling condition, all the optical signal get coupled to the ring and results in zero power transmission through the T port. Resonance condition in MRR is defined as the condition where the path length propagated by the optical signal through the closed loop waveguide is equal to the integer multiple of the optical signal wavelength propagating through the closed loop waveguide. At this condition, it is observed that the optical signal propagating through the closed loop waveguide and the coupled optical signal to the closed loop waveguide from the bus waveguide of MRR remains is same phase, thus constructivly interfering in the closed loop waveguide. The MRR achieves higher enhancement factor at critical coupling condition, results in maximum intensity building up in the closed loop while minimum intensity (theoretically zero intensity) is observed at the T port. The critical coupling condition is calculated by equating the derivative of T port intensity to zero with respect to coupling coefficient. The critical coupling condition in add-drop MRR configuration (Figure 2.4) with equal coupling between the ring and two bus waveguides is $\exp\left(\frac{i\omega L n_{eff}}{c} - \frac{\alpha L}{2}\right)$=1.

Another geometrical classification of MRRs is based on the coupling of ring to the bus waveguide. Two types of coupling schemes are available: lateral and vertical coupling schemes. Each coupling schemes has certain advantages and disadvantages. The schematic diagram of lateral and vertical coupling schemes are depicted in Figure 2.6 (a) and (b) respectively using FreeCAD software. In lateral coupling, both the ring and bus waveguides

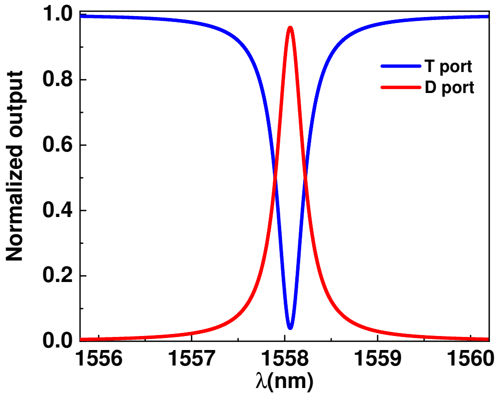

Figure 2.5: Output power spectrum at T port and D port of SRR with R = 5μm and λ_R = 1558.06nm.

are fabricated in the same plane. A single lithographic step process is adequate for the fabrication of ring and bus waveguides. The horizontal gap between the ring and the bus waveguide controls the coupling efficiency. High precision e-beam lithography and etching is required to achieve the specified gap between the waveguides. The failure to attain

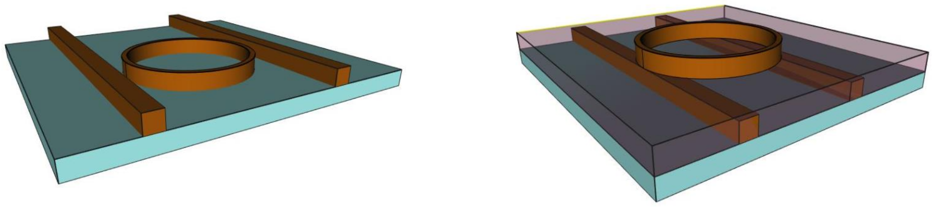

(a) Lateral coupling

(b) Vertical coupling

Figure 2.6: Coupling based MRR configurations (a) Lateral coupling scheme (b) Vertical coupling scheme.

individual waveguide optimization from the design and fabrication perspective is another drawback of lateral coupling configuration as these waveguides are fabricated on a single plane. On the other hand, vertical coupling provides flexibility for individual waveguide optimization as the ring and bus waveguides are fabricated in different planes. The possibility for denser integration is higher in vertical coupling and high precision in achieving specified gap by controlled deposition method rather than etching process. The difficulty in aligning the layers and achieve tapering are the major challenges faced in vertical coupling scheme.

2.2.2 Optical Coupling coefficient of MRR

The transfer functions expressed in earlier section (Eq. 2.9 and 2.10) clearly shows that careful controlling of the coupling coefficients in MRRs can result in performance enhancement of respective filter, switch and modulator applications along with achieving the required specifications. The interstitial mode suppression and controlling resonance splitting in cascaded MRR configuration can be achieved by proper optimization of coupling parameters. The coupling efficiency of a MRR can be increased by increasing the coupling length.

The coupling coefficient (κ) between the waveguides in MRR depends on multiple parameters like the gap between the waveguides, refractive index of waveguides and surrounding medium, operating wavelength, width of waveguides and radius of ring waveguides. Most of the simulation softwares like OptiFDTD, Rsoft FDTD etc. defines mainly the gap between the waveguides rather than defining the coupling coefficients. Hence the relation between the gap and the coupling coefficient is needed to be determined to simulate the structures in these softwares. A method to realize this dependency is through coupled mode theory[23, 24].

The multiparameter dependent coupling coefficient between bus-ring and ring-ring waveguides can be expressed as [23]:

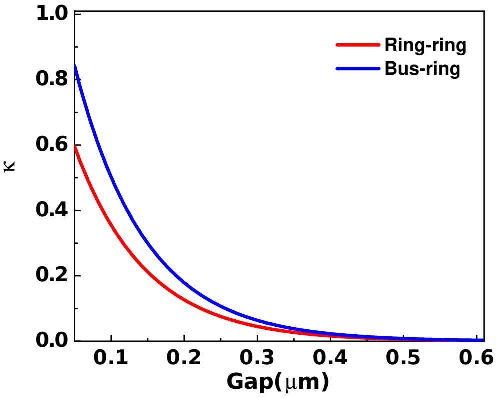

Figure 2.7: Relation between coupling coefficient vs. coupling gap of ring-ring waveguides and bus-ring waveguides in SRR for a radius of 1.7μm.

$$\begin{aligned}\kappa = &\frac{\omega\epsilon_0 \cos(k_{x2}w_2)(n_1^2 - n_0^2)}{2\sqrt{P_1P_2}(k_{x1}^2 + \alpha_2^2)} \times \sqrt{\frac{\pi R}{\alpha_2}} \exp(\alpha_2(w_2 - 2s_0)) \\ &\times(\alpha_2 \cos(k_{x1}w_1)\sinh(\alpha_2 w_1) + k_{x1}\sin(k_{x1}w_1)\cosh(\alpha_2 w_1))\end{aligned} \tag{2.11}$$

The width of the waveguides are represented as w_1 and w_2, n_0 and n_1 represents the refractive index of surrounding medium and waveguide respectively, the center to center gap between the waveguides are denoted as $2s_0$. R_1 and R_2 are the radius of rings for ring-ring waveguide coupling coefficient calculation while R_1 is taken as infinity and R_2 as the ring radius for the bus-ring waveguides.

$$\begin{aligned} R &= \text{Effective radius of curvature=}\frac{R_1R_2}{R_1 + R_2} \\ P_i &= \text{Mode power=}\frac{\beta_i}{2\omega\mu_0}(w_i + \frac{1}{\alpha_i}) \\ \alpha_i &= \text{Decay constant in cladding=}\sqrt{\beta^2 - n_0^2k^2} \\ k &= \text{free space wave vector=}\frac{2\pi}{\lambda} \\ k_{xi} &= \text{Propagation constant in core=}\sqrt{n_i^2k^2 - \beta^2} \end{aligned}$$

By using these equations, the coupling coefficient between two planar optical waveguides with dissimilar refractive indices, arbitrary widths and separation can be calculated. The Figure 2.7 depicts the dependency of ring-ring and bus-ring waveguide coupling coefficient on the gap between the waveguides for the waveguide widths as 0.2μm, radius of rings as 1.7μm, refractive index of the waveguides as 3.48 and the operational wavelength as 1.55μm. It is observed that the coupling factor between bus-ring waveguide is higher than ring-ring waveguides for a fixed gap because of larger coupling length achieved in bus-ring waveguide.

2.3 Performance parameters

The performance parameters discussed in this section includes major spectral and switching characteristics of MRRs. The spectral parameters include free spectral range (FSR), full width half maximum (FWHM), Finesse (F), quality factor (Q-factor), out of band rejection (OBR), shape factor. The switching parameters include contrast ratio (CR), insertion loss (IL), cross talk, polarization dependent loss (PDL), rise and fall time transients.

FSR is the figure of merit of a ring resonator, which represents the distance between

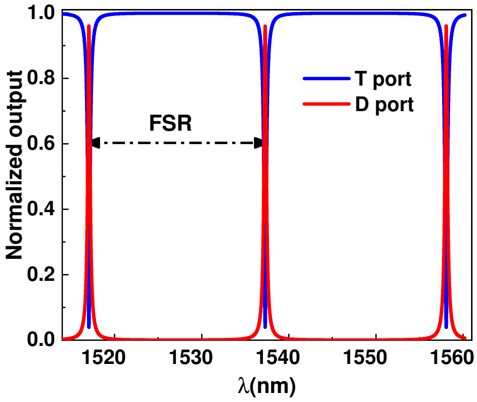

Figure 2.8: Transmission spectrum of MRR with FSR marked in the plot.

consecutive resonant peaks. One of the critical design requirement in filters and sensors is to attain higher FSR. The expression for calculating FSR is given by

$$FSR = \frac{\lambda^2}{n_{eff}L} \tag{2.12}$$

From Eq.2.12, it is observed that the FSR is inversely proportional to the ring size. Hence, small footprinted rings are suitable for applications with large FSR requirements. Figure 2.8 shows the FSR in transmission spectrum of SRR. FWHM is used to define 3dB bandwidth of ring resonator. It can be calculated as the wavelength range between the points where the signal amplitude reduces to half its maximum value. FWHM of an add-drop MRR configuration can be expressed as

$$FWHM = \frac{\lambda^2}{\pi n_{eff}L}\frac{1-a\tau}{\sqrt{a\tau}} \tag{2.13}$$

Here *a* is the round trip loss in the ring. The ability of the ring resonator to travel round trips before losing the energy is expressed in terms of Finesse (F). Finesse can be calculated as the ratio of FSR to FWHM. For an ideal lossless ring resonator, the finesse value is infinity. The finesse for a lossy resonator is

$$F = \frac{FSR}{FWHM} = \frac{\pi\sqrt{a\tau}}{1-a\tau} \tag{2.14}$$

The sharpness of the resonance is measured by Q-factor. Q-factor is calculated as the ratio of energy stored in the resonator to the energy lost during one cycle.

$$Q\,factor = \frac{\pi n_{eff} L}{\lambda} \frac{\sqrt{a\tau}}{1 - a\tau} \tag{2.15}$$

OBR represents the filtering ability to reject the signals present out of the desired frequency band. In MRR configuration, OBR is defined as the difference between the maximum signal intensities (I^{max}) and minimum signal intensities (I^{max}) in the drop port,

$$OBR = I_{drop}^{max} - I_{drop}^{min} \tag{2.16}$$

Shape factor represents the selectivity of the filter. It is measured as the ratio of -3dB bandwidth to -10dB bandwidth. As the shape factor approaches unity, the passband spectrum will be more of rectangular shape.

$$Shapefactor = \frac{-3dB\,bandwidth}{-10dB\,bandwidth} \tag{2.17}$$

Insertion loss of a ring resonator represents the signal power loss added into the system due to the insertion of the ring resonator. Insertion loss should be minimum for better system performance. In ring resonator, it is measured as the difference between the optical signal power launched at the input port and the power collected at output ports (T port and D port). It depends on the absorption characteristics of the ring and bus waveguides. Even the operating wavelength contribute to the variation in insertion loss.

$$IL = P_I - (P_T + P_D) \tag{2.18}$$

Contrast ratio or contrast difference is defined as the power variation occurs during ON and OFF condition of the switch. For a ring resonator switch, both T port and D port outputs can act as switching output. The difference between the optical signal power at the output ports during ON condition and OFF condition represents the CR of MRRs. CR should be maximum for high efficiency switches.

$$CR = P_{T\ (ON)} - P_{T\ (OFF)} \tag{2.19}$$

Crosstalk determines the output power due to unwanted signal present in the input port. It is measured as the ratio between the power at the output port due to unwanted signal to the power due to desired signal. It should be minimum for high efficiency switches.

Rise time and fall time transients in switches represent the switching time to reach steady state response during turn ON and OFF conditions. It should be minimum to avoid inter-symbol interference effect and to meet high switching rate requirements.

2.4 Vernier effect

It is observed from Eq.2.12 that the ring resonator with smaller radius are required to obtain large FSR for filtering and sensing applications. But the bending losses increase as the ring radius decrease, thus limiting the performance of the ring resonator. Under these multiple constraints, vernier effect is an alternative scheme to achieve large FSR without reducing the ring radius. Vernier MRR configurations consists of series MRRs with different ring radii. Also the sensitivity of the vernier MRR is higher than SRRs [25, 26]. Figure 2.9 is showing a vernier DRR configuration with L_1 and L_2 as the circumferences of the rings with radii R_1 and R_2 respectively. The resultant FSR of the vernier MRR will be the least common multiple of individual rings and can be expressed as

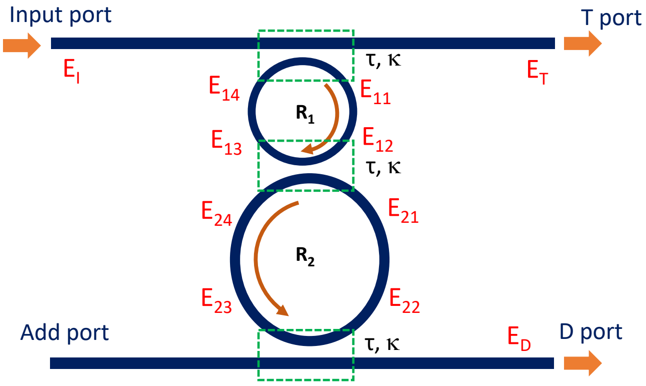

Figure 2.9: Schematic diagram of DRR employing the vernier effect.

$$FSR = N.FSR_{ring1} = M.FSR_{ring2} \tag{2.20}$$

FSR_{ring1} and FSR_{ring2} represents the FSR of the individual rings in vernier DRR configuration. Here, M and N should be co-prime numbers.

The normalized transfer function at T port and D port of vernier DRR configuration (Figure 2.9)) is derived by solving the field expressions (Eq.2.21-2.32) at different points in bus and ring waveguides.

$$E_{11} = \tau E_{14} + i\kappa E_I \tag{2.21}$$

$$E_T = \tau E_I + i\kappa E_{14} \tag{2.22}$$

$$E_{12} = \exp\left(\frac{i\omega L_1 n_1}{2c} - \frac{\alpha_1 L_1}{4}\right) E_{11} \tag{2.23}$$

$$E_{13} = i\kappa E_{21} + \tau E_{12} \tag{2.24}$$

$$E_{14} = \exp\left(\frac{i\omega L_1 n_1}{2c} - \frac{\alpha_1 L_1}{4}\right) E_{13} \tag{2.25}$$

$$E_{24} = \tau E_{21} + i\kappa E_{12} \tag{2.26}$$

$$E_{23} = \exp\left(\frac{i\omega L_2 n_2}{2c} - \frac{\alpha_2 L_2}{4}\right) E_{24} \tag{2.27}$$

$$E_{22} = \tau E_{23} \tag{2.28}$$

$$E_{21} = \exp\left(\frac{i\omega L_2 n_2}{2c} - \frac{\alpha_2 L_2}{4}\right) E_{22} \tag{2.29}$$

$$E_D = i\kappa E_{23} \tag{2.30}$$

Let us assign that

$$C_1 = \exp\left(\frac{i\omega L_1 n_1}{c} - \frac{\alpha_1 L_1}{2}\right)$$
$$C_2 = \exp\left(\frac{i\omega L_2 n_2}{c} - \frac{\alpha_2 L_2}{2}\right)$$

The refractive indices of the rings are assumed to be n$_1$, n$_2$ and the absorption in the respective rings as α_1 and α_2. By applying substitution method on the field expressions mentioned, the output optical power at T port (P_T) and D port (P_D) is obtained in terms of the optical power launched at input port. E_T and E_D can be expressed in terms of E_I to obtain T port power P_T ($|E_T|2$) and D port power P_D ($|E_D|2$) respectively. Eq.2.22 gives E_T in terms of E_I and E_{14}. E_{14} is substituted using Eq.2.25, where E_{13} is substituted from Eq.2.24. E_{21} can expressed in terms of E_{12} by substituting E_{22} in Eq.2.29 using Eq.2.28, Eq.2.27, and Eq.2.26. Also E_{12} can be expressed in terms of E_{14} and EI using Eq.2.23 and Eq.2.21. Finally we obtain E_{14} in terms of E_I which can be substituted in Eq.2.22 to yield the field expression E_T and corresponding T port power. Similarly, E_D is expressed in term of E_{23} in Eq.2.30. E_{23} in Eq.2.30 can be substituted using Eq.2.27 where E_{24} is expressed in terms of E_{21} and E_{12} from Eq. 2.26. E_{21} andE_{12} is already solved in terms of

E_I. Substituting these expressions in Eq.2.30 yield the D port power.

$$P_T = \left|\frac{\tau(1 - C_1 + C_1C_2 - \tau^2C_2)}{1 - \tau^2(C_1 + C_2 - C_1C_2)}\right|^2 \tag{2.31}$$

$$P_D = \left|\frac{(i\kappa)^3\sqrt{C_1}\sqrt{C_2}}{1 - \tau^2(C_1 + C_2 - C_1C_2)}\right|^2 \tag{2.32}$$

Comparison between the power spectrums at T port and D port of SRR and vernier DRR is

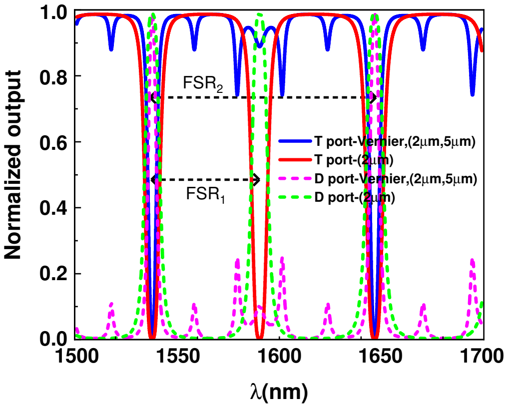

Figure 2.10: Power spectral responses of vernier DRR (radius=5μm and 2μm) and SRR (radius=2μm) configurations. FSR$_1$ =50nm and FSR$_2$=100nm, FSR$_1$ and FSR$_2$ denotes FSR of SRR and vernier DRR respectively.

shown in Figure 2.10. In this figure, FSR$_1$ and FSR$_2$ denotes FSR of SRR and vernier DRR respectively and the ring radius of SRR is taken as R=2μm and ring radii of vernier DRR as R$_1$=2μm, R$_1$=5μm. The FSR$_1$ and FSR$_2$ obtained are 50nm and 100nm respectively.

2.5 Applications of MRR

MRRs are highly suitable for different applications which are widely spread out in different areas. The contributions of MRR in the fields of sensing, filtering, modulation, switching, routing and logic gates etc are significant. So many technological and configurational advancements are undergoing to improve the performance of MRR in on-chip applications. MRR based thermal sensors [27], pressure sensors [28], biosensors [29] and chemical sensors [30] are well known for operating with higher sensitivity, reliability, integrability and miniaturization. Figure 2.11(a) shows a MRR based sensor with a continuous input signal launched at the input port. The launched signal is assumed to be resonant to the MRR when the analyte (target) to be detected is not passed into the structure. The ring structure is provided with respective receptors to attach the analyte when it is allowed to pass through the MRR sensor. After passing the analyte through the sensor device, the analyte get attached to the receptor and leads to refractive index change of MRR. The change in refractive index leads to intensity variation of output optical signal collected at T port due to resonant wavelength shift. Hence the presence of the analyte can be detected based on the T port output intensity variation. Similarly, the temperature and pressure sensor also leads to refractive index variation in the MRR and results in intensity change. Moreover, multiple circulation of light inside the MRR enhances the interaction with targets and helps the detection of smallest quantity of the analyte. It is able to achieve a detection limits on the order of 10^{-7} RIU.

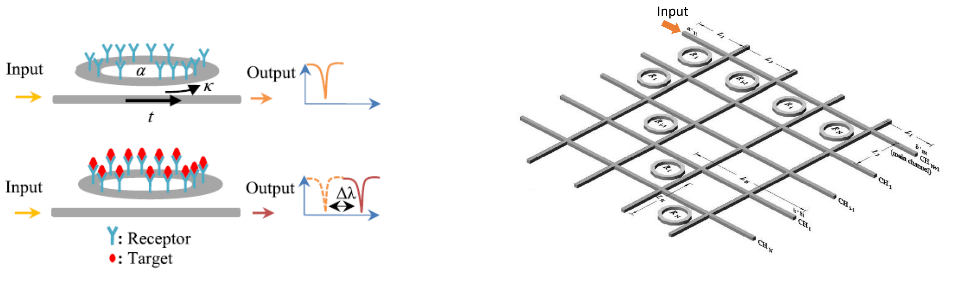

(a) MRR Sensor (b) Switching and routing

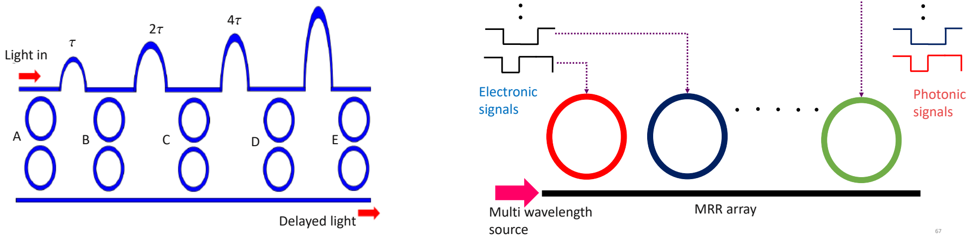

(c) Delay line circuit (d) WDM signal modulation

Figure 2.11: Different MRR applications (a) MRR based chemical/bio sensor [**?**] (b) MRR array based switching and routing configuration [**?**] (c) Optical delay line circuits based on cascaded parallel MRRs (d) WDM modulator based on MRR arrays

The filtering action of MRR can be analysed from Figure 2.5, which depicts the behaviour of the output spectrum of SRR. It is observed that the resonant signal is filtered out from the T port and appears at D port, results in notch filtering effect. Switching and routing of optical signal using MRR have attracted great attention in the signal processing field. Figure 2.11(b) shows a type of MRR based switching configuration. The signal launched at the input can be collected through different channels (CH$_1$-CH$_{N+1}$) depending on the resonant nature of MRRs present in the configuration. The resonant condition can be altered by applying bias on the rings. The configuration designed in Figure 2.11(b) gives output through main channel when all the MRRs are at off resonant condition (bias applied on all the MRRs).

Another interesting application of MRRs are assigning optical transmission delays [31]. Figure 2.11(c) depicts a MRR based delay line configuration in which the launched input signal can be converted into its delayed version and collected through D port with delays ranging from 0-15τ. The output signal experiences zero delay if the cascaded MRR A is at resonant condition while all other cascaded MRRs (B,C,D,E) are at off resonance. When MRR E satisfies resonant condition and all other MRRs at off resonant condition leads the input signal to undergo a delay of 15τ. The features of microring resonator is highly compatible to implement as modulators/switches in on-chip communications. Figure 2.11(d) shows a WDM signal modulator based on MRR arrays. Wavelengths launched through the multiwavelength source gets coupled to the rings and those wavelengths satisfying the resonant condition gets circulated through the respective rings. The applied electrical signal on each ring results in resonant wavelength shift, thus the circulating optical signal in the respective ring undergoes modulation. The T port of the MRR array collects the modulated optical WDM signals from each MRRs.

The contribution of MRRs in the medical field for screening and detection is highly appreciable. Optical thermography using MRR configuration is an efficient non contact method for temperature detection, especially during COVID 19 scenario. Point of care diagnosis of viruses including corona virus using MRRs is a fast developing interesting field.

2.6 MRR modulation mechanisms

As mentioned from Eq.2.9 and Eq.2.10, that the spectral response at T port and D port of MRR strongly depends on the refractive index of microring, absorption in microring and coupling strengths between waveguides of microring. The optical modulation can be implemented into MRR by varying any of these three parameters. The modulation mechanisms based on varying refractive index with respect to applied bias is known as electrorefraction. Electroabsorption is the modulation mechanisms in which the absorption property of the material is varied with respect to applied electric field. Coupling modulation is achieved by varying the coupling coefficients in MRR with respect to applied bias. Even though coupling modulation provides high Q resonant nature, the need for microelectromechanical systems increases fabricational complexities.

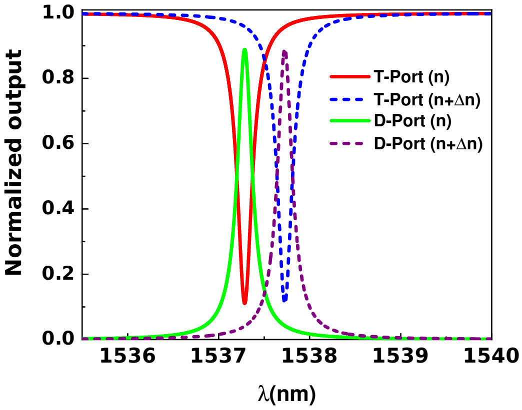

Figure 2.12: Output port spectrum of SRR configuration by varying refractive index.

This thesis have considered the optimization and designing of MRR modulators based on varying refractive index and absorption in the ring structures using electrical bias. The variation in refractive index and absorption results in switching of optical signal between T port and D ports of MRR. Most of the MRR filters are passive in nature, whose responses are fixed and there is no provisions for tuning the spectral response further once it has been fabricated. Electrorefractive and electroabsorptive MRR modulators requires active materials like III-V semiconductors which are capable to change its refractive index and absorption in response to applied bias to provide enhanced functionalities to the modulator.

In this thesis, active III-V materials like GaAs, InGaAsP are considered which have the ability to change refractive index and absorption with respect to small bias applied on the rings and can also operate efficiently in lowest attenuation and dispersion windows in optical communication. Figure 2.12 plots the output spectrum at T port and D port with respect to refractive index change in a SRR with two bus waveguides. The resonant wavelength shifts as the refractive index varies from n to n+Δn by applying bias on the ring structure and accordingly optical signal switching occurs between T port and D port. The resonant wavelength can be red shifted or blue shifted according to increase or decrease in refractive index. Carrier injection based electrorefractive modulation mechanism injects carriers into the ring structure and results in refractive index variation.

Figure 2.13 plots the response at the T-port output spectrum of SRR for the absorption changes $\alpha_1, \alpha_2, \alpha_3$ ($\alpha_1 < \alpha_2 < \alpha_3$). The intensity of T port output increases as the

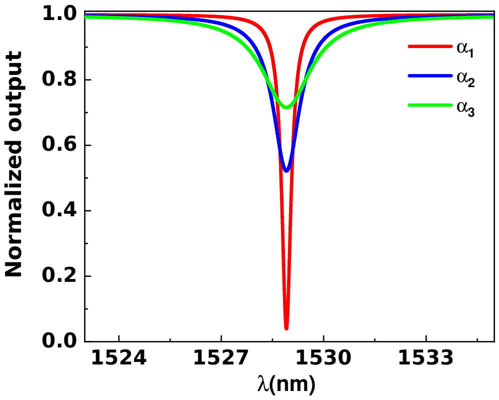

Figure 2.13: T port spectrum of SRR configuration by varying absorption ($\alpha_1, \alpha_2, \alpha_3$) in ring.

absorption in the ring resonator increases. Quantum confined stark effect is an efficient electroabsorption modulation mechanism which can change the absorption of QWs incorporated in the rings and results in signal switching between the output ports of MRR.

2.7 Conclusions

In this chapter, a brief overview of microring resonators along with its performance parameters and applications were discussed. The transfer functions of single ring resonator and vernier double ring resonator are derived. Also studied the switching of optical signal between T port and D port due to change in refractive index and absorption in the ring resonator. III-V semiconductor material based MRRs can realize carrier injective and electroabsorptive MRR modulator/switches by varying refractive index and absorption respectively according to applied bias.

Chapter 4

Design and optimization of electroabsorptive MRR logic gates

4.1 Introduction

Logic gates are the cornerstone of high-speed signal processing units. A new paradigm introduced by Hardy and Shamir [48] has combined the benefits of optics and electronics to achieve directed logic functionality. The convenience of control and high-speed operation can be achieved simultaneously in electro-optic logic circuits by using the electron for signal control and the photon for signal operation [49]. Optical operations performed on each switching elements in the network to realize Boolean logic functions are independent to each other, thus leading to very low latency, which is in contrast to electronic logic circuits where the gate delays get accumulated in the processing time. Optical directed logic gates open up new horizon for computational parallelism at the speed of light, and also provides higher packaging density in integrated circuit platforms. Microring resonators (MRRs) have widely been used to implement different combinational and sequential optic logic functionality due to their unique properties, such as, small footprint, flexibility in tuning resonant wavelength and narrow band filtering. The resonant condition in the ring resonator can be altered by different mechanisms, such as, bias assisted carrier injection, thermo optic effect, electro optic effect and electro absorption (EA), thus enabling applications such as optical switching, optical modulator, optical logic gates and sensing.

Many researchers have investigated carrier-injection (CI) based electro-optic logic circuits in MRRs [50], along with improved thermal stability of the MRRs by integrating microheaters on the chip architecture [51]. Also, appreciable results have been obtained by implementing all-optical MRR logic gates and utilizing the non-linearity of the electro-optic materials leading to optical switching [52]. In this thesis, we propose various logic gate configurations based on the quantum confined stark effect (QCSE) [53] in p-i-n diode embedded MRRs. The quantum wells are incorporated in the i-region of the p-i-n diode, which also acts as the light guide. Absorption changes associated with the QCSE in quantum wells lead to a change in the refractive index, thus resulting in switching of states.

We show that those optical logic gates in which the states can be switched through the EA effect can only be realized through proper optimization of the ring and quantum well (QW) parameters along with proper selection of the operating wavelength and applied field. The proposed configurations result in directed logic gates, which simultaneously yield a logic operation and its complement at different ports of MRR. In this chapter, we discusses the modelling of optical switching in p-i-n heterostructure MRR incorporated with EA QWs, and presents the design structures to analyze AND, NAND, XOR, XNOR and Fredkin gate. The reason behind the failure of realizing OR and NOR gates by a parallel EA MRRs configuration is analysed. A novel triple ring MRR configuration for simultaneously realizing OR as well as AND gates at the output ports through the EA mechanism is presented.

4.2 Realization of electroabsorptive ring resonator based optical gates

The major advantages provided by electroabsorptive QW-based MRRs over other optical switching configurations are the low drive power requirements, high speed of operation, better sensitivity, very small active volume, higher absorption change contributed by excitons and the resonance tunability attained by independently varying quantum well material composition and well width. The normalized field expressions at the T port and D port of the logic gate MRR configurations are expressed in terms of the fields at input port and add port, absorption, phase and coupling coefficients of MRR. With the applied field, the EA QW-based MRRs act as optical switch, whereby the absorption parameter of the QWs placed in the light propagation path of the ring structure is varied. The change in absorption leads to a change in the refractive index, through Kramers-Kronig (KK) relation (refer Eq.3.4), and results in a shift in the resonant wavelength. Note that, the shift in the absorption edge of a QW with an applied field is termed as QCSE. The entire logic gate configurations are grown over an InP substrate with electrodes deposited over the rings (p electrodes) and beneath the substrate (n electrodes). The operating wavelength has to be selected close to the bandedge wavelength, however, this should be greater than the bandedge wavelength of the QW, in order to obtain a considerable absorption change due to QCSE. The well/barrier materials are chosen as In$_y$Ga$_{1-y}$As$_x$P$_{1-x}$/InP so that the operating wavelength is within the low attenuation window used in optical communications. By properly choosing the material composition (x, y), InGaAsP can be lattice matched with InP, and the effective index of QW is expressed as $\sqrt{\frac{n_w(x,y)L_w+n_bL_b}{L_w+L_b}}$, where n_w is the refractive index of well material (In$_y$Ga$_{1-y}$As$_x$P$_{1-x}$), which depends on the material composition, n_b is the barrier (InP) refractive index, and L_w, L_b is the QW and the barrier width, respectively [44]. We assume a lossless coupling between the waveguides and ring for all the designed logic gate configurations (i.e., $\tau^2 + \kappa^2 = 1$). The launched beam is assumed to be TE polarized, and we further assume that no polarization conversions takes place as the beam propagates through the straight waveguides/rings. The excitonic absorption in QW as a function of applied field and operating wavelength, $\alpha(F,\lambda)$ can be expressed as [40].

$$\alpha(F, \lambda) = 10^4 \Big(\frac{75\Gamma_0}{L_w \Gamma_h} \mathring{A} \Big) \times f \times \exp\Big(- ln2 \Big[\frac{E_{ex}(F) - hc/\lambda}{\Gamma_h} \Big]^2 \Big) + \alpha_B \tag{4.1}$$

The excitonic energy varies with the applied field and the excitonic peak wavelength gets red shifted at higher fields. Excitonic energy (E_{ex}) is expressed as $E_g + E_e + E_{hh} - E_b$. Here, E_e, E_{hh} are the electron and heavy hole particle energies, respectively, and E_g represents the bulk bandgap of In$_y$Ga$_{1-y}$As$_x$P$_{1-x}$. Most of the transitions occurs between the ground state level of the electrons and heavy holes, and hence only the fundamental transition is used in calculating the QCSE spectrum. The field dependence of excitonic binding energy (E_b) seems to be negligible compared to field dependent particle energies, and hence, it is neglected in our calculations. Γ_0 represents the half width half maximum (HWHM) linewidth of the exciton at zero field. The broadening of excitonic linewidth occurs with increasing the well width and the applied field. The modified excitonic HWHM linewidth (Γ_h) at a fixed field and a well width is expressed as $\Gamma_h = \Gamma_0 + (B/L_w^2) + \zeta F$ [40]. The overlap integral (f) which represents the overlap between electron and hole wavefunction also reduces with the applied field.

4.2.1 Fredkin gate using single MRR

The controlled SWAP (C-SWAP) gate also known as the Fredkin gate is a reversible gate that swaps the inputs when the control signal is high. This gate can be realized using p-i-n heterostructure EA QW based single MRRs (Figure. 4.1(a) and (b)). The field applied on the p-i-n embedded ring acts as the control signal. The input optical signals (Input1, Input2) are launched at the input port and add port, respectively, while the corresponding outputs of the operations are collected through the D port and T port, respectively. Here the operands and operational outputs are in the optical domain, whereas the control signal is in the electrical domain. We assume that the wavelength of the launched input signals at the input port and add port satisfies the resonant condition when no field is applied onto the ring. With an applied electric field, the absorption of the ring changes, resulting in a concomitant change in the refractive index, thus leading to an out-of-resonance condition. The control signal (which represents the applied electric field) is logical 0 with no applied field and represents a logical 1 with an applied electric field. The presence and absence of the launched input signal at the input ports are represented as logic 1 and logic 0, respectively. The working of the proposed Fredkin gate can be explained by the following four cases:

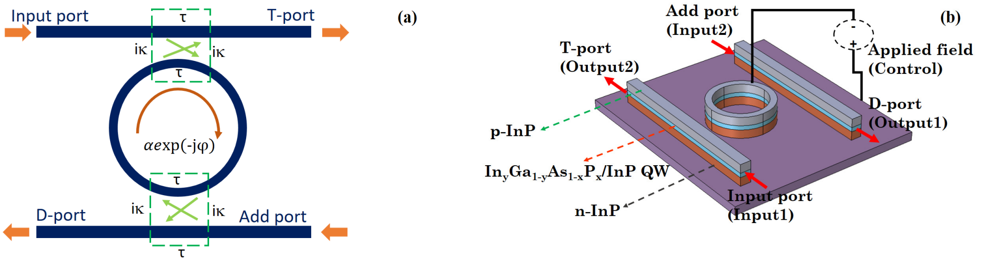

Figure 4.1: (a) Schematic diagram of a single MRR. (b) Perspective view of Fredkin gate with EA In$_y$Ga$_{1-y}$As$_x$P$_{1-x}$/InP QW based single MRR.

Case 1: (Input1=0, Input2=0): When both input port and add port are logic 0, the output intensities at the T port and the D port remain low (logic 0 output), irrespective of the applied field on the ring (i.e., Whether the control input is logic 0 or logic 1).

Case 2: (Input1=0, Input2=1): When the input port is at logic 0, the add port is at logic 1 and the control signal is at logic 0 (resonance condition satisfied), then the output intensity at the T port (Output2) will be high (logic 1) and the intensity at the D port (Output1) will be low (logic 0). When the control signal is at logic 1 condition (out-of-resonance condition), then the D port (Output1) transmits a high intensity beam (logic 1) while the intensity at the T port (Output2) appears low (logic 0).

Case 3: (Input1=1, Input2=0): When the input port is at logic 1, the add port is at logic 0 and the control signal is at logic 0 condition (resonance condition satisfied), then the output intensity at the T port (Output2) will be low (logic 0) and the intensity at the D port (Output1) will be high (logic 1). When the control signal is at logic 1 (non-resonant condition satisfied), then the T port (Output2) transmits a high intensity beam (logic 1) while the

intensity at the D port (Output1) appears low (logic 0).
Case 4: (Input1=1, Input2=1): When both the input port and the add port are at logic 1, the output intensities at the T port and the D port appears to be high (logic 1) irrespective of the applied field (control signal). The beam propagates towards the T port and the D port at resonance and out-of-resonance conditions due to the inputs applied at the input and add ports.

The Fredkin configuration can be used to realize a buffer gate, a NOT gate, a two-input AND and a two-input OR gates with appropriately setting both (for Buffer and NOT) or one of the inputs (Input1 and Input2)[54, 55]. The major drawback of the proposed EA MRR based Fredkin configuration is that the control signal is in the electrical domain, which complicates the performance as a universal gate, in which the control signal is used as one of the operand (as in the case of the two-input AND and OR gates based on the Fredkin configuration, the operands are not in a single domain).

4.2.2 AND and NAND gate using parallel DRR

The electrical-optical and optical-electrical conversion adversely affects the overall performance of Fredkin configuration based AND gates. A parallel configuration of MRRs with EA QW-incorporated double rings can be realized as two-input AND and NAND gates with all the logical operands in the electrical domain and the logical gate operational outputs in the optical domain (Figure. 4.2). The distance between the rings are adjusted in such a way that the coupling between the individual rings is negligible. The signal launched at the input port is a continuous signal that satisfies the resonant condition at zero applied field on the rings of the double ring resonator (DRR). The field applied separately on each rings act as the two operands and the beam intensities collected at T port and D port gives logical

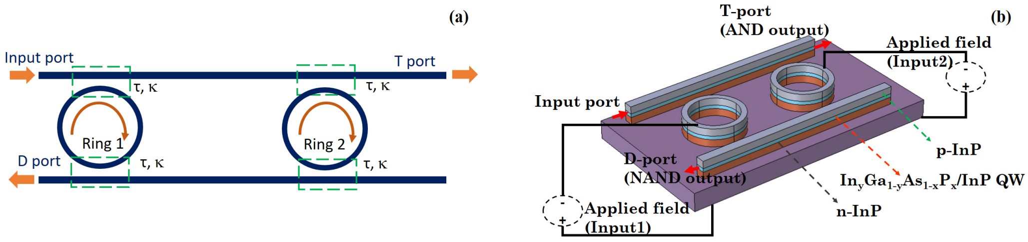

Figure 4.2: (a) Parallel DRR for realizing AND NAND gate. (b) Perspective view of AND NAND gate based on EA QW embedded on parallel MRR.

AND and NAND gate outputs respectively. The inputs are taken as logic 1 with a non-zero field applied (Input1=1/Input2=1 for $F \neq 0$ applied on Ring1/Ring2) and as logic 0 with no field applied on the rings. Zero-field applied on any one of the rings results in resonant condition at the ring and leads the light beam launched at the input port to appear at D port. While non-zero field applied on both rings results in out of resonance condition and the light beam launched at the input port to appear at T port [56].

The parallel MRR configuration can act as logical NOR gate and OR gate at the T port and the D port, respectively, in which the states are changed by thermo-optic effect as reported in [56]. Using the same parallel EA DRR configuration (Figure. 4.2), and by launching a continuous signal whose wavelength satisfies the resonance condition at an applied field, the device can act as an OR gate and a NOR gate at the D port and the T port, respectively. With an applied electric field to the ring(s), an index change is induced in such a way that the launched signal is now at resonance in the ring, which enables the signal to couple into the ring and appear at the D port. However, a concomitant absorption change is invariably present in the ring, which causes attenuation of the resonant signal, leading to a poor contrast ratio between the 1 and 0 signals, and making the realization of OR/NOR gates impractical.

4.2.3 XOR, XNOR gates using ring resonators and U-bent waveguides

XOR and XNOR logic gates can be implemented using two cascaded EA QW incorporated MRRs (Ring1 and Ring2) and two U-bent waveguides (Figure. 4.3). The wavelength of the continuous optical signal launched at input port of the MRR architecture act as resonant wavelength for zero-field applied on the p-i-n heterostructure rings. The fields applied on the rings are selected as the operands and the output intensities collected at the T port and the D port of Ring2 as the XOR and XNOR logic outputs. The D port output of Ring1 is supplied to the input port of Ring2 using a short U bent waveguide, also the T port of Ring1's output enters as the add port input for Ring2 through a long U bent waveguide. The lengths of U-bent waveguides are suitably selected to attain a total phase shift of 2π, when the beam propagates through these waveguides. The operation of this proposed XOR XNOR logic gate architecture is described as identical field condition applied on the rings (both in either resonant or non resonant) results in a high-intensity output signal (logic 1) at the D port of Ring2 (XNOR output) and low-intensity output signal (logic 0) at the T port of Ring2 (XOR) while non-identical field condition leads to high-intensity output signal at the T port of Ring2 and low-intensity output signal at the D port of Ring2 [50].

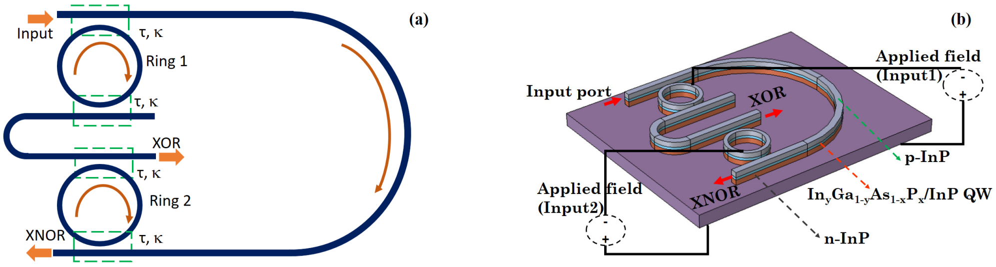

Figure 4.3: (a) Cascaded double ring MRR configuration with U-bend waveguides for realizing XOR and XNOR gate. (b) Perspective view of XOR XNOR gate based on EA QW based MRR.

Three-input XOR and XNOR gates can be realized by cascading the outputs of two input XOR and XNOR gates (Figure. 4.3) into the Fredkin gate (MRR3) configuration, shown in Figure. 4.1, with the third input being the field applied onto MRR3.

4.2.4 OR and AND gates using triple MRRs

We have already discussed the difficulty in realizing an OR gate using the EA mechanism in a parallel DRR configuration (Section 2.2). In this section, a novel triple-MRR configuration, shown in Figure. 4.4, is proposed for simultaneously realizing OR as well as AND gates. A resonant signal is continuously launched at the input port of Ring1 and the add port of Ring2. Here the logic operands are the electric fields applied onto Ring1 and Ring2 (Input1 and Input2), and the logic outputs are obtained as the light intensities at the T port and the D port of Ring3. If the field applied onto Ring1 and Ring3 is the same, then the T port of Ring3 gives an OR output and the D port gives an AND output. Similarly, if the field applied onto Ring2 and Ring3 is the same, then the T port of Ring3 provides an AND output and the D port of Ring3 gives an OR output. Ring3 here acts as a Fredkin gate with the T port output of Ring1 fed as an input into the input port of Ring3 and the add port of Ring3 fed with the D port output of Ring2. The operation of the device as a logic gate is discussed below. Here, the applied field on Ring3 is the same as that on Ring1.
Case 1: (Input1=0, Input2=0): A zero field applied on Ring1 and Ring2 results in resonant condition at Ring1 and Ring2, therefore, the intensities at the T port and the D port of Ring3 will be low (logic 0) as there is no optical input to Ring3.
Case 2: (Input1=0, Input2=1): A non-zero electric field applied on Ring2 (i.e., MRR2 becomes out of resonance, thus bypassing Ring2) yields high intensity at the drop port of Ring2. The drop port of Ring2 is connected to the add port of Ring3, and thus the optical

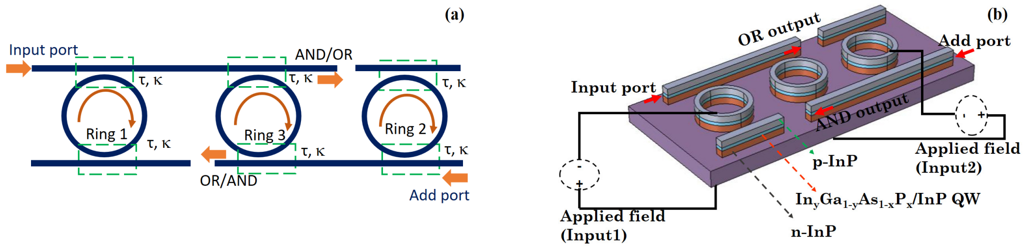

Figure 4.4: (a) Parallel triple ring MRR configuration for OR and AND gate realization. (b) Perspective view of OR AND gate based on EA MRR.

signal launched at the add port of Ring2 couples into Ring3 (Ring3 is at resonance as no field is applied onto it) and appears at the T port of Ring3, resulting in a high intensity signal (logic 1) at the T port and a low intensity signal (logic 0) at the D port of Ring3. The T port of Ring3 now acts as an OR gate, and the D port of Ring3 acts as an AND gate.
Case 3: (Input1=1, Input2=0): A non-zero electric field applied on Ring1 causes the launched signal at input port to bypass Ring1 and Ring3, and appear at the T port of Ring3. With no field applied on Ring2 the resonant signal routed to the add port of Ring2 appears at the T port of Ring2. As a result, no signal appears at the D port of Ring3.
Case 4: (Input1=1, Input2=1): A non-zero electric field applied on Ring1 and Ring2 results in out-of-resonance conditions in MRR1 and MRR2, and hence, the zero field resonant signals routed to the input port of Ring1 and the add port of Ring2 bypass Ring1, 2 and 3, and appear at the T port and the D port of Ring3.

4.3 Results and discussions

4.3.1 Fredkin gate outputs

The configuration and operation principle of the Fredkin gate based on the EA mechanism are discussed in Section 4.2.1. The logical inputs for the gates are determined by the intensity of the launched continuous resonant wavelength beam at the input port and the add port. The signal wavelength launched at the input port and the add port is taken as 1515.27nm, which satisfies the resonant condition for a ring radius of 5μm. In$_y$Ga$_{1-y}$As$_x$P$_{1-x}$ with x=0.1 and y as (16.6+15.6x)/(31.2+x) [40] is the material for QW with InP being the barrier, and these QWs constitute the intrinsic region of the p-i-n diode, and also acts as the light core. The chosen material composition ensures perfect lattice matching between the two materials. The width of QW is taken as 75Å and the barrier width as 70Å (enough to decouple between the wells so that the particle wavefunctions of the adjacent wells do not interact). For c (control signal, i.e., the applied electric field to the QW) $\neq 0$, the input wavelength experiences absorption and the corresponding refractive index change leads to out-of-resonance condition in the MRR. According to Figure. 4.5, the absorption change and refractive index change in a 75Å wide QW for an applied electric field of 70 kV/cm are 219.64cm^{-1} and 0.0029, respectively. For an applied field of 100 kV/cm, the absorption and index changes are 667.88cm^{-1} and 0.0043 respectively at 1515.27nm, and the corresponding port intensities are listed as truth table in Table 4.1.

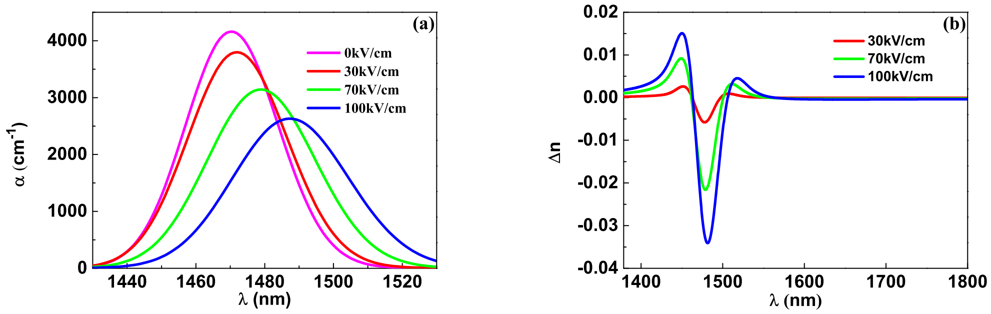

Figure 4.5: (a) Absorption spectrum in a 75Å wide QW at applied fields 0 kV/cm, 30 kV/cm, 70 kV/cm and 100 kV/cm, (b) Refractive index change at the different fields in 75Å QW.

Table 4.1: Truth table for Fredkin gate at F=70, 100 kV/cm and κ=0.5, 0.6. The value in the square brackets represent the optical power at the respective ports.

Input1	Input2	Control (c)	κ=0.5, (c=1,F=70 kV/cm) Output1	Output2	κ=0.6, (c=1,F=100 kV/cm) Output1	Output2
0	0	0	0 [0]	0 [0]	0 [0]	0 [0]
0	0	1	0 [0]	0 [0]	0 [0]	0 [0]
0	1	0	0 [0.049]	1 [0.600]	0 [0.023]	1 [0.707]
0	1	1	1 [0.560]	0 [0.060]	1 [0.595]	0 [0.016]
1	0	0	1 [0.600]	0 [0.049]	1 [0.707]	0 [0.023]
1	0	1	0 [0.060]	1 [0.560]	0 [0.016]	1 [0.595]
1	1	0	1 [0.650]	1 [0.650]	1 [0.731]	1 [0.731]
1	1	1	1 [0.620]	1 [0.620]	1 [0.612]	1 [0.612]

It is obvious from Figure. 4.6 that the output intensities at the D port (output1) and

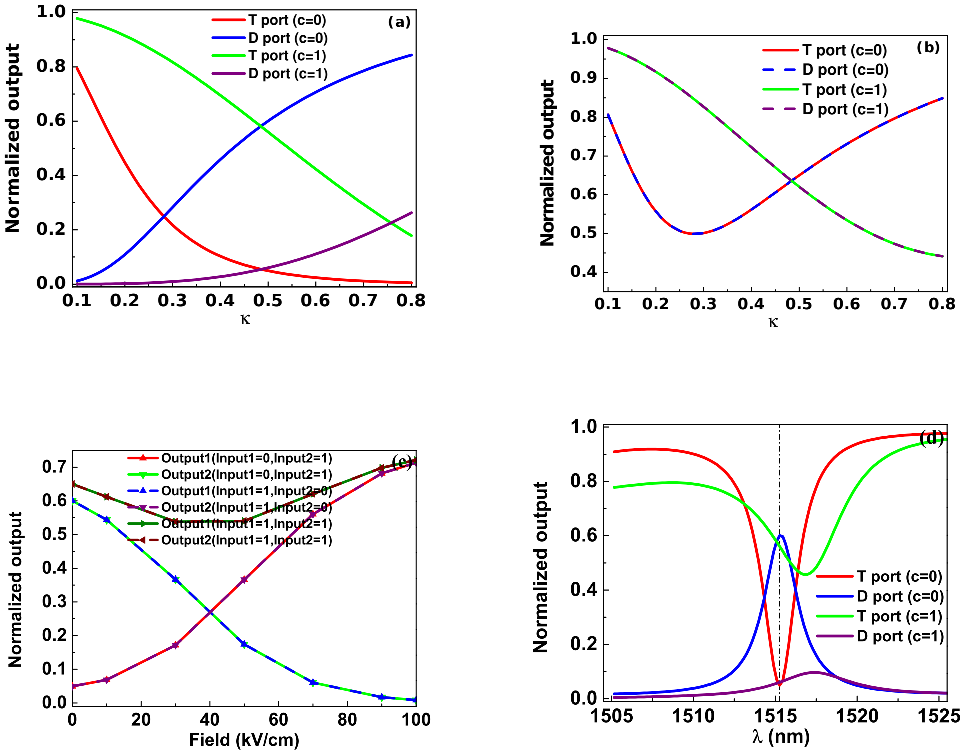

Figure 4.6: Normalized output power at all ports of the EA MRR based Fredkin gate versus (a) the coupling coefficient between ring and bus waveguide, with Input1=0, Input2=1 with c=1 as 70 kV/cm, λ_R=1515.27nm, (b) coupling coefficient between ring and bus waveguide, with Input1=1, Input2=1 with c=1 as 70 kV/cm, λ_R=1515.27nm, (c) as a function of applied field at different (Input1,Input2) combinations. (d) wavelength, with Input1=0, Input2=1 with c=1 as 70 kV/cm and κ=0.5 (Dotted line shows λ_R=1515.27nm).

the T port (output2) are highly dependent on the operating wavelength, the applied field and the coupling coefficients (between bus and ring waveguide). These parameters have to be optimally selected for the proposed MRR configuration to operate as a Fredkin gate. Note that the control signal in this case is in the electrical domain. As a large contrast between the 1 and 0 states is desired, a higher applied electric field is beneficial as illustrated in Figure. 4.6(c), which shows the normalized output power versus the applied field for a Fredkin gate configuration, for different input scenarios. For an applied field of 100 kV/cm, the optimum coupling coefficient is around 0.6, which ensures that a large contrast ratio is maintained between the T and D ports when the control signal is either ON (c=1, F=100 kV/cm) or OFF (c=0, F=0 kV/cm). The output intensity dependency on coupling coefficient for (Input1=1, Input2=0) is same as (Input1=0, Input2=1) with the output ports interchanged.

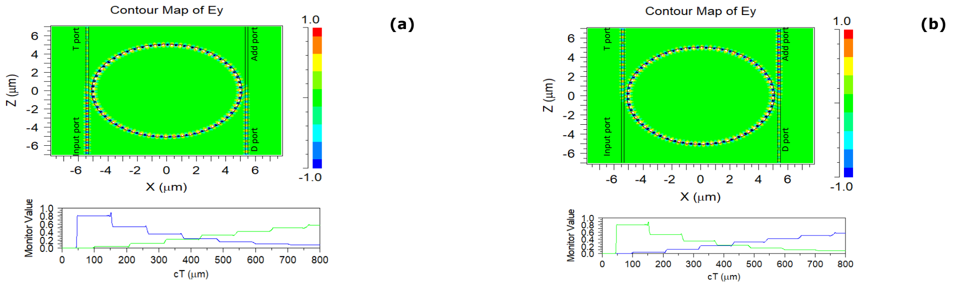

(a) control=0, Input1=1,Input2=0

(b) control=0, Input1=0,Input2=1

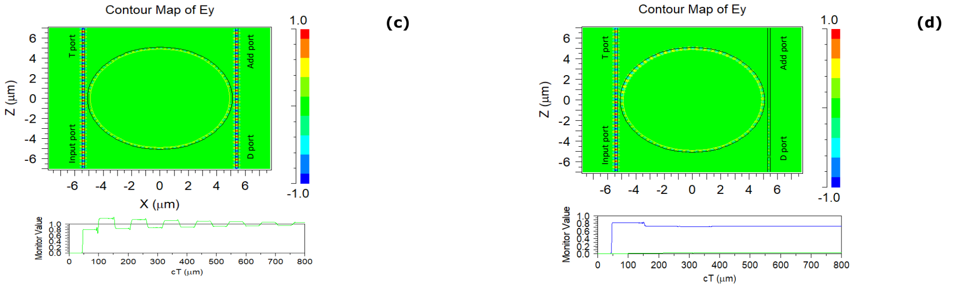

(c) control=0, Input1=1,Input2=1

(d) control=1, Input1=0,Input2=1

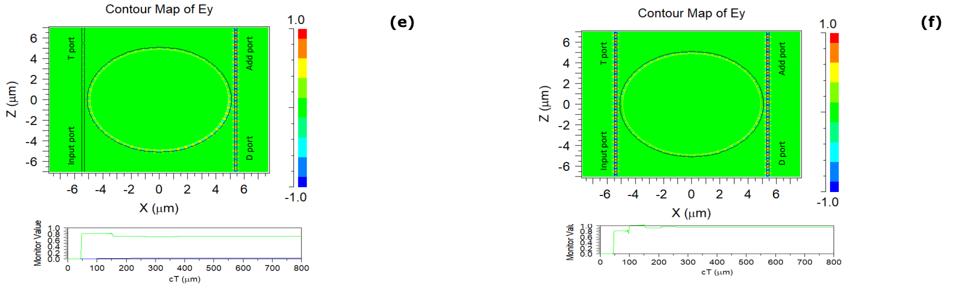

(e) control=1, Input1=0,Input2=1

(f) control=1, Input1=1,Input2=1

Figure 4.7: Rsoft Fredkin outputs with Input1 at input port, Input2 at add port, Output1 (green line) at D port and Output2 (blue line) at T port. (a) control=0, Input1=1,Input2=0 (b) control=0, Input1=0,Input2=1, (c)control=0, Input1=1,Input2=1 (d) control=1, Input1=0,Input2=1 (e) control=1, Input1=1,Input2=0 (f) control=1, Input1=1,Input2=1.

The proposed Fredkin configuration can also act as a buffer gate, a NOT gate, an AND gate and an OR gate, by suitably selecting the input signals, as shown in Table 4.1. For example, according to Table 4.1, when Input2 is at logic 0 and Input1 is at logic 1, the output at T port (output2) follows control signal, while the output at the D port is the inverted version of control signal. With Input1 as logic 0, Input2 and control can be considered as the inputs for an AND gate, Output1 (D port) will act as the output of the AND gate.

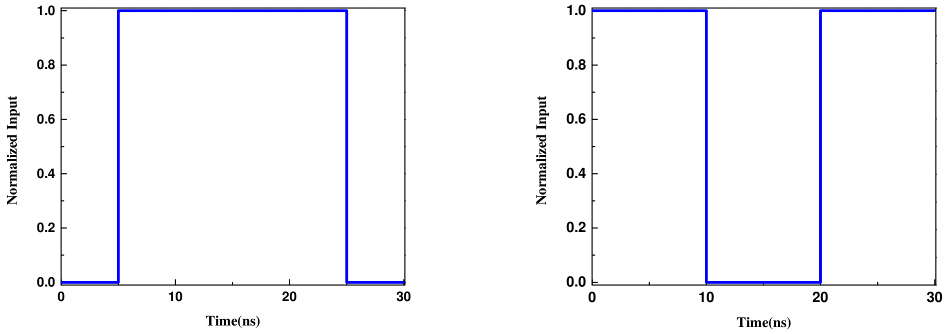

(a) Input1.

(b) Input2.

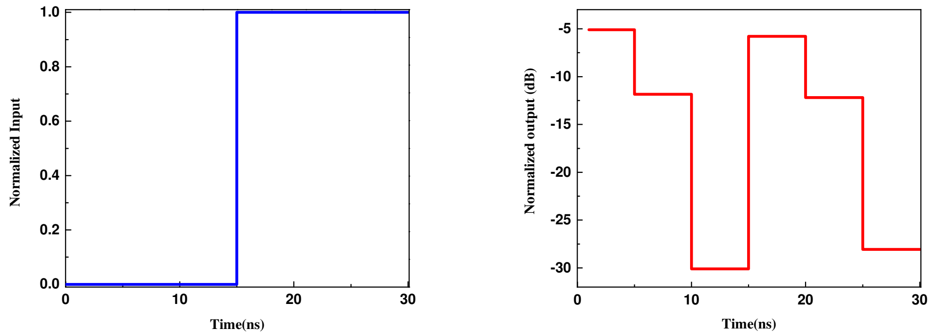

(c) Control signal.

(d) Output of T port in dB.

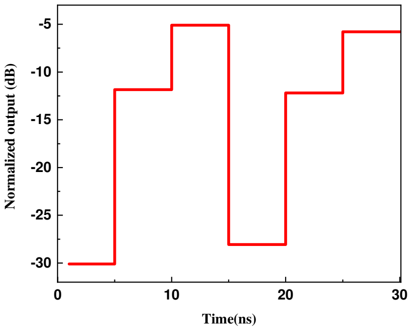

(e) Output of D port in dB.

Figure 4.8: Timing waveforms of EA MRR fredkin gateat F=70KV/cm and κ=0.5 (a) Input1 at input port (011110) (b) Input2 at add port (110011) (c) control signal on ring (000111) (d) Output2 (dB) at T port (110110) (e) Output1 (dB) at D port (011011).

The same configuration with Input1 as logic 1 would result in an OR gate whose output is obtained from the T port (Output2). The designed EA MRR Fredkin configuration is validated by simulating in Rsoft software and the corresponding results are illustrated in Figure 4.7. The results in Rsoft supports the working of SRR as Fredkin gate. The outputs (output1, output2) during input1=0 and input2=0 remains zero irrespective of the state of control signal. The timing waveforms of the EA MRR fredkin gate with bit period=5ns is shown in Figure 4.8. An envelope detector is required to be placed at the T port and D port for level estimation. The threshold level of the envelope detector is selected as 0.4 times of input amplitude.

4.3.2 Parallel MRR based AND and NAND gate outputs

The outputs of the AND and NAND gates based on EA MRR architecture (Figure. 4.2) are discussed in this section. The fields applied on the two rings of the parallel MRR act as the operands. The T port and the D port act as the AND output and the NAND output, respectively. The resonant wavelength is selected as 1515.27nm (resonant to the MRR at F=0 kV/cm).

Table 4.2: Truth table for the AND (T port) and NAND (D port) gates at F=100 kV/cm with κ=0.35 and κ=0.55. The value in the square brackets represent the optical power at the respective ports.

Input1 (Ring1)	Input2 (Ring2)	κ=0.35		κ=0.55	
		T port	D port	T port	D port
0 (0 kV/cm)	0 (0 kV/cm)	0 [0.057]	1 [0.574]	0 [0.010]	1 [0.796]
0 (0 kV/cm)	1 (100 kV/cm)	0 [0.135]	1 [0.382]	0 [0.026]	1 [0.664]
1 (100 kV/cm)	0 (0 kV/cm)	0 [0.135]	1 [0.336]	0 [0.026]	1 [0.468]
1 (100 kV/cm)	1 (100 kV/cm)	1 [0.735]	0 [0.069]	1 [0.439]	0 [0.032]

The dependency of output intensity (AND and NAND gate outputs) on the operating wavelength, coupling and applied field is shown in Figure. 4.9. It is seen that the MRR can operate as an AND gate and a NAND gate only at the resonance wavelength (at 0 kV/cm), which is around 1515.27nm. For an AND gate, the contrast ratio (CR) is defined as the intensity difference between the high and low state in the gate (CR1, CR2 and CR3 are the intensity differences between the outputs for (Input1, Input2)=(1, 1) and (Input1, Input2)=(0, 0), (Input1, Input2)=(1, 1) and (Input1, Input2)=(0, 1), (Input1, Input2)=(1, 1) and (Input1, Input2)=(1, 0), respectively). It is observed that for the AND gate, a coupling coefficient of κ=0.3 yields a large CR between the outputs, when the input field is 70 kV/cm (refer Figure 4.10), while κ=0.35 yields a large CR between the outputs, when the input

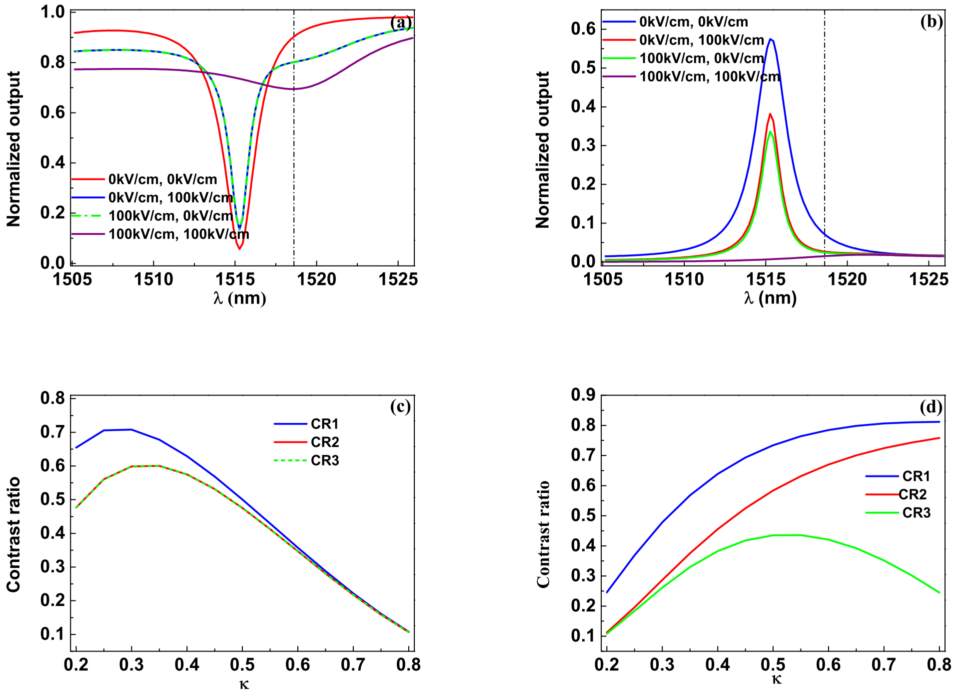

Figure 4.9: Wavelength and coupling coefficient dependency of a parallel EA MRR based AND/NAND gate. (a) Normalized T port power as a function of wavelength at various operands (field applied on rings) and κ=0.35. (Dotted line shows $\lambda = 1518.61nm$ which is resonant at F=100 kV/cm), (b) Normalized D port power as a function of wavelength at various operands and κ=0.35, (c) CR at T port as a function of coupling coefficient with applied field as 100 kV/cm, $\lambda_R = 1515.27nm$, (d) CR at D port as a function of coupling coefficient with applied field as 100 kV/cm, $\lambda_R = 1515.27nm$.

field is 100 kV/cm (refer Figure 4.9). For the NAND gate, a coupling coefficient of κ=0.5 yields a large CR between the outputs, when the input field is 70 kV/cm, while κ=0.55 yields a large CR between the outputs, when the input field is 100 kV/cm. It is observed that a trade off between the κ and applied field occurs to obtain high CR. and The truth table which depicts the power at the output ports for the AND and NAND gates at F=100 kV/cm are shown in Table 4.2, for κ=0.35 and κ=0.55.

We also investigated the option of implementing NOR and OR gates using parallel MRR (Figure. 4.2) with the EA mechanism for switching the states. For the parallel MRR, the applied voltage changes the refractive index of the ring in such a way that the resonant condition is satisfied for the input optical signal. With an applied field of 100 kV/cm to the rings, the change in the refractive index (Δn) is 0.0045, corresponding to a wavelength of

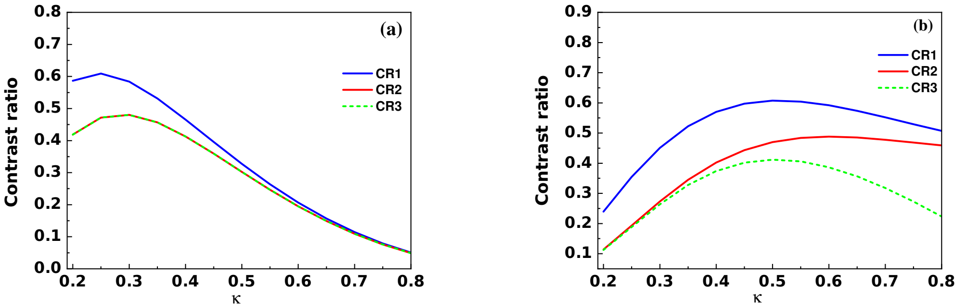

Figure 4.10: Coupling coefficient dependency of a parallel EA MRR based AND/NAND gate. (a) CR at T port as a function of coupling coefficient with applied field as 70 kV/cm, $\lambda_R = 1515.27nm$, (b) CR at D port as a function of coupling coefficient with applied field as 70 kV/cm, $\lambda_R = 1515.27nm$.

1518.61nm. At this wavelength, the configuration can act as NOR/OR gate.

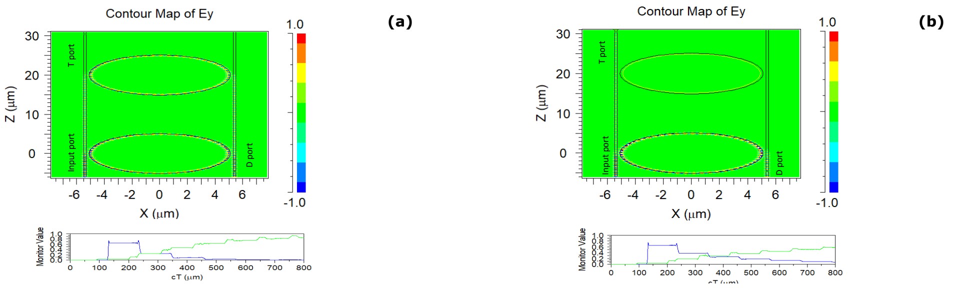

(a) Input1=0,Input2=0 (b) Input1=0,Input2=1

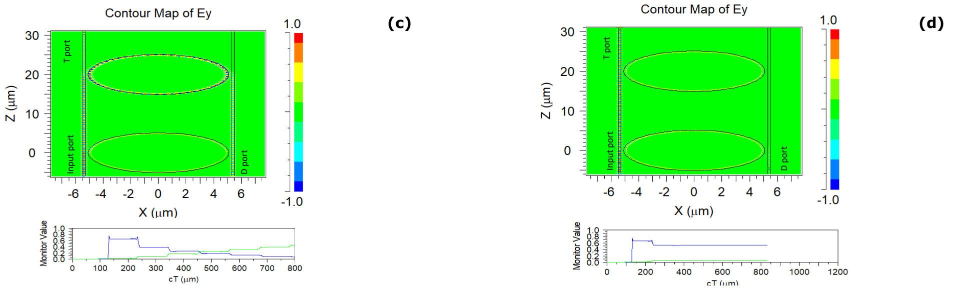

(c) Input1=1,Input2=0 (d) Input1=1,Input2=1

Figure 4.11: Rsoft parallel MRR AND/NAND outputs with Input1, Input2 as field applied on Ring1 and Ring2, AND output (blue line) at T port and NAND port (green line) at D port. (a) Input1=0,Input2=0 (b) Input1=0,Input2=1, (c) Input1=1,Input2=0 (d) Input1=1,Input2=1.

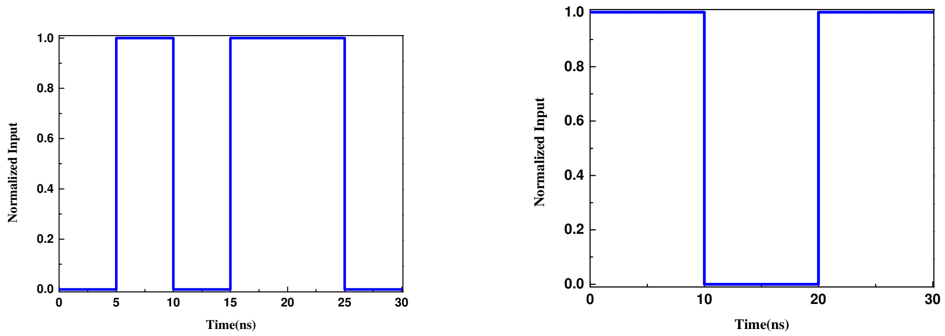

(a) Input1 (b) Input2.

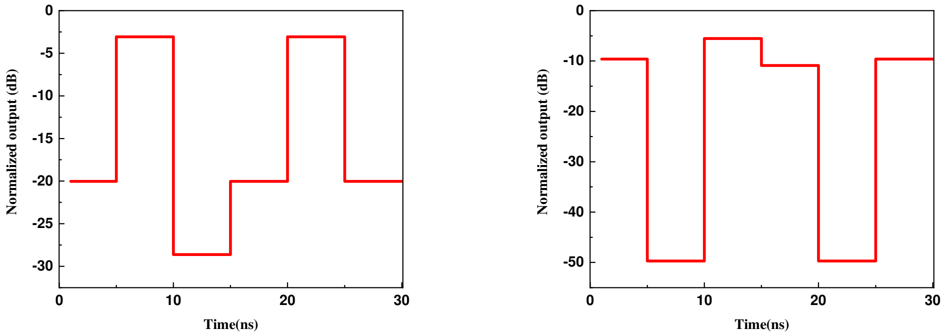

(c) Output of T port in dB. (d) Output of D port in dB.

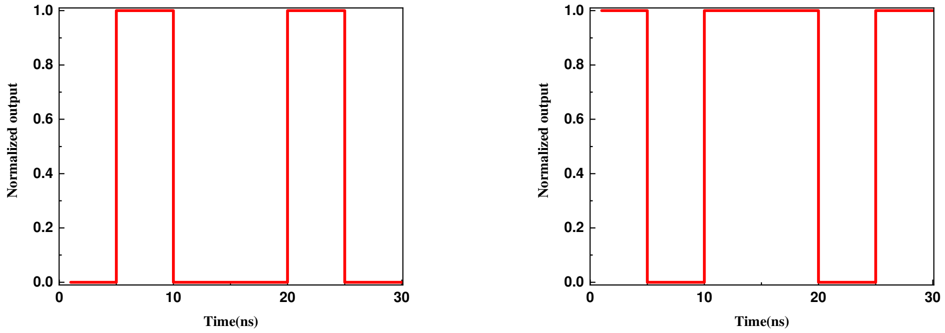

(e) Output of T port (AND gate). (f) Output of D port (NAND gate).

Figure 4.12: Timing waveforms at F=100KV/cm and κ=0.35 (a) Input1 (010110) (b) Input2 (110011) (c) AND output (dB) at T port (d) NAND output (dB) at D port (e) AND output (010010) at T port (f) NAND output (101101) at T port.

According to Figure. 4.9(a) and (b), at 1518.61nm, the parallel MRR configuration fails to act as NOR/OR gate due to a low CR between the states. A low CR is due to the fact that the signal satisfies the resonance condition and gets coupled to the MRR only with an applied electric field, where, at this condition, the absorption coefficient of the MRR becomes high ($499.721cm^{-1}$). The signal in the MRR therefore gets attenuated and the MRR now acts as a lossy resonator with a low quality (Q) factor.

The Rsoft outputs of EA parallel MRR AND/NAND gates at different cases is depicted in Figure 4.11 which supports the analysis made with the proposed configuration in Figure 4.2. The timing waveforms of EA parallel MRR AND/NAND is shown in Figure 4.12 with bit period of 5ns and threshold level is taken as 0.4 times the input amplitude.

4.3.3 XOR and XNOR gate outputs based on DRR and U-bent waveguides

Section 4.2.3 had explained the working mechanism of the XOR and XNOR gates implemented using DRR and U-bent waveguides, which use the EA mechanism for switching between states. The operands are the electric fields applied onto the rings and the XOR and XNOR outputs are collected at the T port and the D port of Ring2, respectively (refer to Figure. 4.3).

Table 4.3: Truth table for XOR and XNOR gate at F=100 kV/cm and κ=0.6. The value in the square brackets represent the optical power at the respective ports.

Input1 (Ring1)	Input2 (Ring2)	XOR (T port)	XNOR (D port)
0 (0 kV/cm)	0 (0 kV/cm)	0 [0.067]	1 [0.534]
0 (0 kV/cm)	1 (100 kV/cm)	1 [0.445]	0 [0.050]
1 (100 kV/cm)	0 (0 kV/cm)	1 [0.445]	0 [0.050]
1 (100 kV/cm)	1 (100 kV/cm)	0 [0.039]	1 [0.370]

The launched signal at the input port has a wavelength of 1515.27nm (resonant to the MRR at zero applied field). The length of long U-bent and short U-bent waveguides are selected as $6\pi R$ and $2\pi R$, respectively, in order to ensure zero phase difference for the signal before and after entering the U-bent waveguide. The CR variation at the output ports of Ring2 versus the coupling coefficient is shown in Figure. 4.13 (a) and (b), respectively. Note that for κ=0.6, high CR is obtained for all states for both XOR and XNOR logic gates at λ_R=1515.27nm.

The power variations at the output T and D ports of Ring2 for different control signals (different applied electric fields) are shown in Figure. 4.13(c) and (d), respectively. The

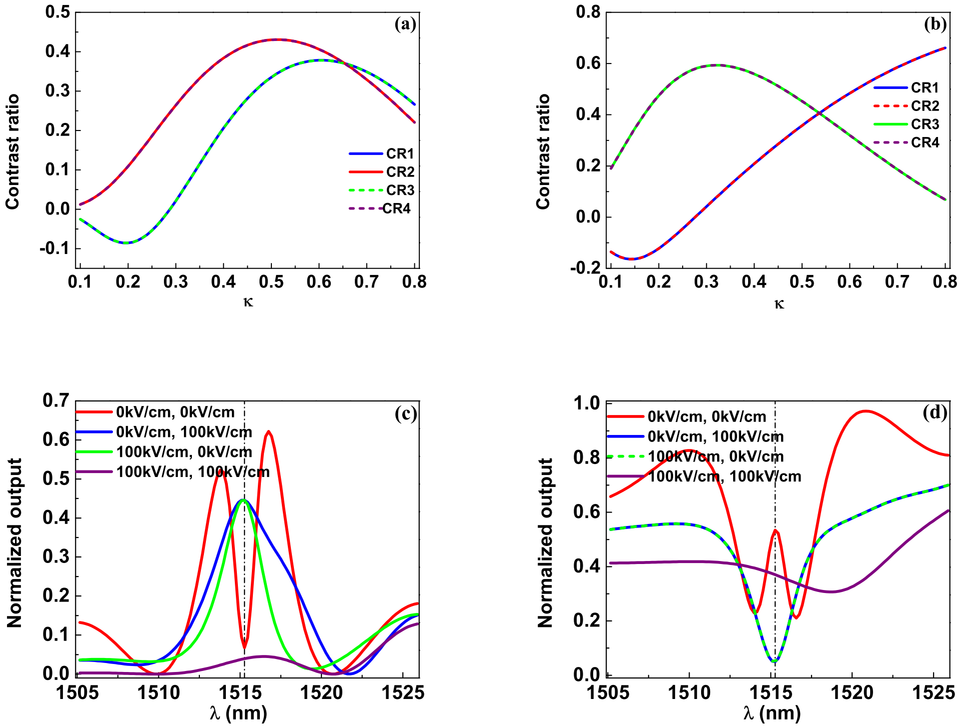

Figure 4.13: Coupling and wavelength dependency of the EA MRR and U-bent waveguides-based XOR and XNOR gates at F=100 kV/cm. The dotted straight line indicates λ_R=1515.27nm. (a) CR at T port of Ring2 versus the coupling coefficient at λ_R=1515.27nm, (b) CR at D port of Ring2 versus the coupling coefficient at λ_R=1515.27nm, (c) Normalized T port power of Ring2 versus wavelength at various operands (fields applied on the rings) and κ=0.6., (d) Normalized D port power of Ring2 versus wavelength at various operands and κ=0.6.

output contrast ratios CR1-4 of the XOR gate shown in Figure. 4.13(a) are the intensity difference between the outputs of logical inputs (0,1) and (0,0), (0,1) and (1,1), (1,0) and (0,0), (1,0) and (1,1), respectively. Note that, the output of the XOR gate is taken from the T port of Ring2. The contrast ratios CR1-4 for the XNOR gate plotted in Figure. 4.13(b) are defined the intensity difference between the outputs of logical inputs (0,0) and (0,1), (0,0) and (1,0), (1,1) and (0,1), (1,1) and (1,0), respectively. The truth table for the XOR and XNOR gates for a coupling coefficient of 0.6 is depicted in Table 4.3. EA MRR can act as triple input XOR and XNOR gates by feeding the outputs of two input EA MRR XOR/XNOR gates into a fredkin gate based on EA SRR and the field on the fredkin ring as the third input. The truth table of EA MRR based triple input XOR and XNOR is depicted in Table 4.4 with F=100KV/cm and κ=0.55, input port and add port of Fredkin is fed with output of 2 input XOR and XNOR respectively. Optical amplifiers placing at the output stage of two input XOR/XNOR gate (before feeding into Fredkin gate) in EA MRR triple input XOR XNOR gate helps to improve the CR.

Table 4.4: Truth table for triple input XOR and XNOR gate at F=100KV/cm and κ=0.55 and λ=1515.27nm

Input1	Input2	Input3	XOR	XNOR
0 (0 KV/cm)	0 (0 KV/cm)	0 (0 KV/cm)	0 (0.138)	1 (0.380)
0 (0 KV/cm)	0 (0 KV/cm)	1 (100 KV/cm)	1 (0.350)	0 (0.099)
0 (0 KV/cm)	1 (100 KV/cm)	0 (0 KV/cm)	1 (0.350)	0 (0.099)
0 (0 KV/cm)	1 (100 KV/cm)	1 (100 KV/cm)	0 (0.069)	1 (0.325)
1 (100 KV/cm)	0 (0 KV/cm)	0 (0 KV/cm)	1 (0.349)	0 (0.099)
1 (100 KV/cm)	0 (0 KV/cm)	1 (100 KV/cm)	0 (0.069)	1 (0.325)
1 (100 KV/cm)	1 (100 KV/cm)	0 (0 KV/cm)	0 (0.069)	1 (0.325)
1 (100 KV/cm)	1 (100 KV/cm)	1 (100 KV/cm)	1 (0.307)	0 (0.046)

4.3.4 Triple-MRR based OR and AND gate outputs

As discussed in Section 4.2.4, an OR gate along with an AND gate can be simultaneously realized in a triple ring MRR that uses the EA mechanism for state switching. The input optical signal of 1515.27nm launched at the input port of Ring1 and add port of Ring2 satisfies the resonance condition with no field applied onto the rings.

Table 4.5: Truth table for AND (T port) and OR (D port) gate based on triple MRR. The value in the square brackets represent the optical power at the respective ports.

Input1 (Ring1)	Input2 (Ring2)	Input1 on ring3		Input2 on ring3	
		T port	D port	T port	D port
0 (0 kV/cm)	0 (0 kV/cm)	0 [0.043]	0 [0.043]	0 [0.043]	0 [0.043]
0 (0 kV/cm)	1 (100 kV/cm)	1 [0.414]	0 [0.092]	0 [0.058]	1 [0.586]
1 (100 kV/cm)	0 (0 kV/cm)	1 [0.586]	0 [0.058]	0 [0.092]	1 [0.414]
1 (100 kV/cm)	1 (100 kV/cm)	1 [0.590]	1 [0.590]	1 [0.590]	1 [0.590]

The CR variations at the output T and D ports of Ring3 (T port for OR and D port for AND with the field applied onto Ring3 being the same as that applied onto Ring1) versus the coupling coefficient are shown in Figure. 4.14(a) and (b), respectively. The output contrast ratios CR1-3 of the OR gate shown in Figure. 4.14(a) are the intensity difference between the outputs of logical inputs (1,1) and (0,0), (1,1) and (0,1), and (1,1)

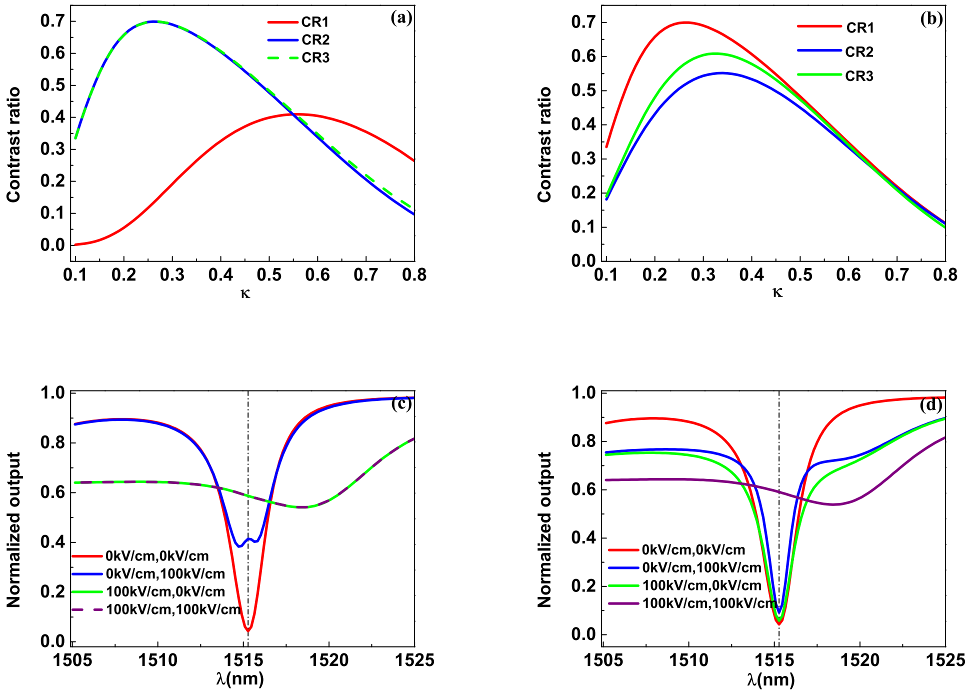

Figure 4.14: Wavelength and coupling dependency of triple EA MRR based OR and AND gates with Ring3 fed with Input1. (a) CR at the T port of Ring3 versus the coupling coefficient for an applied field of 100 kV/cm and λ_R=1515.27nm, (b) CR at the D port of Ring3 versus the coupling coefficient for an applied field of 100 kV/cm and λ_R=1515.27nm, (c) Normalized T port power of Ring3 versus wavelength for various operands (field applied on rings), with κ=0.45, (d) Normalized D port power of Ring3 versus wavelength for various operands, with κ=0.45. (Dotted vertical line shows λ_R=1515.27nm).

and (1,0), respectively. The contrast ratios for the AND gate (shown in Figure. 4.14(b)) are defined in Section 3.2. For κ=0.45, high CRs are obtained for all the states, for both the OR and AND logic gates, and thus the optimum coupling coefficient between the ring and waveguide is selected as 0.45. The power variation at the output T and D ports of Ring3 for different control signals (different applied electric field) is shown in Figure. 4.14 (c) and (d), respectively. Table 4.5 provides the output intensities for the proposed OR and AND gates are based on MRR configurations with the field applied onto Ring 3 being the same as the one applied onto Ring 1 and Ring2, with operating wavelength as 1515.27nm and κ=0.45. The same MRR configuration can be used to realize NAND/NOR gates at the output ports by launching a wavelength which satisfies resonant condition at non-zero field applied on the rings. But the poor Q factor due to absorption effect leads to the failure of realizing NAND/NOR gates using EA triple MRR configuration. In reference [53], OR and AND logic gates are realized using parallel double ring MRR. This configuration could only realize the logic gate at different resonant condition of the rings. The zero bias applied on the ring when satisfies the resonant condition in the MRRs of the configuration leads to OR gate realization while non-zero bias applied on the ring when satisfies the resonant condition in the MRRs leads to AND gate realization. The proposed triple parallel MRR configuration using electroabsorption modulation can successfully realize OR and AND gates simultaneously at the T port and D port when the MRR satisfies resonant condition at zero field applied on the rings

4.4 Conclusion

In this chapter, we proposed and simulated the performances of logic gates based on EA based MRRs employing QWs in the intrinsic region of p-i-n heterostructure diodes as the light guiding media. Simulation results have shown that the absorption in the QWs can be varied through external applied fields, which change the state of the logic gates. Using MRRs, we succeeded in implementing Fredkin logic gate; a universal gate suitable for reversible computing, whereby the states are changed through the EA mechanism. When realizing two input AND gate using MRR based Fredkin gate, one of the input is in the optical domain while the other is in the electrical domain. It is always advantageous for a Fredkin gate to have both the input signals in the same domain. To accomplish this, we have proposed a parallel EA double ring resonator in which AND as well as NAND outputs can be simultaneously obtained at the output T port and the D port, respectively.

While implementing OR and NOR gates using parallel MRRs in conjunction with the EA mechanism, we also found that the reduction in the Q factor of the rings at an applied field, due to higher absorption, leads to a poor contrast ratio between the various output states, making the realization of OR and NOR gates impractical. A novel triple ring configuration has also been proposed, for the first time, which can simultaneously realize AND and OR gates through the EA mechanism. Implementation of XOR and XNOR gates using two EA MRRs along with U-bent waveguides was verified. Most importantly, our simulation results have also revealed that all the proposed logic gates can only be realized by optimizing the coupling coefficient, operating wavelength and applied field. The EA MRR optical logic gates have the potential to achieve faster switching and integrate higher device density. The hybrid architecture of the proposed EA MRR logic gates, with the control signal being in the electrical domain and controlled signal in the optical domain, takes advantage of the key attributes of both domains, making them advantageous for their use in futuristic photonic integrated circuts and optical signal processing.

Chapter 5

Design and optimization of bias assisted carrier injective MRR logic gates

5.1 Introduction

Optical logic gates are the key elements needed to realize high speed optical signal processing systems and optical computing. Hardy and Shamir [48] introduced a new platform in signal processing, which simultaneously enables high speed operation and control convenience. The high-speed and control benefits of optics and electronics can be collectively used to develop electro-optics-based logic circuits whereby electrons and photons are used for signal control/switching and signal operation, respectively [49]. Optical directed logic gates open up computational parallelism, thus lead to higher packaging density in integrated circuits (ICs). Performing optical operations independently on each switching element in a network enables boolean logic functions to be realized with reduced latency and over-all processing time. Optical logic gates based on III-V semiconductors are highly recommended for monolithic integration with other III-V devices (e.g., lasers, photodetectors, amplifiers, etc.) in chip platform. To enable control/switching in logic gates, several switching mechanisms such as electro-optic (EO) effect [50, 57], electro-absorption (EA) effect [58] and thermo-optic (TO) effect [51] can be used. However, each of these mechanisms has its own drawbacks. The EO effect is relatively weak in III-V semiconductors, and hence, the length of an EO device must be long enough in order to attain a large change in optical output with a practical applied bias voltage, which makes it incompatible for chip integration. EA based logic gates are polarization sensitive and the wavelength operation of these devices should be chosen near the bandgap of the material as EA effect is strongest only for those wavelengths that are near the bandedge wavelength. Group III-V semiconductor materials with bandgap close to lowest attenuation and dispersion wavelength window (around 1300nm and 1550nm, respectively) are Indium-based ternary and quaternary materials, such as InAlAs/InGaAs and InGaAsP/InP. The major drawbacks of these materials are their scarcity and immature processing technologies. The TO based logic gates faces thermal mismatch issues along with poor stability and reliability. An alternative switching mechanism that works well with III-V semiconductor materials is carrier injection (CI)[59]. The major attractive features of CI mechanism are polarization independent nature, operational simplicity, high contrast ratio and freedom to operate over a wavelength band far away from the bandgap. Through a bias-assisted CI mechanism, varying the bias voltage applied to the III-V semiconductor material changes its refractive index through bandfilling (BF), bandgap shrinkage (BGS) and free carrier absorption (FCA) effects. The limitation faced by CI modulation-based devices implemented using Mach Zehnder Interferometer and directional coupler structures in ICs is their bulky nature [35, 60]. However, a solution that overcome this limitation is to use microring resonator (MRR) structures [21].

In this chapter, we are introducing a novel bias assisted CI based p-i-n diode embedded parallel triple MRR configuration to simultaneously realize OR and AND gates at the output ports (T port and D ports) during resonant wavelength (resonant at zero bias) launched at the input ports. The bias on the rings act as the operands while the operational results are collected at the respective output ports. The performance of the proposed configuration is optimized using the applied bias on MRRs, intrinsic region width, relaxation time of carriers and coupling coefficient between ring and bus waveguides. Launching a wavelength which satisfies resonant condition at non-zero bias, at the input ports of this proposed configuration can lead to the simultaneous realization of NOR and NAND gates at the respective output ports. We already discussed in Chapter 4 about the failure of EA parallel DRR configuration to work as NOR and OR gate due to low Q factor. The same proposed parallel DRR configuration can work as AND and NAND gate or NOR and OR gate by implementing CI modulation mechanism. The results corresponding to the operation of CI based parallel DRR is also discussed in this chapter. All the MRR logic gate configurations discussed in Chapter 4 can operate successfully by incorporating CI modulation mechanism instead of EA modulation.

5.2 Modeling of carrier injective parallel triple ring resonators based optical gates

The perspective view of the proposed logic gate configuration is shown in Figure 5.1. The structure consists of three identical parallel rings of identical radii, R, seperated by a sufficient minimum gap that the cross coupling between the individual rings is negligible. The entire logic gate structure is grown on a GaAs substrate. The device is comprised of p-i-n diodes having GaAs intrinsic (i) regions, which act as light carrying media (core regions), and surrounding p-AlGaAs and n-AlGaAs regions, which have lower refractive indices than the intrinsic region and act as claddings that confine the optical signal to the intrinsic regions (cores). Injection of carriers into i-GaAs is enabled by depositing p and n electrodes on the top of the rings and beneath the GaAs substrate. Since the bandgap wavelength of the GaAs material is typically far less than the low attenuation and dispersion wavelengths, efficient operation can be attained at these long wavelengths. The material exhibits appreciable refractive index change with a small applied bias voltage. Unlike silicon-based logic gate devices, GaAs-based devices enable monolithic integration with other semiconductor optoelectronic devices. The injection of carriers in a forward-biased ring resonator structure induces a refractive index change that shifts the resonant wavelength, thus routing a portion of optical signal launched into the input port to the T and D ports of the subsequent MRRs. The resulting intensity variation at the T port and D port of MRR3 (refer to Figure 5.1) leads to the realization of OR/AND and NAND/NOR gates. The principle of operation and realization of OR and AND or NAND and NOR gates using carrier injective p-i-n

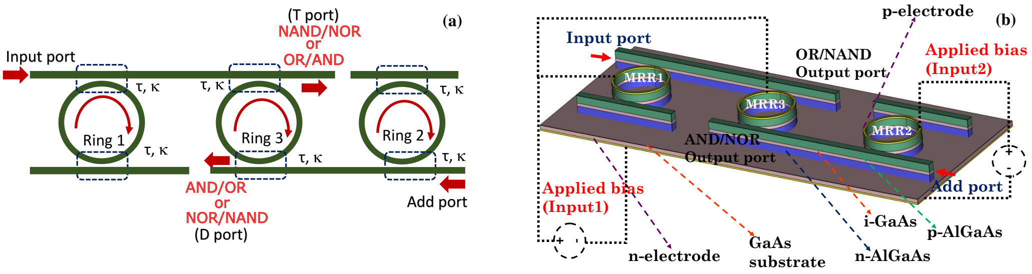

Figure 5.1: (a) Parallel triple ring MRR configuration for OR/AND and NOR/NAND gate realization. (b) Perspective view of MRRS for realizing OR/AND and NOR/NAND gate based on CI. The T port of MRR3 acts as an OR gate and the D port as an AND gate at zero bias for the resonant signal. The T port of MRR3 acts as a NAND gate and D port as a NOR gate at a non-zero bias (the bias applied on MRR3 is same as MRR1).

embedded parallel triple ring resonators are discussed below:

5.2.1 Principle of operation of carrier injective p-i-n diode embedded MRRs

Applying through the electrodes, forward biases to the p-i-n structured MRRs results in electron and hole injection into the intrinsic regions. The change in refractive index in the i-GaAs is attributed to the change in absorption associated with BF (Burstein-Moss phenomenon, i.e. bandgap of a semiconductor material increases as the absorption edge is shifted to higher energies due to conduction band state population.), BGS and FCA (plasma effect) due to the injected carriers [34]. Note that, BF and BGS are interband absorption effects while FCA is intraband absorption effect. In the following calculations of switching characteristics, the band shapes are assumed to be parabolic. By injecting carriers, photons of energies slightly greater than the nominal bandgap energy (E_g) experience lower absorption because the electrons and holes fill the conduction and valance band, thus leading to the BF effect. The BGS effect happens when the injected carrier concentration density exceeds the critical carrier concentration density (material parameter dependent). This effect lowers the conduction band edge and increase the valance band edge, thus shrinking of the bandgap energy , which increases the absorption for photon of energies less than the nominal bandgap energy. Note that, while calculating the BF effect, the change in the band gap due to BGS must also be included and typically the contributions of the BF and BGS effects can be combined together in the calculations [44]. The critical carrier density estimation (χ_{cr}) and bandgap energy reduction ($\Delta E_g(\chi)$) is modeled according to [34, 61]. The resulting change in absorption ($\Delta\alpha(\chi,\, E)_{BF+BGS}$) due to the combined BF and BGS effects is expressed as a function of carrier density (χ) in i-GaAs and photon energy (E) as [44]:

$$\begin{aligned}\Delta\alpha(\chi, E)_{BF+BGS} = \frac{C_{hh}}{E}((f_v(E_{ah})) - (f_c(E_{bh})))\sqrt{E-(E_g-\Delta E_g(\chi))} \\ +\frac{C_{lh}}{E}((f_v(E_{al})) - (f_c(E_{bl})))\sqrt{E-(E_g-\Delta E_g(\chi))} - (\frac{C_{hh}}{E}\sqrt{E-E_g} + \frac{C_{lh}}{E}\sqrt{E-E_g})\end{aligned} \tag{5.1}$$

Here, E_{ah} and E_{bh} denotes the state of energy levels in valance band and conduction band by considering heavy holes, while E_{al} and E_{bl} denotes the state of energy levels in valance band and conduction band by considering light holes respectively. The Fermi-Dirac probability distribution function in these respective states are represented by f_v and f_c. The constants (C$_{hh}$ and C$_{lh}$) are obtained from [34] by correcting with a multplicative term $\sqrt{\hbar}$ and units as cm^{-1}eV. The change in absorption is accompanied by a change in refractive index (Δn$_{BF+BGS}$) and it can be calculated by applying Kramers-Kronig integration to Eq.(1) and substituting the appropriate Cauchy principal value. The maximum change in refractive index due to BF and BGS occurs near the bandgap region and become negligible for photon energies much less than the bandgap energy.

FCA is due to the absorption of photons by free carriers (electrons and holes) and the intraband transition of free carriers occuring from one energy state to a higher energy state. FCA-based refractive index change (Δn_{FCA}) dominates at lower photon energies or higher operating wavelengths, since Δn$_{FCA}$ is proportional to the square of the operating wavelength. Δn$_{FCA}$, which depends on the injected electron and hole densities ($\chi_{e,p}$), refractive index (n) and propagating wavelength through the core i-GaAs region, is given as

$$\Delta n_{FCA} = -\frac{e^2\lambda^2}{8\pi^2 c^2 \epsilon_0 n}\left(\frac{\chi_e}{m_e} + \frac{\chi_p}{m_p}\right) \tag{5.2}$$

where e, c, ϵ_0, m$_e$ and m$_p$ are the electronic charge, velocity of light in free space, free space permittivity and effective masses of electron and holes, respectively. The total change in refractive index (Δn$_{total}$) is the sum of the Δn$_{BF+BGS}$ and Δn$_{FCA}$.

5.2.2 Realization of triple parallel MRRs based optical logic gates

Incorporating the CI modulation mechanism into the proposed triple parallel MRRs configuration leads to realization of different logic gates. The launched resonant photon energy of the signal at the input port of MRR1 and add port of MRR2 in the proposed configuration is selected to be far less than bandgap energy of the intrinsic region in the rings. Three identical rings are used in the proposed configuration shown in Figure 5.1, where L is the circumference of each of the rings. The input power of the launched light signal is denoted as P_I and the normalized output power levels at the T port of MRR1 (ring1) and D port of MRR2 (ring2) are represented as P_{T1} and P_{D2} respectively. MRR3 acts as a Fredkin gate with the T port output of Ring1 fed as an input into the input port of Ring3 and the add port of Ring3 fed with the D port output of Ring2 [55]. The normalized power levels at T1 and D2 ports are given by

$$P_{T1,D2} = \left| \tau + \frac{(i\kappa)^2 \tau \exp\left(\frac{i2\pi L n_{1,2}}{\lambda} - \alpha L\right)}{1 - \tau^2 \exp\left(\frac{i2\pi L n_{1,2}}{\lambda} - \alpha L\right)} \right|^2 \tag{5.3}$$

while P$_{T3}$ and P$_{D3}$ are the normalized powers at T port and D port of MRR3 (ring3) and are given by

$$P_{T3} = \left|\tau + \frac{(i\kappa)^2\tau \exp\left(\frac{i2\pi L n_3}{\lambda} - \alpha L\right)}{1 - \tau^2 \exp\left(\frac{i2\pi L n_3}{\lambda} - \alpha L\right)}\right|^2 \times P_{T1} + \left|\frac{(ik)^2 \exp\left(\frac{i\pi L n_3}{\lambda} - \alpha L/2\right)}{1 - \tau^2 \exp\left(\frac{i2\pi L n_3}{\lambda} - \alpha L\right)}\right|^2 \times P_{D2} \tag{5.4a}$$

$$P_{D3} = \left|\tau + \frac{(i\kappa)^2\tau \exp\left(\frac{i2\pi L n_3}{\lambda} - \alpha L\right)}{1 - \tau^2 \exp\left(\frac{i2\pi L n_3}{\lambda} - \alpha L\right)}\right|^2 \times P_{D2} + \left|\frac{(ik)^2 \exp\left(\frac{i\pi L n_3}{\lambda} - \alpha L/2\right)}{1 - \tau^2 \exp\left(\frac{i2\pi L n_3}{\lambda} - \alpha L\right)}\right|^2 \times P_{T1} \tag{5.4b}$$

The refractive indices of the rings (n$_1$ for Ring1, n$_2$ for Ring2, n$_3$ for Ring3) is n_{eff} at zero applied, and changes to n_{eff}-Δn_{total} at an applied bias. Note that the add port of Ring1 must be isolated from the input port of Ring2 as shown in Figure 5.1 to restrict the entry of any optical signal through the add port of Ring1, which can result in nonfunctioning of the gates. The bias voltage applied to Ring1 and Ring2 is considered as the operands, and the logic output is collected as light intensities at the T port and the D port of Ring3. An optical signal which is resonant either at zero bias or at an applied bias is continuously launched through the input port of Ring1 and the add port of Ring2, depending whether an OR/AND or a NAND/NOR function is needed. The bias applied to Ring3 controls the ports through which OR/AND and NAND/NOR functions are obtained. If the bias applied to Ring3 is same as that applied to Ring1, then, depending on whether the launched optical signal is resonant at zero bias or non-zero bias, an OR or a NAND gate is realized at the T port of Ring3, while the D port of Ring3 realizes the AND or NOR gate, respectively. If the bias applied on Ring3 is same as that applied to Ring2, then an OR or a NAND gate is realized at the D port of Ring3, while the T port of Ring3 realizes an AND or a NOR gate, respectively.

The operation of the device as a logic gate is subsequently described. Here, we considered that the applied bias on Ring3 is the same as that on Ring1. Also consider that $\lambda = \lambda_{0R}$ is the wavelength which satisfies resonance condition with zero bias being applied to the rings, while $\lambda = \lambda_{1R}$ satisfies the resonance condition when the rings are biased with a non-zero voltage.

Case 1: (Input1=0, Input2=0, $\lambda = \lambda_{0R}$): A zero bias applied to Ring1 and Ring2 results in resonance conditions at Ring1, Ring2 and Ring3 for optical signals of wavelength λ_{0R} launched into the input port of MRR1 and the add port of MRR2. This scenario results in low optical intensities (logic 0) at the T port and the D port of Ring3, as no input optical signals enter into the ports of Ring3.

(Input1=0, Input2=0, $\lambda = \lambda_{1R}$): A zero bias applied to Ring1 and Ring2 results in non-resonance conditions at Ring1, Ring2 and Ring3 for optical signal of wavelength λ_{1R} launched into the input port of MRR1 and the add port of MRR2. This scenario results in high optical intensities (logic 1) at the T port and the D port of Ring3.

Case 2: (Input1=0, Input2=1, $\lambda = \lambda_{0R}$): When the optical signals of wavelength λ_{0R} are launched at the input port of Ring1 and the add port of Ring2, a non-zero bias applied to Ring2 (i.e., MRR2 becomes out of resonance, thus bypassing Ring2) yields a high-intensity optical signal at the drop port of Ring2. The drop port of Ring2 is connected to the add port of Ring3, and thus, the optical signal launched into the add port of Ring2 couples into Ring3 (Ring3 is at resonance as no bias is applied onto it) and appears at the T port of Ring3, resulting in a high-intensity optical signal (logic 1) at the T port and a low-intensity optical signal (logic 0) at the D port of Ring3 (as the T port intensity of MRR1 is low).

(Input1=0, Input2=1, $\lambda = \lambda_{1R}$): When optical signals of wavelength λ_{1R} launched at the input port of Ring1 and the add port of Ring2, a non-zero bias applied on Ring2 (i.e., MRR2 becomes resonant, thus couples to Ring2) yields a high-intensity optical signal at the T port of Ring2. A zero bias applied to Ring1 makes MRR1 out of resonance, yielding a high-intensity optical signal at the T port of MRR1. Since the T port of MRR1 is connected to the input port of Ring3, as Ring3 is driven with the same bias as Ring1, MRR3 becomes out of resonance, and this results in a high-intensity optical signal (logic 1) at the T port of MRR3 and a low-intensity optical signal (logic 0) at the D port of MRR3.

Case 3: (Input1=1, Input2=0, $\lambda = \lambda_{0R}$): A non-zero bias applied to Ring1 (i.e., MRR1 becomes out of resonant, thus bypasses Ring1) yields a high-intensity optical signal at the T port of Ring1. Since the T port of Ring1 is connected to the input port of Ring3, the optical signal launched into the input port of Ring1 bypasses Ring3 (Ring3 is out of resonance, as a non zero bias is applied onto it) and appears at the T port of Ring3, resulting in a high-intensity optical signal (logic 1) at the T port and a low-intensity optical signal (logic 0) at the D port of Ring3 (since the optical signal intensity at the D port of MRR2 is low and at the T port is high).

(Input1=1, Input2=0, $\lambda = \lambda_{1R}$): A non-zero bias applied to Ring1, at which MRR1 becomes resonant, yields a high-intensity optical signal at the D port of Ring1. A zero bias applied to Ring2 drives MRR2 out of resonance and thus, a high-intensity optical signal appears at the D port of MRR2 and the intensity of optical signal at T port of MRR2 becomes low. As the D port of MRR2 is connected to the add port of Ring3, when both Ring3 and Ring1 share the same bias, MRR3 is driven into resonance, yielding a high-intensity optical signal (logic 1) at the T port and a low-intensity signal (logic 0) at the D port of MRR3.

Case 4: (Input1=1, Input2=1, $\lambda = \lambda_{0R}$): A non-zero bias applied to both Ring1 and Ring2 results in non-resonance conditions for MRR1 and MRR2, and hence, zero bias resonant-wavelength signals launched at the input port of Ring1 and the add port of Ring2 bypass Rings 1, 2 and 3, yielding high-intensity optical signal (logic 1) at both the T port and the D port of Ring3.

(Input1=1, Input2=1, $\lambda = \lambda_{1R}$): A non-zero bias applied to both Ring1 and Ring2 drive them into resonance, and hence, non-zero bias resonant-wavelength signals launched to the input port of MRR1 and the add port of MRR2 couple into Rings 1 and 2, and appear at the D port of MRR1 and the T port of MRR2, resulting in low-intensity optical signals (logic 0) at both the T port and the D port of MRR3.

The above-described operations of the proposed triple parallel MRR based logic gate configuration demonstrate its ability to realize OR and AND gate at T port and D port for a zero bias resonant wavelength λ_{0R} or NAND and NOR gate at T port and D port for a non-zero bias resonant wavelength λ_{1R}, respectively.

5.2.3 Realization of carrier injective parallel DRR based logic gates

The parallel DRR configuration to realize AND and NAND gates simultaneously at the T port and D port are discussed in Figure 4.2 of Chapter 4. EA modulation mechanism fails to simultaneously realize OR and NOR gates on the same proposed configuration due to low Q factor and high absorption during an applied bias condition (operand as logic 1) on the rings (Ring1 and Ring2), resulting in low CR for OR and NOR gate outputs. Implemeting CI mechanism to change the refractive index of rings in response to applied bias has succeeded to simultaneously realize AND and NAND or NOR and OR gates at the output ports depending up on the nature of launched wavelength at the input port. If the launched wavelength satisifes resonant condition at zero bias (operand as logic 0) leads to AND gate output at T port and NAND gate output at D port. If the launched wavelength satisfies resonant condition at non-zero bias (operand as logic 1), then T port yields NOR gate output while D port yields OR gate output respectively. The normalized output power at T port and D port of a parallel DRR is expressed as

$$P_T = \left|\tau^2\bar{C} + \sqrt{\phi_1}\bar{C}\tau j\kappa\Gamma + \phi_2 j\kappa\tau(\alpha + \beta\Gamma)\right|^2 \tag{5.5a}$$

$$P_D = \left|(j\kappa)^2\sqrt{\phi_1} + j\kappa\tau\bar{C}\sqrt{\phi_2}\alpha + (j\kappa\tau\phi_1 + \tau\bar{C}j\kappa\sqrt{\phi_2}\beta)\Gamma\right|^2 \tag{5.5b}$$

Here,

$$\phi_1 = \exp\left(\frac{j2\pi L n_1}{\lambda} - \alpha L\right)$$

$$\phi_2 = \exp\left(\frac{j2\pi L n_2}{\lambda} - \alpha L\right)$$

$$\alpha = \frac{j\kappa\tau\bar{C}}{1-\tau^2\phi_2}$$

$$\beta = \frac{\bar{C}\sqrt{\phi_1}(j\kappa)^2}{1-\tau^2\phi_1}$$

$$\Gamma = \frac{\tau j\kappa\sqrt{\phi_1} + \sqrt{\phi_2}\bar{C}(j\kappa)^2\alpha}{1-\tau^2\phi_1 - \sqrt{\phi_2}\bar{C}(j\kappa)^2\beta}$$

$\bar{C}$ represents the attenuation experienced by the optical signal when it passes through the straight waveguides which connects the DRR. Using appropriate optical amplifiers in the bus waveguides helps to reduce the $\bar{C}$ effect on the output intensity. The refractive indicies of Ring1 and Ring2 (refer Figure 4.2) is represented as n_1 and n_2, which depends on the applied bias over the rings. The refractive indicies remains as n_{eff} at an applied bias of 0V on the ring while an applied non-zero bias results in a refractive index value of $n_{1,2} = n_{eff} - \Delta n$.

5.2.4 Realization of carrier injective off axis MRR based logic gate

Off axis MRR is an attractive MRR configuration with non-concentric rings. The inner off axis rings has the potential to generate extra resonant notches in the output spectrum due to extra phase matching condition occuring between inner and outer rings. In our analysis we are considering the configuration with a single inner off axis ring and and outer ring based MRR. The configuration contributes smaller device size compared to parallel and series MRR configurations, thus leads to better footprint management in interconnect architecture.

τ_1 and κ_1 represents the transmission and coupling coefficient between the bus waveguide and outer ring while τ_2 and κ_2 represents the transmission and coupling coefficient between the non-concentric inner and outer rings as shown in Figure 5.2. The coupling between the rings will be less than the coupling between bus-ring waveguide due to reduced coupling region between ring-ring waveguides. C_1 and C_2 represents the phase change in

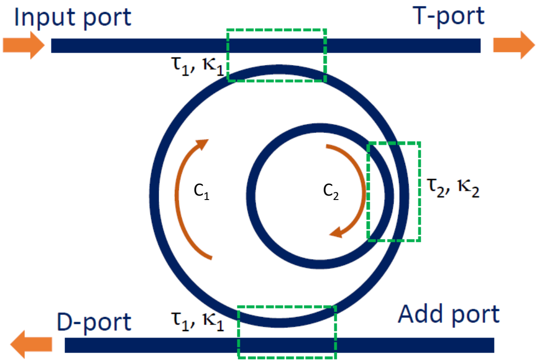

Figure 5.2: Off axis MRR configuration with a single inner and outer ring.

outer ring and inner ring respectively while propagation of light through it. The normalized transfer functions of the proposed off axis MRR configuration to obtain the normalized output port intensities at T port (P_T) and D port (P_D) are expressed as:

$$P_T = \left|\tau_1 + j\kappa_1 M_1\right|^2 \tag{5.7a}$$

$$P_D = \left|M_2 + M_3\right|^2 \tag{5.7b}$$

Here,

$$M_1 = \frac{C_3^2\tau_1\tau_2\sqrt{C_1}j\kappa_1 - C_3^2\tau_1\tau_2^2\sqrt{C_1}\sqrt{C_2}j\kappa_1 + j\kappa_1 j\kappa_2^2 C_3^2\sqrt{C_1}\sqrt{C_2}\tau_1}{1 - \tau_2\sqrt{C_2} - \sqrt{C_1}\tau_1^2 C_3^2\tau_2 + \sqrt{C_1}\sqrt{C_2}\tau_1^2\tau_2^2 C_3^2 - j\kappa_2^2 C_3^2\tau_1^2\sqrt{C_1}\sqrt{C_2}}$$

$$M_2 = C_3^2\tau_1\tau_2 j\kappa_1 + \frac{j\kappa_1 j\kappa_2^2 C_3^2\sqrt{C_2}\tau_1}{1 - \tau_2\sqrt{C_2}}$$

$$M_3 = C_3^2\tau_2 j\kappa_1^2 + \frac{j\kappa_1^2 j\kappa_2^2 C_3^2\sqrt{C_2}}{1 - \tau_2\sqrt{C_2}}$$

$$C_1 = \exp\left(\frac{j2\pi L_1 n_1}{\lambda} - \alpha L_1\right)$$

$$C_2 = \exp\left(\frac{j2\pi L_2 n_2}{\lambda} - \alpha L_2\right)$$

$$C_3 = \sqrt{\sqrt{C_1}}$$

L_1 and L_2 represents the circumference of outer and inner rings while n_1 and n_2 represents the applied voltage dependent refractive index of inner and outer ring. Here, L_1=$2\pi R_1$ and L_2=$2\pi R_1$ where R_1 and R_2 are the radius of outer ring and off axis ring. It is observed that the off axis MRR configuration act as inhibitor logic gate when the radius of outer ring is selected as double of inner ring. An inhibitor logic gate is a universal logic gate which are mainly popular in enzymic activity in biochemical reactions. In an inhibitor logic gate, the presence of one input inhibits or inactivates the other input. Inhibitor logic gate are mainly of four forms, two types of NOT+AND inhibitor gate and two types of NOT+OR inhibitor gate as shown in Figure 5.3 with a and b represents the operands to the gates.

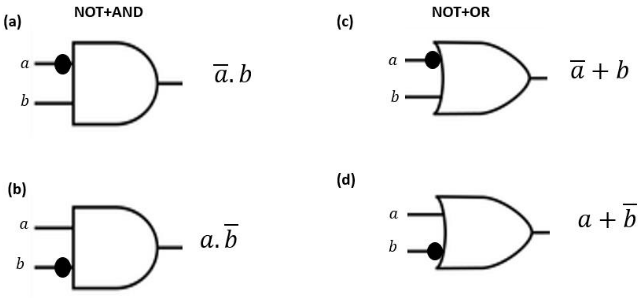

Figure 5.3: Types of inhibitor gates.

The off axis MRR configuration can successfully realize NOT+AND and NOT+OR inhibitor logic gatse (Figure 5.3(a) and (d)) and the truth table of the respective inhibitor gates are shown in Table 5.1. The presence of one input inactivates the action of other input. The operation of the device as a logic gate is described below. Here, we considered that the zero bias applied on the rings leads to resonant condition while an applied bias on the rings leads to non-resonant condition. Input1 and input2 represent the bias applied on outer ring and off axis ring respectively. The launched wavelength which satisfies resonant condition in the MRRs is λ_R.

Case 1: (Input1=0, Input2=0, $\lambda = \lambda_R$): A zero bias applied to outer ring and off axis ring results in resonance conditions at the MRRs for optical signals of wavelength λ_R launched into the input port. This scenario results in high optical intensities (logic 1) at the T port and low intensities (logic 0) at D port.

Case 2: (Input1=0, Input2=1, $\lambda = \lambda_R$): A zero bias applied to outer ring and a non-zero bias is applied to off axis ring results in resonance conditions at the outer ring while non-resonant condition at off axis ring for optical signals of wavelength λ_R launched into the input port. This scenario results in low optical intensities (logic 0) at the T port and high intensities at the D port.

Case 3: (Input1=1, Input2=0, $\lambda = \lambda_R$): A zero bias applied to off axis ring and a non-zero bias is applied to outer ring results in resonance conditions at the off axis ring while non-resonant condition at outer ring for optical signals of wavelength λ_R launched into the input port. This scenario results in low optical intensities (logic 0) at the D port and high intensities (logic 1) at T port.

Case 4: (Input1=1, Input2=1, $\lambda = \lambda_R$): A non-zero bias is applied to outer ring and off axis ring results in resonance conditions at the off axis ring while non-resonant condition at outer ring for optical signals of wavelength λ_R launched into the input port. This scenario results in low optical intensities (logic 0) at the D port and high intensities (logic 1) at T port.

The output intensities at D port and T port of off axis MRR configurations at different bias conditions act as the output of inhibitor gates (NOT+AND ($\bar{a}b$) and NOT+OR ($a + \bar{b}$) respectively) with applied bias as operands. The truth table of inhibitor gates is shown in Table 5.1.

Table 5.1: Truth table for NOT+AND inhibitor gate ($\bar{a}b$) and NOT+OR inhibitor gate ($a + \bar{b}$).

Input1 (a)	Input2 (b)	NOT+AND ($\bar{a}b$)	NOT+OR ($a + \bar{b}$)
0	0	0	1
0	1	1	0
1	0	0	1
1	1	0	1

5.3 Results and Discussions

Based on the principle of the proposed triple parallel MRR configuration for operation as OR/AND and NAND/NOR logic gates, shown in Figure 4.2 and as discussed in the previous section, the logical outputs are collected at the T port and D port of MRR3, while the input continuous-wave resonant (at zero or non-zero bias) wavelength signals are launched at input port of MRR1 and add port of MRR2. The average carrier density injected into the i-GaAs region during forward biasing is calculated by solving the electron and hole transport equations [**?**]. The induced carrier density leads to resonant wavelength shift (due to a change in the refractive index), which results in changes in the intensities of the optical signals at the output ports. The light intensity change at the D and T port is decided by the change in the refractive index which in turn depends on the applied bias and therefore on injected carrier density in the intrinsic region of the p-i-n diode. The available carrier density is also decided by the carrier life time and the active volume availabe for the carriers to recombine. A smaller life time leads to smaller carrier concentration as the rate at which carriers recombine would be fast. Similarly, a larger active volume would also result in smaller carrier concentration as the carrier recombination would be large [**?**]. The coupling coefficient variation affects the output port intensities [**?**] in the proposed MRR logic gate configurations and the optimum coupling coefficient to attain maximum CRs at output ports depends upon the refractive index change in the rings resulting from the applied bias. The optimization of the proposed logic gate configuration is therefore achieved by optimizing the width (w) of the i-GaAs region, the applied bias, the lifetime of carriers in the i-GaAs region and the coupling coefficients of the ring-bus waveguides for maximizing contrast ratio and optical field confinement in the light carrying core region of the proposed logic-gate configuration. As confinement increases, the cladding losses decreases and leads to appearance of higher fraction of intensities at the output ports. Thus helps to achieve better contrast ratio between the output port intensities representing the logic 0 and logic 1 conditions in MRR logic gate.

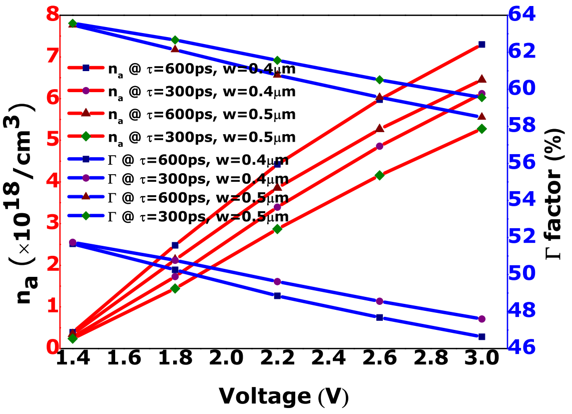

Figure 5.4: Dependency of average concentration and confinement factor on applied bias, intrinsic width and lifetime in i-GaAs.

The absorption and refractive index change are estimated by considering the contribution of the BF, BGS and FCA effects (Eq. (5.1) and (5.2)) as described in section 5.2.1. Increasing the width of the i-GaAs region enables better optical signal confinement, however, the average carrier concentration injected into the core region during forward biasing gets reduced, due to the increase in electron-hole recombination rate. Note that, increasing the applied bias increases the average concentration in the core region, however, also increases the current and therefore the power dissipation. A larger bias also results in reduced optical signal confinement in the intrinsic GaAs region, since the refractive index difference between i-GaAs core and AlGaAs cladding reduces. All these effects constrains the range of the applied bias to 1.4V-3.0V and intrinsic region width of 0.4-0.5μm.

The microrings in the proposed configuration are assumed to be identical of radius 5μm. The launched resonant wavelength at zero bias is selected to be 1559.7nm, a wavelength that falls in the window where the fiber attenuation is minimal. The dependency of n_a on the width of the intrinsic region, the carrier lifetime and the applied bias is depicted in Figure 5.4, and the corresponding Δn and $\Delta\alpha$ is calculated by referring Eqs (1) and (2). It is obvious from Figure 5.4 that the average carrier concentration increases with increasing both the bias voltage and the carrier lifetime, whereas increasing the width of intrinsic region reduces the carrier concentration. An increase in lifetime results in higher n_a (leading to higher refractive index change) with respect to increase in voltage, however, this may not be always favorable for attaining higher CR at the output ports, because a higher refractive index change could now cause the signal to be resonant at both zero and non-zero biased condition. In addition, the optical confinement increases when the intrinsic region width increases, however, it decreases with increasing the applied bias. This is because, at higher bias, a larger average carrier density is present in the core region, which greatly reduces the refractive index of the core, thereby reducing the refractive index difference between the core and the cladding, and thereby reducing the optical mode confinement. Figure 4 shows $\Delta\alpha_{BF+BGS}$ and Δn_{total} versus wavelength for an intrinsic region width of 0.4μm and τ =300ps and different bias voltages applied to the ring configuration. The change in absorption and refractive index increases with increasing the applied bias voltage. FCA typically contributes to the change in refractive index at higher wavelengths. As shown in Figure 5.5(b), at 1559.7nm, a refractive index change of 0.0266 is attained when the bias changes from 1.4V to 3.0V.

5.3.1 CI based triple parallel MRR logic gate outputs

The modified output intensities at the MRR output ports can be obtained by substituting Δn in the transfer functions of proposed triple parallel MRR logic gate configuration (Eq. 4). The bias voltage applied to Ring3 is assumed to be the same bias applied on Ring1. Figure 5.6(a) and Figure 5.6(b) show the normalized output optical intensity at the T port

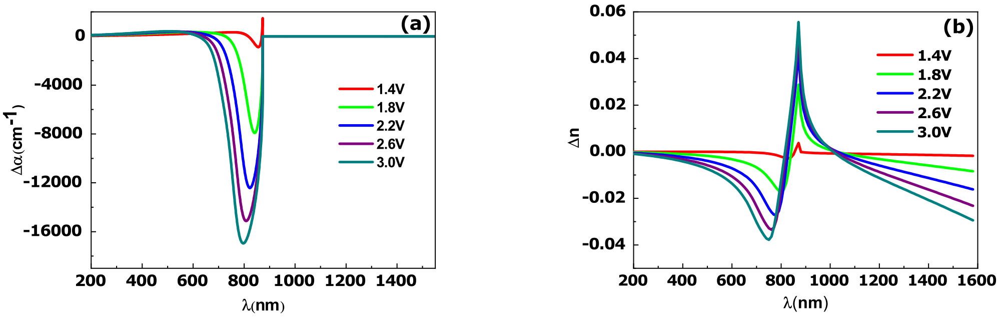

Figure 5.5: (a)BF and BGS effect based absorption change spectrum for a w=0.4μm and τ=300ps at different applied bias. (b) Total refractive index change ($\Delta n_{BF+BGS+FCA}$) as a function of wavelength for a w=0.4μm and τ=300ps at different applied bias.

and D port of MRR3, versus wavelength at different bias voltages applied to MRRs 1 and 2, when the proposed configuration is operated as an OR/NAND gate and AND/NOR gate, respectively. As shown in Figure 5.6(a), for λ=1559.7nm and κ=0.55, a high output optical signal intensity (logic 1) is obtained at the T port of MRR3, when either Ring1 or Ring2 are biased, leading to OR gate realization. For λ=1549.6nm and κ=0.55, a low output optical signal intensity (logic 0) is obtained at the T port of MRR3, only when both Ring1 and Ring2 are biased at 2.6V, leading to NAND gate realization. Referring to Figure 5.6(b), for λ=1559.7nm and κ=0.55, the D port of MRR3 collects a high-intensity optical signal only when both rings are biased, thus realizing an AND gate. For λ=1549.6nm and κ=0.55, the D port of MRR3 collects a high-intensity optical signal only when both the rings are not biased at 2.6V, thus realizing a NOR gate. The truth table for the proposed carrier injection based OR/AND triple MRR logic gate configuration is depicted in Table 5.2 which demonstrates the OR and AND logic operations. The threshold value is chosen as 0.3 times the input light intensity. Hence, if output intensity is above 0.3 times the input intensity it will be considered as logic 1, otherwise it is considered as logic 0.

CR is defined as the intensity difference between the high and low states in the gate. Therefore, CR1, CR2 and CR3 for the OR gate are the intensity difference between the outputs for (Input1, Input2)=(1, 1) and (Input1, Input2)=(0, 0), (Input1, Input2)=(1, 1) and (Input1, Input2)=(0, 1), (Input1, Input2)=(1, 1) and (Input1, Input2)=(1, 0), respectively. Note that the coupling coefficient between the ring and bus waveguides needs to be optimized in order to obtain a high CR for given intrinsic region width, applied bias voltage and relaxation time. Figures 5.7(a-d) show the normalized output optical intensities at the T port (OR gate) of MRR3 versus the coupling coefficient for different CR values and for a

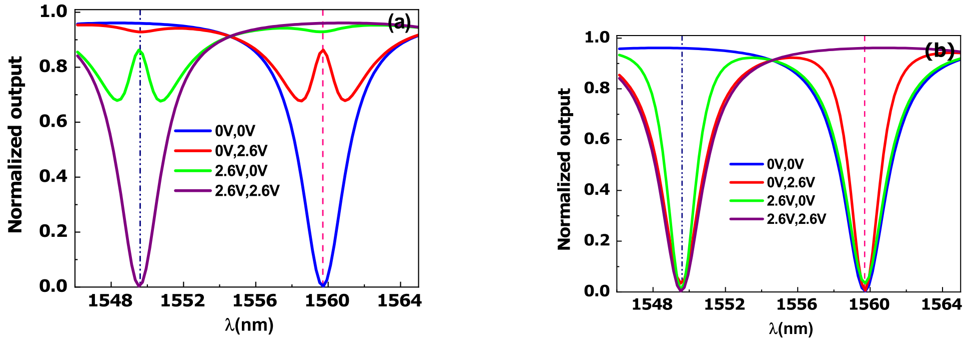

Figure 5.6: (a) Normalized T port intensity spectrum with OR gate realized at 1559.7nm (vertical pink dashed line) and NAND gate realized at 1549.6nm (vertical blue dot dashed line). (b) Normalized D port intensity spectrum with AND gate realized at 1559.7nm (vertical pink dashed line) and NOR gate realized at 1549.6nm (vertical blue dot dashed line). Logic 1 operand is represented as 2.6V on the p-i-n structured MRR while 0V represents logic 0 operand condition.

launched wavelength of 1559.7nm, τ=300ps, w=0.4μm for different logic 1 bias conditions of V=1.4V, 1.8V, 2.2V and 2.6V, respectively.

Table 5.2: Truth table for OR and AND gate at applied bias as 0V and 2.6V and κ=0.55, λ=1559.7nm, w=0.4μm and τ=300ps. The value in the square brackets represent the optical power at the respective ports.

Input1 (Ring1)	Input2 (Ring2)	OR (T port)	AND (D port)
0 (0 V)	0 (0 V)	0 [0.0025]	0 [0.0025]
0 (0 V)	1 (2.6 V)	1 [0.8631]	0 [0.0052]
1 (2.6 V)	0 (0 V)	1 [0.9292]	0 [0.0339]
1 (2.6 V)	1 (2.6 V)	1 [0.9603]	1 [0.9603]

As shown in Figure 5.7, the optimum coupling coefficient required to maximize the CRs for the OR gate at the T port depends on the applied bias voltage (representing logic 1 condition). The maximum CR attained for the OR gate is at an applied bias voltage of 2.6V when κ=0.586. Figures 5.8(a-d) show the normalized output optical signal intensities at the D port (AND gate) of MRR3 versus coupling coefficient for different CR values and for a launched wavelength of 1559.7nm, τ=300ps, w=0.4μm, for different logic 1 bias conditions of V=1.4V, 1.8V, 2.2V and 2.6V, respectively. As shown in Figure 5.8, the optimum coupling coefficient required to maximize the CRs for the AND gate at the D port depends

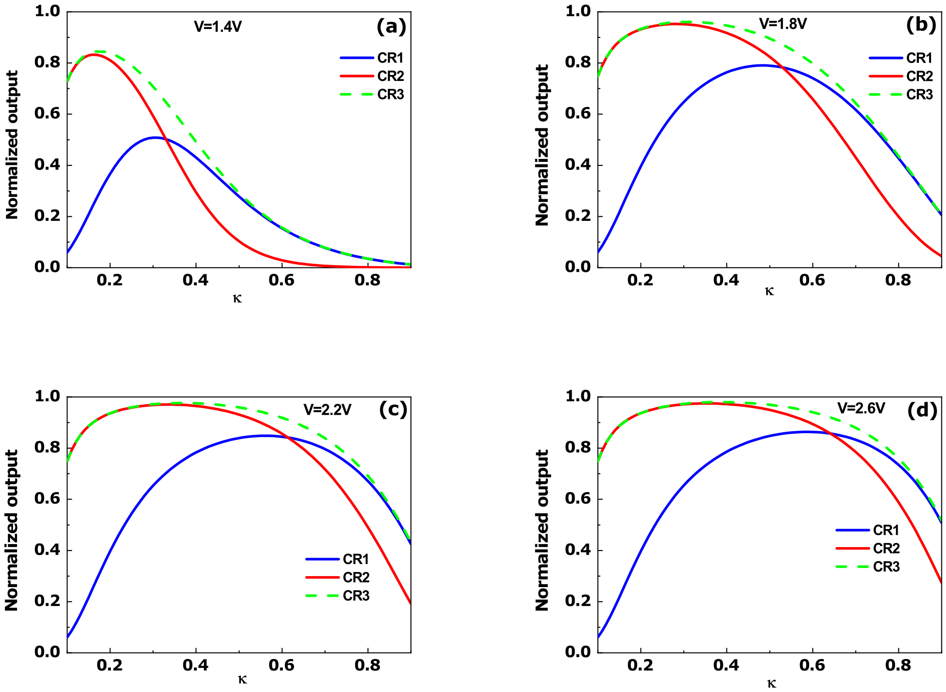

Figure 5.7: T port CR dependency on coupling coefficient of triple CI MRR based OR gate with Ring3 fed with Input1 with an applied bias of (a) 1.4V (b) 1.8V (c) 2.2V (d) 2.6V as input logic 1 condition and operating wavelength λ_R=1559.7nm

on the applied bias voltage (representing logic 1 condition). For an applied bias voltage of 2.6V when κ=0.431, a maximum CR is attained for AND gate for an intrisic width of 0.4μm and operating wavelength as λ_R=1559.7nm. The maximum CRs (CR1, CR2 and CR3) attained at an applied bias of 1.4V is less compared to the maximum CRs obtained at an applied bias of 2.6V with the optimized coupling coefficient values. Typically, the optimum κ for maximizing the CR depends on applied bias voltage, intrinsic region width and carrier recombination lifetime. It is noteworthy that the CR attained at the optimum coupling coefficient increases with the applied bias voltage. From figures 5.7 and 5.8, it is interesting to note that for the designed logic OR and AND gate configurations, the tolerance of the output intensity to the variation in κ increases as the applied bias increases. The intensity-versus-κ curves at higher bias volatges has almost a constant value, enabling the selection of a single optimum coupling coefficient (instead of two different optimum coupling coefficients) for both the OR and AND gate. The "flat-top" nature of intensity-versus-κ during higher applied bias results from the large change in the refractive index due to which the wavelength that would have been resonant with the ring under applied bias shifts far away from the wavelength that was resonant to the ring with no applied bias.

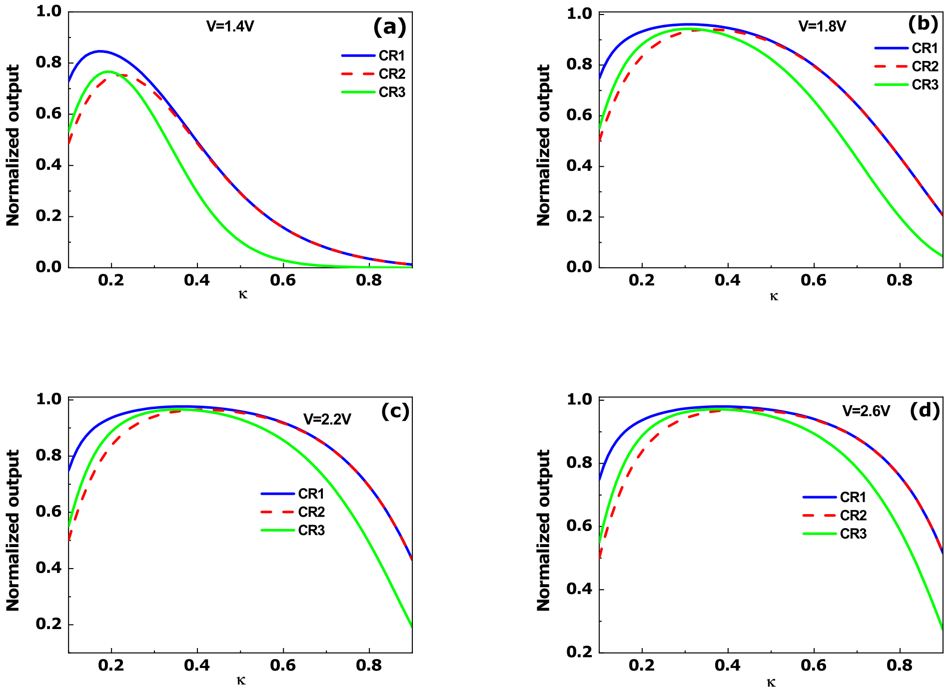

Figure 5.8: D port CR dependency on coupling coefficient for triple CI MRR based AND gate with Ring3 fed with Input1 with an applied bias of (a) 1.4V (b) 1.8V (c) 2.2V (d) 2.6V as logic 1 condition and operating wavelength λ_R=1559.7nm

Imperfections that occur during the fabrication of MRR can cause deviations in the gap between ring and bus waveguides, resulting in significant difference in κ value obtained and κ value designed. This, however, will not be a major issue in the proposed MRR OR/AND logic gate configuration when operated at higher bias due to an almost constant appreciable CRs attained over a wider range of κ values. Also, the flat-topped intensity-versus-κ curves at higher bias voltages facilitate to design the MRRs at relatively smaller κ values instead of higher κ values, as higher κ values demand for smaller gap between ring and bus waveguides with advanced device fabrication process. This considerably relaxes the fabrication complexity. However, the fabrication tolerance admissible at higher bias will be at the expense of higher power dissipation, which should be minimized for logic gates. We have proposed a novel triple parallel MRR configuration for realizing OR and

AND gate or NAND and NOR gate at the output ports. In [57], the authors have reported XOR/XNOR and AND gate which are realized using Mach-Zehnder interferometer, which is bulky in nature and hence not suitable for large scale integration. In [56], the authors have reported AND/NAND and OR/NOR logic gates realized using MRR, however the switching is enabled using thermo-optic effect. This switching mechanism faces poor stability and reliability. Our proposed device on the other hand relies on carrier injection based switching mechanism which requires only a low operating voltage and making it more reliable, thermally stable and consumes only lesser footprint. Furthermore, the proposed triple parallel configuration provides better functionality as non-conjugate gates (OR and AND or NAND and NOR gates) are obtained simultaneously in the MRR output ports instead of obtaining conjugate gates (like AND and NAND gates, OR and NOR gates) simultaneously at the output ports as in conventional configurations introduced in the literature. CI based triple parallel MRR logic gate realizes NAND and NOR gate at the output port, which is not possible to realize in electroabsorption based triple parallel MRR due to higher absorption effect as the operating wavelength is needed to be selected near bandgap edge of the core material.

Table 5.3: Truth table for NAND and NOR gate at applied bias as 0V and 2.6V, κ=0.55 for NAND gate and κ=0.44 for NOR gate, λ=1549.6nm, w=0.4μm and τ=300ps. The value in the square brackets represent the optical power at the respective ports.

Input1 (Ring1)	Input2 (Ring2)	NAND (T port)	NOR (D port)
0 (0 V)	0 (0 V)	1 [0.9573]	1 [0.9825]
0 (0 V)	1 (2.6 V)	1 [0.9237]	0 [0.0217]
1 (2.6 V)	0 (0 V)	1 [0.8631]	0 [0.0168]
1 (2.6 V)	1 (2.6 V)	0 [0.0032]	0 [0.0078]

The same triple parallel MRR logic gate configuration with CI modulation mechanism can also work as NAND and NOR gates using the T port and D port of MRR3, when the launched wavelength satisfies resonance condition at an applied bias voltage for the MRRs. Each MRR satisfies the resonance condition at an operating wavelength, λ= 1549.6nm, with an applied bias of 2.6V, leading to the realization of NAND and NOR gates using the T port and D port (refer Figure 5.6(a) and (b)). Note that, a change in absorption of the rings through electroabsorption mechanism can also result in a change in the refractive index of the rings and can be used to realize logic gates using MRR configurations. However, in realization of logic gates using electroabsorption [58], it was observed that the electroabsorption-based modulation mechanism fails to realize NAND/NOR gates us-

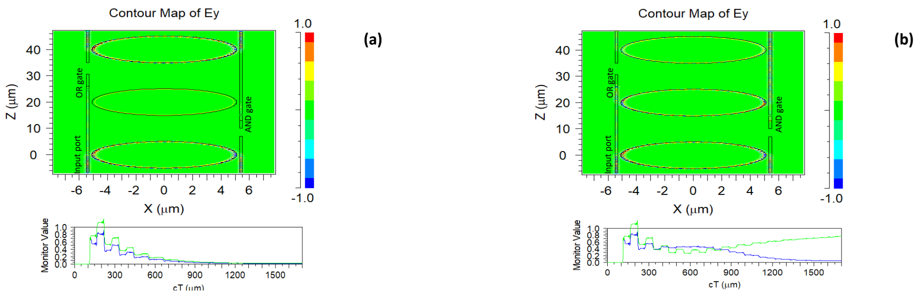

(a) Input1=0,Input2=0 (b) Input1=0,Input2=1

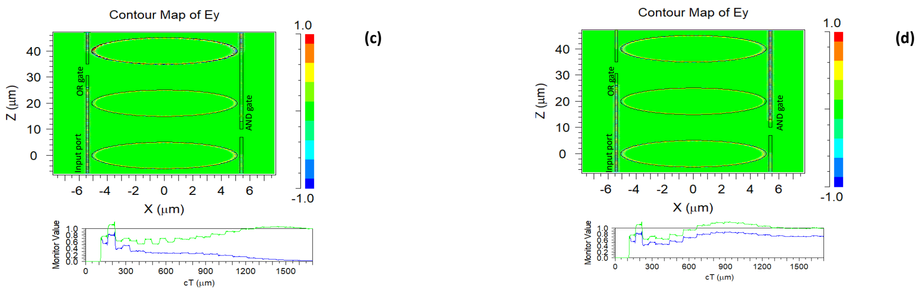

(c) Input1=1,Input2=0 (d) Input1=1,Input2=1

Figure 5.9: Rsoft parallel triple MRR OR and AND outputs with Input1, Input2 as field applied on Ring1 and Ring2, OR output (green line) at T port and AND port blue line) at D port. (a) Input1=0,Input2=0 (b) Input1=0,Input2=1, (c) Input1=1,Input2=0 (d) Input1=1,Input2=1.

ing triple parallel MRR configuration. This is because, at an applied bias, absorption of the rings increase due to the reduction of the Q factor during the propagation of resonant wavelength through the rings when a non-zero bias voltage is applied to the rings. On the other hand, usage of CI mechanism in triple parallel MRR configuration successfully overcomes this drawback and helps in realizing both OR and AND or NAND and NOR logic gates at the output ports, thus making the proposed device more versatile. The coupling dependency to yield maximum CR in NAND/NOR gate is similar to the calculated optimum κ for the OR/AND gate configuration. The truth table for the NAND/NOR gate for the launched wavelength λ= 1549.6nm and at their optimized coupling condition is shown in Table 2 for an applied bias voltage of 2.6V (logic 1 operand condition), and demonstrates the NAND and NOR logic operations.

The proposed triple parallel MRR configuration (refer Figure 5.1) to realize OR and AND gates can be modified by avoiding the two bus waveguides, through which the input wavelengths are not launched (refer Figure 5.10). But comparing to the earlier proposed configuration with four bus waveguides, the CR attained between the logic high and low

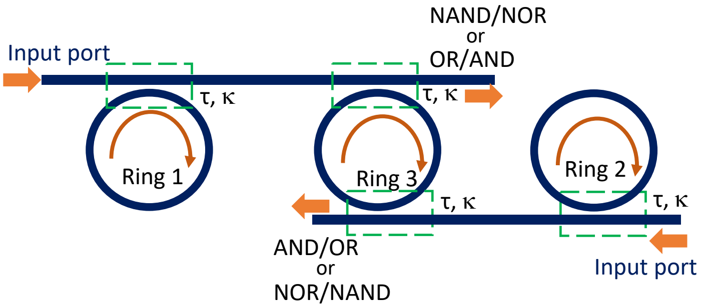

Figure 5.10: Modified triple parallel MRR logic gate (OR/NOR/AND/NAND) configuration with two bus waveguides.

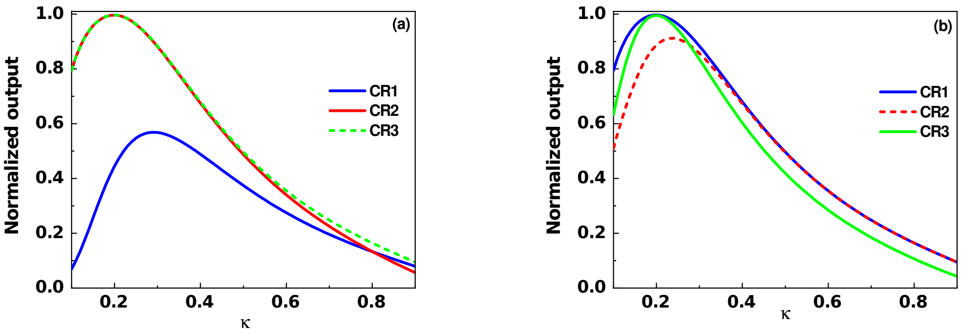

Figure 5.11: CR dependency on coupling coefficient for modified triple CI MRR based OR and AND gate with Ring3 fed with Input1 with an applied bias of 2.6V on rings as logic 1 operand at 1549.6nm (a) at T port (b) at D port.

states of the OR gate in the modified structure is less (with the bias applied on Ring3 is same as Ring1). The Figure 5.11 depicts the CR of OR and AND gate outputs obtained for the modified CI triple parallel MRR configuration with λ=1559.7nm at an applied bias of 0V and 2.4V for representing logic 0 and logic 1 operands. The CRs (CR1,CR2 and CR3) for OR and AND gates at T port and D port are mentioned earlier.

Tolerance level for κ in Figure 5.11 is less compared to Figure 5.7(c) and Figure 5.7(d). The absence of drop ports and add ports in the configuration limits further signal processing of the launched wavelengths at resonant condition and addition of signals into the configuration. The advantage of the modified MRR logic gate configuration is that the optimum coupling required to attain high CR is small compared to the earlier configuration, which helps in fabrication by increasing the gap between ring and bus waveguide.

5.3.2 Parallel CI DRR logic gate outputs

As discussed in section 5.2.3, parallel DRR configurations can act as AND and NAND or NOR and OR logic gates by CI modulation mechanism. The truth table for AND and NAND gates at T port and D port at λ=1559.7nm, κ=0.5, w=0.4μm and τ=300ps is depicted in Table 5.4. At an operating wavelength λ=1549.6nm (satisfies resonant condition at applied bias of 2.6V), the T port and D ports of the MRR configuration act as NOR and OR gates respectively. The corresponding truth table is shown in Table 5.5 at κ=0.5, w=0.4μm and τ=300ps. Figure 5.12 (a) and (b) represents the output spectral response of CI based parallel DRR at T port and D port respectively at an applied bias of 2.6V on p-i-n heterostructured MRR for representing logic 1 operand.

Table 5.4: Truth table for AND and NAND gate at applied bias as 0V and 2.6V and κ=0.5, λ=1559.7nm, w=0.4μm and τ=300ps. The value in the square brackets represent the optical power at the respective ports.

Input1 (Ring1)	Input2 (Ring2)	AND (T port)	NAND (D port)
0 (0 V)	0 (0 V)	0 [0.0011]	1 [0.9314]
0 (0 V)	1 (2.6 V)	0 [0.0041]	1 [0.8717]
1 (2.6 V)	0 (0 V)	0 [0.0041]	1 [0.8717]
1 (2.6 V)	1 (2.6 V)	1 [0.9415]	0 [0.0797]

Table 5.5: Truth table for NOR and OR gate at applied bias as 0V and 2.6V and κ=0.5, λ=1549.6nm, w=0.4μm and τ=300ps. The value in the square brackets represent the optical power at the respective ports.

Input1 (Ring1)	Input2 (Ring2)	NOR (T port)	OR (D port)
0 (0 V)	0 (0 V)	1 [0.9139]	0 [0.0802]
0 (0 V)	1 (2.6 V)	0 [0.0057]	0 [0.8693]
1 (2.6 V)	0 (0 V)	0 [0.0057]	0 [0.8693]
1 (2.6 V)	1 (2.6 V)	0 [0.0015]	1 [0.9310]

5.3.3 CI based off axis MRR inhibitor gate outputs

The wavelength dependency of output intensities at T port and D port of off axis MRR configuration is shown in Figure 5.13. It is observed that at zero bias resonant wavelength (1559.7nm), the configuration act as inhibitor gates at T port and D port. The T port output

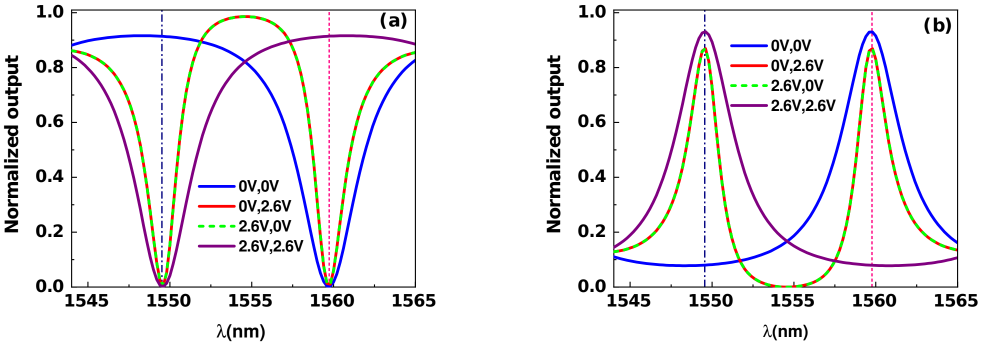

Figure 5.12: (a) Normalized T port intensity spectrum with AND gate realized at 1559.7nm (vertical pink dashed line) and NOR gate realized at 1549.6nm (vertical blue dot dashed line). (b) Normalized D port intensity spectrum with NAND gate realized at 1559.7nm (vertical pink dashed line) and OR gate realized at 1549.6nm (vertical blue dot dashed line). Logic 1 operand is represented as 2.6V on the p-i-n structured MRR while 0V represents logic 0 operand condition.

intensity yields low intensities only at zero bias applied on outer ring and non-zero bias applied on off axis ring. The Figure 5.13 is plotted at ring-bus coupling (κ_1) as 0.6 and ring-ring coupling as (κ_2) as 0.45. Due to smaller interaction length between ring-ring waveguides, the coupling between ring-ring waveguides at a particular gap is less than the coupling between ring-slab waveguides.

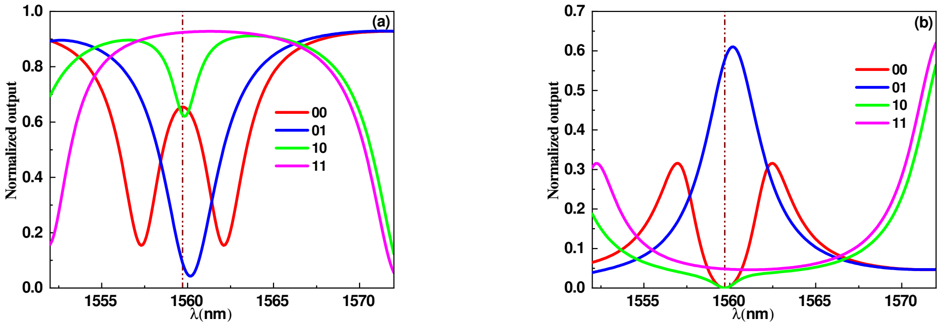

Figure 5.13: (a) Normalized T port intensity spectrum at 1559.7nm inhibitor logic gate-NOT+OR with applied bias as 2.6V. (b) Normalized D port intensity spectrum at 1559.7nm (inhibitor logic gate-NOT+AND) with applied bias as 2.6V (logic 1).

The radius of the rings are selected in such a way that both the MRRs satisfy resonant condition at zero bias. The radii are R$_1$=5μm and R$_2$=2.5μm. The output port intensities also depends on the coupling between ring-ring and ring-bus waveguides. Proper optimization of coupling coefficient will only leads to the realization of inhibitor gates at the output ports of the proposed off axis configuration.

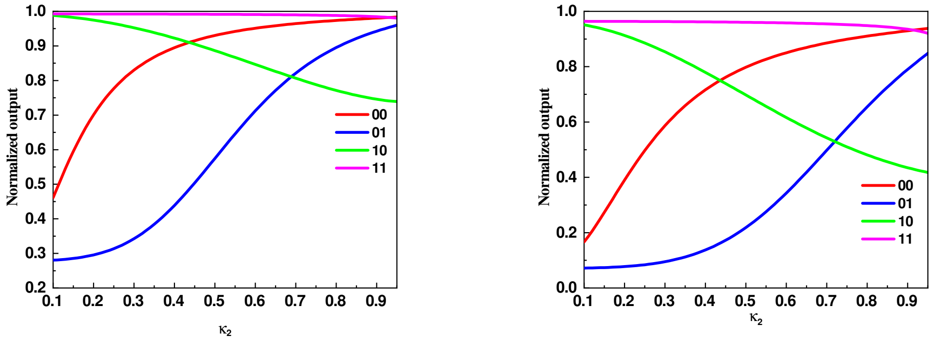

(a) κ_1=0.3 (b) κ_1=0.5

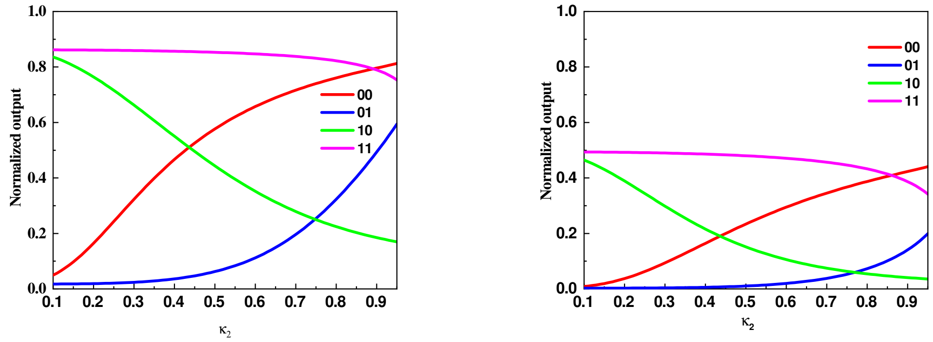

(c) κ_1=0.7 (d) κ_1=0.9

Figure 5.14: Normalized T port intensity for an operating wavelength 1559.7nm at different coupling values at main ring (κ_1) and off axis ring (κ_2) for ring1 radius as 5μm and ring2 radius as 2.5μm.

The dependency of coupling coefficents on the normalized output port intensities at an operating wavelength 1559.7nm is shown in Figure 5.14 and Figure 5.15 respectively. As there are two set of coupling coefficients (coupling between ring-bus waveguides (κ_1)) and coupling between ring-ring waveguides (κ_1)), we need to optimize both the coupling values to attain maximum contrast ratio in the inhibitor gate output. The coupling dependency graphs in Figure 5.14 and Figure 5.15 are plotted by keeping κ_1 fixed in each plot and κ_2 is varied. From the optimization procedure, it is observed that maximum contrast ratio obtained at T port to realize NOT+AND inhibitorlogic gate is at κ_1=0.65 and κ_2=0.4

while maximum contrast ratio obtained at D port to realize NOT+OR inhibitor logic gate is at κ_1=0.6 and κ_2=0.45. The truth table for NOT+AND and NOT+OR inhibitor gate obtained at T port and D port of off axis MRR configuration are shown in Table 5.6 with corresponding intensities at optimized coupling values.

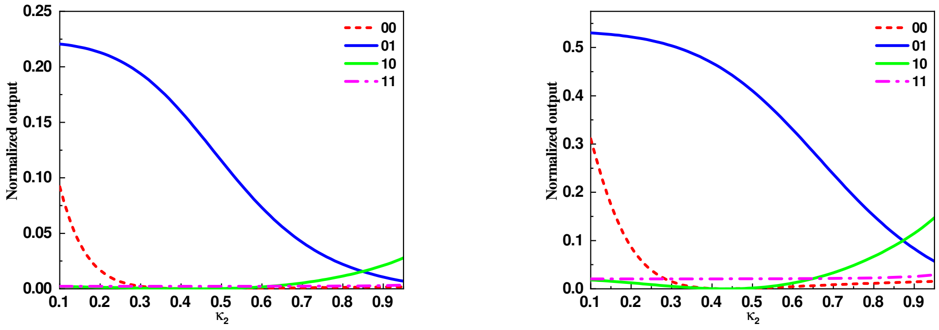

(a) κ_1=0.3

(b) κ_1=0.5

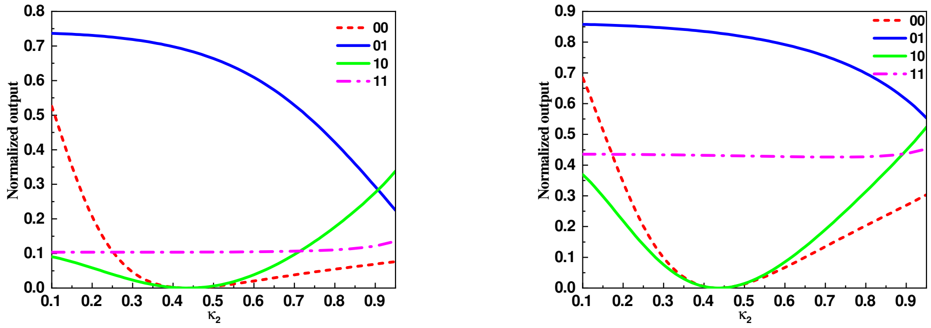

(c) κ_1=0.7

(d) κ_1=0.9

Figure 5.15: Normalized T port intensity for an operating wavelength 1559.7nm at different coupling values at outer ring (κ_1) and off axis ring (κ_2) for ring1 radius as 5μm and ring2 radius as 2.5μm.

Table 5.6: Truth table for the NOT+OR (T port) and NOT+AND (D port) gates at an applied bias of 2.6V with κ_1 and κ_2 as the coupling values between outer ring-bus waveguides and off axis ring-outer ring respectively. The value in the square brackets represent the optical power at the respective ports.

Input1 (outer ring)	Input2 (inner ring)	κ_1=0.65,κ_2=0.4		κ_1=0.6,κ_2=0.45	
		T port	D port	T port	D port
0 (0V)	0 (0V)	1 [0.5347]	0 [0.0015]	1 [0.6545]	0 [0.0001]
0 (0V)	1 (2.6V)	0 [0.0515]	1 [0.6509]	0 [0.0925]	1 [0.5765]
1 (2.6V)	0 (0V)	1 [0.6166]	0 [0.0013]	1 [0.6265]	0 [0.0001]
1 (2.6V)	1 (2.6V)	1 [0.8961]	0 [0.0712]	1 [0.9239]	0 [0.0482]

The proposed triple parallel MRR configuration using carrier injection modulation can successfully realize OR and AND gates simultaneously at the T port and D port when the MRR satisfies resonant condition at zero field applied on the rings. It can also successfully realize NOR and NAND gates simultaneously at the D port and T port when the MRR satisfies resonant condition at non-zero field applied on the rings. This proposed configuration realize AND and OR gates simultaneously, instead of complementary logic gates (providing inverted and non-inverted logic output) attaining at the T port and D port which is highly useful in interconnect architecture demanding smaller footprint and high density packaging.

Designing the logic gates using MRR helps to design with smaller footprint compared to logic gates designed using Mach Zehnder Interferometer [57]. The ring size can be limited to 10μm scale while a MZI with acceptable ON OFF intensity contrast requires a size on cm range ($10^4\mu m$) [57].

In reference[**?**], six MRRs layout is used to design OR and NOR gate based on non-linear effect. The proposed parallel double ring MRR based on carrier injection modulation requires only two MRRs for realizing OR and NOR gates. Also the proposed triple parallel MRRs based on carrier injection modulation mechanism only uses 3 MRRs to realize OR gate and NOR gate.

5.4 Conclusion

A novel logic gate configuration based on the use of triple parallel MRRs in conjunction with carrier injection is proposed. Results shows that by using the bias voltage applied to MRRs as the operands and the output intensities at the T port and D port as the logic gate outputs, the proposed logic gate configuration simultaneously realize OR and AND gate or NAND and NOR gate operations depending on the wavelength of the optical signal launched into the input port and add port of the logic gate configuration. The dependency of the contrast ratio of the logic gate outputs on the applied bias voltage, relaxation time, intrinsic region thickness and coupling coefficient between the ring and bus waveguide have been simulated, and the results have shown that, by increasing the bias voltage, a higher fabrication tolerance (high contrast ratio obtained over a wider value range of coupling coefficient) is achieved. The fabrication tolerance attained at higher applied bias enables the selection of a single optimum coupling coefficient (instead of two different optimum coupling coefficients) to simultaneously realize both the OR and AND gates or NAND and NOR gates. The failure in realization of NOR and OR gates based on parallel DRR configuration using EA modulation mechanism is resolved by using CI based MRRs in parallel DRR configuration. The inhibitor logic gates (NOT+AND and NOT+OR) can be successfully realized using off axis MRR configuration, which provides extra resonant notches along with smaller foot print. The off axis MRR configuration is optimized using the coupling between outer ring waveguide-off axis ring waveguide and outer ring waveguide-bus waveguide for better contrast ratio between the logic 0 and logic 1 intensities at the output ports inorder to realize inhibitor gates.

Chapter 7

Conclusions

Optical modulators are important functional block of optical interconnects in optoelectronic integrated circuits (OEICs). The bulkiness of conventional optical modulators is the major hindrance in the path of optical interconnects to attain high performance switches and signal processing units like optical logic gates. Microring resonators (MRRs) are the emerging solution to the performance crisis of optical interconnects by providing unique features like resonant nature, small footprint, narrow band filtering, high Q factor, compactness etc. MRRs are classified based on geometrical configurations and opted modulation mechanism for switching.

Modelling, performance analysis and optimization of MRR based optical modulators/switches and optical logic gates configurations is proposed and studied in this thesis. Electrical bias assisted change in absorption and refractive index experienced at the intrinsic layer of ring structure leads to the modulation in MRR. Electroabsorption and carrier injection modulation mechanisms are incorporated in the proposed p-i-n structured MRR modulators/logic gates to switch the light intensities between the output ports of MRR. A brief review about the theory, working principle and performance parameters of MRR along with its different applications are discussed. The studies in the thesis comprises of three domains. The first domain includes the optimization of electroabsorptive double ring MRR modulators to attain high contrast ratio and low insertion loss at low applied field. The realization and optimization of electroabsorption (EA) and carrier injection (CI) based MRR logic gates is another domain of studies. The transient performance analysis in carrier injection modulation based single ring MRR switch is also investigated.

The transfer functions of single ring add drop and double ring MRR configurations are derived and concluded that the refractive index, absorption in the ring, transmission and coupling coefficients between the waveguides are the output port intensity determining factors in MRR. The inverse dependency of coupling coefficients and gap between waveguides are analysed using couple mode theory. The advantage of vernier configuration to increase free spectral range without increasing bending loss in the ring is studied by deriving the transfer functions.

The performance of quantum confined stark effect based EA double ring MRR is optimized to obtain high contrast ratio and low insertion loss at low applied field, with the design optimizing parameters as quantum well (QW) width, QW material composition, radius of the ring, coupling between ring and bus waveguides, operating wavelength. The QWs incorporated in MRR experience change in absorption with respect to applied bias and the respective absorption is calculated by solving schrodinger wavefunction equation. The change in absorption leads to change in refractive index, which is calculated by applying Kramers kronig relation on the absorption change in QWs. The p-i-n structured MRRs are designed with i-InGaAsP acting as the core region for the launched light signal propagation and the light signal is confined in core region using the claddings made up of n-type and p-type InP. The spectral analysis performed at the output ports of MRR depicted the intensity variation at T port and D port according to applied field on the rings of the proposed double ring resonator (DRR). The studies revealed that even narrow QWs offers higher contrast ratio when incorporated in MRRs and optimized using operating wavelength and QW incorporated MRR parameters. It is observed that each QW DRR with fixed radius attains maximum contrast ratio (CR) at particular coupling coefficient. As the operating wavelength approaches the resonant wavelength of MRR configuration, the CR increases but the fabrication tolerance decreases.

Electro optic logic gates utilizes the benefits of both optics and electronics to simultaneously attain high speed operation and signal controlling convenience. Computational parallelism, high packaging densities and absence of gate delays leads to high performance directed MRR optical logic gates. Different optic logic gates such as buffer, NOT, Fredkin, AND, NAND, OR, XOR and XNOR gates are designed and realized using EA based MRR configurations. The realized hybrid architectured logic gates yields the ouptut of logic operation as the light intensities at the T port and D port of MRR while the operands of the logic operation is the applied field on the rings. The field applied on the rings varies absorption and associated refractive index change leads to the switching of output logic level. A novel EA triple ring MRR configuration is designed and realized to simultaneously yield OR and AND gates at the output ports. It is found that all the logic gates are realized under proper optimization of the configurations using operating wavelength, coupling coefficients and applied fields on the rings. The simulation results using RSoft FDTD supported the proposed configurations to operate as the respective logic gates. The failure of OR and NOR gate realization using EA parallel DRR is also analysed and found that the reduction of Q factor due to higher absorption at applied field leads to poor contrast ratio in the output ports.

CI based MRR logic gates attains more popularity due to polarization independency and the selection of operational wavelength is not limited to region near bandgap of the core material as in the case of EA based MRR logic gates. The contribution of bandfilling, bandgap shrinkage and free carrier absorption towards the refractive index change is studied and the respective spectral analysis is performed at the output ports in proposed MRR configurations with core as i-GaAs. The simulation results revealed the dependency of average carrier concentration on applied bias and width of intrinsic region in p-i-n structured MRR configuration. A novel triple parallel CI based MRR configuration is proposed and simultaneously realized OR and AND/ NAND and NOR gates at output ports depending on the resonant nature of launched wavelengths at input and add ports during zero and non-zero bias conditions (operands) on the rings. CI based parallel double ring MRR also succeeded to simultaneously realize AND and NAND/ NOR and OR gates at the output ports with applied bias on the rings acting as the operands. The behaviour of contrast ratios in the proposed logic gates are studied with respect to applied bias, width of intrinsic region and coupling between ring and bus waveguides. An off axis MRR configuration is proposed to realize the inhibitor logic gates (NOT+AND and NOT+OR) at the T port and D port. The configuration is properly optimized using the coupling between outer ring waveguide-off axis ring waveguide and outer ring waveguide-bus waveguide to obtain maximum contrast ratio at the logic gate outputs.

Carrier dynamics analysis conducted in CI based single ring MRR modulator by mathematical modelling revealed the frequency chirping and bit rate limitations for a launched WDM input at input port. Instantaneous response of the resonator along with the memory effect of earlier outputs are considered for deriving the time dependent transfer function at T port of MRR. Time domain response of i-GaAs MRR shows that certain non-resonant wavelengths present in WDM inputs can behave as resonant signal due to transient response of p-i-n heterostructure incorporated in the MRR for applying the bias. Proper selection of wavelengths for WDM inputs according to the nature of the ring helps to obtain chirp free outputs at the output port of MRR. The dependency of transmitted output on coupling coefficient and reverse current density is also studied for determining the switching transients of output along with memory effects.

EA and CI based MRR modulators are attractive choice to design high performance optical switches and logic gates in OEICs. The proposed configurations varies the output intensities by bias assisted absorption and refractive index change. The configurations successfully combines the benefits of resonant nature of MRR along with the EA and CI switching mechanisms.

Future scope

- Optimize the performance of EAM MRR optical switch with higher order of quantum wells in intrinsic region and higher order rings.
- Applying fields on the rings of MRR for EA and CI modulation mechanism based MRR optical switch and optical logic gates can result in slight variation in coupling coefficients between ring and us waveguides. Studies on stabilizing the coupling coefficients by applying field on bus waveguides of MRR.
- Designing and optimizing the performance of sequential logic gates using EA and CI based MRRs.
- Study the frequency chirping response of non-resonant wavelengths in EAM based MRR and to select the wavelengths effectively in WDM network containing MRR modulator.
- Study on the realization of the off axis MRR configuration based logic gates (various radius combinations of inner and outer rings).

Bibliography

[1] P. Kapur and K. C. Saraswat, “Optical interconnects for future high performance integrated circuits,” *Physica E: Low-dimensional Systems and Nanostructures*, vol. 16, no. 3, pp. 620 – 627, 2003.

[2] S. Navin and K. Banerjee, “Interconnect challenges for nanoscale electronic circuits,” *Journal of the Minerals, Metals and Materials Society*, vol. 56, pp. 30–31, 2004.

[3] W. Arden, “The international technology roadmap for semiconductors—perspectives and challenges for the next 15 years,” *Current Opinion in Solid State and Materials Science*, vol. 6, no. 5, pp. 371 – 377, 2002.

[4] D. A. B. Miller, “Rationale and challenges for optical interconnects to electronic chips,” *Proceedings of the IEEE*, vol. 88, no. 6, pp. 728–749, 2000.

[5] E. N. Shauly, “Physical, electrical, and reliability considerations for copper beol layout design rules,” *J. Low Power Electronics and Applications*, vol. 8, no. 20, pp. 1–33, 2018.

[6] J. W. Goodman, F. J. Leonberger, Sun-Yuan Kung, and R. A. Athale, “Optical interconnections for VLSI systems,” *Proceedings of the IEEE*, vol. 72, no. 7, pp. 850–866, 1984.

[7] Timothy.J.Drabik, “Balancing electrical and optical interconnection resources at low levels,” *Journal of Optics A: Pure and Applied Optics*, vol. 1, no. 2, pp. 330–332, 1999.

[8] M. R. Feldman, S. C. Esener, C. C. Guest, and S. H. Lee, “Comparison between optical and electrical interconnects based on power and speed considerations,” *Applied Optics*, vol. 27, no. 9, pp. 1742–1751, 1988.

[9] A. Husain, “Optical interconnect of digital integrated circuits and systems,” *SPIE proceedings*, vol. 466, no. 2, pp. 10–20, 1984.

[10] R.-T. GU, Y.-J. QIAO, and Y.-F. JI, “Chip-to-chip optical interconnects: more bandwidth, more powerful,” *The Journal of China Universities of Posts and Telecommunication*, vol. 16, no. 1, pp. 1 – 5, 2009.

[11] C. Li, R. Bai, A. Shafik, E. Z. Tabasy, and e. B Wang, “Silicon photonic transceiver circuits with microring resonator bias-based wavelength stabilization in 65 nm cmos,” *IEEE Journal of Solid-State Circuits*, vol. 49, no. 6, pp. 1419–1436, 2014.

[12] J. Hammer, *"Modulation and switching of light in dielectric waveguides"*, 1975, vol. 7, pp. 139–200.

[13] Ballabio, A., Bietti, S., Scaccabarozzi, A. et al., “GaAs epilayers grown on patterned (001) silicon substrates via suspended Ge layers,” *Sci Rep*, vol. 9, no. 17529, pp. 1–8, 2019.

[14] Y. Bolkhovityanov and O. Pchelyakov, “GaAs epitaxy on Si substrates: Modern status of research and engineering,” *Physics-Uspekhi*, vol. 51, p. 437, 2008.

[15] G. Li, X. Zheng, J. Yao, H. Thacker, I. Shubin, Y. Luo, K. Raj, J. E. Cunningham, and A. V. Krishnamoorthy, “High-efficiency 25Gb/s CMOS ring modulator with integrated thermal tuning,” *8th IEEE International Conference on Group IV Photonics*, pp. 8–10, 2011.

[16] Q. Xu, S. Manipatruni, B. Schmidt, J. Shakya, and M. Lipson, “12.5 Gbit/s carrier-injection-based silicon micro-ring silicon modulators,” *Opt. Express*, vol. 15, pp. 430–436, 2007.

[17] Q. Xu, B. Schmidt, J. Shakya, and M. Lipson, “Cascaded silicon micro-ring modulators for WDM optical interconnection,” *Opt. Express*, vol. 14, no. 20, pp. 9431–9436, 2006.

[18] Z. Zhou, B. Yin, and J. Michel, “On-chip light sources for silicon photonics,” *Light: Science and Applications*, vol. 4, pp. 1–13, 2015.

[19] J. Liu, X. Sun, R. Camacho-Aguilera, L. C. Kimerling, and J. Michel, “Ge-on-si laser operating at room temperature,” *Opt. Lett.*, vol. 35, no. 5, pp. 679–681, 2010.

[20] E. A. J. Marcatili, "Bends in optical dielectric guides," *The Bell System Technical Journal*, vol. 48, no. 7, pp. 2103–2132, 1969.

[21] G. R. Dominik, *Ring Resonators: Theory and Modeling*. Integrated Ring Resonators, Springer, 2007.

[22] R. Haldar, S. Das, and S. K. Varshney, "Theory and design of off-axis microring resonators for high-density on-chip photonic applications," *Journal of Lightwave Technology*, vol. 31, no. 24, pp. 3976–3986, 2013.

[23] B. E. Little, S. T. Chu, H. A. Haus, J. Foresi, and J. Laine, "Microring resonator channel dropping filters," *Journal of Lightwave Technology*, vol. 15, no. 6, pp. 998–1005, 1997.

[24] Y. Liu, T. Chang, and A. Craig, "Coupled mode theory for modeling microring resonators," *Optical Engineering - OPT ENG*, vol. 44, no. 08, pp. 1–6, 2005.

[25] P. Saeung and P. Yupapin, "Vernier effect of multiple-ring resonator filters modeling by a graphical approach," *Optical Engineering - OPT ENG*, vol. 46, pp. 1–6, 2007.

[26] C. Chinda, P. Yupapin, and S. Prajak, "The serially coupled multiple ring resonator filters and vernier effect," *Optica Applicata*, vol. 39, 2009.

[27] G. N. de Brabander, J. T. Boyd, and G. Beheim, "Integrated optical ring resonator with micromechanical diaphragms for pressure sensing," *IEEE Photonics Technology Letters*, vol. 6, no. 5, pp. 671–673, 1994.

[28] H. T. Kim and M. Yu, "Cascaded ring resonator-based temperature sensor with simultaneously enhanced sensitivity and range," *Opt. Express*, vol. 24, no. 9, pp. 9501–9510, 2016.

[29] A. Jian, L. Zou, H. Tang, Q. Duan, J. Ji, Q. Zhang, X. Zhang, and S. Sang, "Theoretical analysis of microring resonator-based biosensor with high resolution and free of temperature influence," *Optical Engineering*, vol. 56, no. 06, pp. 1–6, 2017.

[30] Y. Sun and X. Fan, "Optical ring resonators for biochemical and chemical sensing," *Analytical and bioanalytical chemistry*, vol. 399, no. 10, pp. 205–11, 2010.

[31] G. Lenz, B. J. Eggleton, C. K. Madsen, and R. E. Slusher, "Optical delay lines based on optical filters," *IEEE Journal of Quantum Electronics*, vol. 37, no. 4, pp. 525–532, 2001.

[32] E. Garmire, “Semiconductor components for monolithic applications,” in *Integrated Optics(T. Tamir ed.)*. Springer-Verlag, New York, 1975.

[33] T. S. El-Bawab, in *Optical Switching*. Springer, 2006.

[34] B. R. Bennett, R. A. Soref, and J. A. Del Alamo, “Carrier-induced change in refractive index of InP, GaAs and InGaAsP,” *IEEE Journal of Quantum Electronics*, vol. 26, no. 1, pp. 113–122, 1990.

[35] F. Ito, M. Matsuura, and T. Tanifuji, “A carrier injection type optical switch in gaas using free carrier plasma dispersion with wavelength range from 1.06 to 1.55 mu m,” *IEEE Journal of Quantum Electronics*, vol. 25, no. 7, pp. 1677–1681, 1989.

[36] D. A. B. Miller, D. S. Chemla, T. C. Damen, A. C. Gossard, W. Wiegmann, T. H. Wood, and C. A. Burrus, “Electric field dependence of optical absorption near the band gap of quantum-well structures,” *Phys. Rev. B*, vol. 32, pp. 1043–1060, 1985.

[37] P. J. Stevens, M. Whitehead, G. Parry, and K. Woodbridge, “Computer modeling of the electric field dependent absorption spectrum of multiple quantum well material,” *IEEE Journal of Quantum Electronics*, vol. 24, no. 10, pp. 2007–2016, 1988.

[38] G. lengyel, K. W. Jelley, and R. W. H. Engelmann, “A semi-empirical model for electroabsorption in gaas/algaas multiple quantum well modulator structures,” *IEEE Journal of Quantum Electronics*, vol. 26, no. 2, pp. 296–304, 1990.

[39] J. F. Lampin, L. Desplanque, and F. Mollot, “Detection of picosecond electrical pulses using the intrinsic franz–keldysh effect,” *Applied Physics Letters*, vol. 78, no. 26, pp. 4103–4105, 2001.

[40] M. E. Chin and W. S. C. Chang, “Theoretical design optimization of multiple-quantum-well electroabsorption waveguide modulators,” *IEEE Journal of Quantum Electronics*, vol. 29, no. 9, pp. 2476–2488, 1993.

[41] T. H. Wood, “Multiple quantum well (mqw) waveguide modulators,” *Journal of Lightwave Technology*, vol. 6, no. 6, pp. 743–757, 1988.

[42] Z. T. S. R. Olsen, G.H. and E. Bertin, “Ingaasp quaternary alloys: Composition, refractive index and lattice mismatch,” *Journal of Electronic Materials*, vol. 9, pp. 977–987, 1980.

[43] N. Dagli, “Wide-bandwidth lasers and modulators for rf photonics,” *IEEE Transactions on Microwave Theory and Techniques*, vol. 47, no. 7, pp. 1151–1171, 1999.

[44] S. Ravindran, K. Alameh, and Y. T. Lee, “Design and analysis of electroabsorptive quantum well based double ring resonators for wavelength switching applications,” *Opt Quant Electron*, vol. 41, pp. 635–644, 2009.

[45] M. K. Chin, P. K. L. Yu, and W. S. C. Chang, “Optimization of multiple quantum well structures for waveguide electroabsorption modulators,” *IEEE Journal of Quantum Electronics*, vol. 27, no. 3, pp. 696–701, 1991.

[46] T. Hiroshima, “Electric field induced refractive index changes in $gaas - al_x ga_{1-x} as$ quantum wells,” *Applied Physics Letters*, vol. 50, pp. 968–970, 1987.

[47] L. Redaelli, A. Mukhtarova, S. Valdueza-Felip, A. Ajay, C. Bougerol, C. Himwas, J. Faure-Vincent, C. Durand, J. Eymery, and E. Monroy, “Effect of the quantum well thickness on the performance of ingan photovoltaic cells,” *Applied Physics Letters*, vol. 105, no. 13, p. 131105, 2014.

[48] J. Hardy and J. Shamir, “Optics inspired logic architecture,” *Opt. Express*, vol. 15, no. 1, pp. 150–165, 2007.

[49] R. Soref, “Reconfigurable integrated optoelectronics,” *Advances in OptoElectronics*, vol. 2011, no. 01, pp. 1–15, 2011.

[50] L. Zhang, J. Ding, Y. Tian, R. Ji, L. Yang, H. Chen, P. Zhou, Y. Lu, W. Zhu, and R. Min, “Electro-optic directed logic circuit based on microring resonators for xor/xnor operations,” *Opt. Express*, vol. 20, no. 11, pp. 11 605–11 614, 2012.

[51] Y. Tian, Z. Liu, H. Xiao, G. Zhao, G. Liu, and et al., “Experimental demonstration of a reconfigurable electro-optic directed logic circuit using cascaded carrier-injection micro-ring resonators,” *Scientific Reports*, vol. 7, no. 6410, pp. 1–10, 2017.

[52] A. Kumar, M. Kumar, S. K. Jindal, and S. K. Raghuwanshi, “Implementation of all-optical active low/high tri-state buffer logic using the micro-ring resonator structures,” *Opt Quant Electron*, vol. 51, no. 191, pp. 1–18, 2019.

[53] L. Shen, H. H. Wieder, and W. S. C. Chang, “Electroabsorption modulation at 1.3 μm on GaAs substrates using a step-graded low temperature grown InAlAs buffer,” *IEEE Photonics Technology Letters*, vol. 8, no. 3, pp. 352–354, 1996.

[54] H. Thapliyal, N. Ranganathan, and S. Kotiyal, *Reversible Logic Based Design and Test of Field Coupled Nanocomputing Circuits in Field-Coupled Nanocomputing, Springer*, 2014, vol. 8280, pp. 133–172.

[55] J. Shamir, H. J. Caulfield, W. Micelli, and R. J. Seymour, "Optical computing and the fredkin gates," *Appl. Opt.*, vol. 25, no. 10, pp. 1604–1607, 1986.

[56] Y. Tian, L. Zhang, R. Ji, L. Yang, P. Zhou, H. Chen, J. Ding, W. Zhu, Y. Lu, L. Jia, Q. Fang, and M. Yu, "Proof of concept of directed or/nor and and/nand logic circuit consisting of two parallel microring resonators," *Opt. Lett.*, vol. 36, no. 9, pp. 1650–1652, 2011.

[57] A. Kumar, S. Kumar, and S. K. Raghuwanshi, "Implementation of xor/xnor and and logic gates by using mach–zehnder interferometers," *Applied Physics Letters*, vol. 125, pp. 5764 – 5767, 2014.

[58] F. K. A and S. R. et al., "Advanced realization and characterization of directed optical logic gates using electroabsorptive quantum-well-based micro ring resonator," *Optik*, vol. 221, p. 164426, 2020.

[59] K. Ishida, H. Nakamura, H. Matsumura, T. Kadoi, and H. Inoue, "Ingaasp/inp optical switches using carrier induced refractive index change," *Appl. Phys. Letter*, vol. 50, pp. 141–142, 1987.

[60] S. Abdalla, S. Ng, P. Barrios, D. Celo, A. Delage, S. El-Mougy, I. Golub, J. . He, S. Janz, R. McKinnon, P. Poole, S. Raymond, T. J. Smy, and B. Syrett, "Carrier injection-based digital optical switch with reconfigurable output waveguide arms," *IEEE Photonics Technology Letters*, vol. 16, no. 4, pp. 1038–1040, 2004.

[61] B. Bennett and R. Soref, "Electrorefraction and electroabsorption in InP, GaAs, GaSb, InAs, and InSb," *IEEE Journal of Quantum Electronics*, vol. 23, no. 12, pp. 2159–2166, 1987.

[62] F. Koyama and K. Iga, "Frequency chirping in external modulators," *Journal of Lightwave Technology*, vol. 6, no. 1, pp. 87–93, 1988.

[63] Z. K. Ioannidis, P. M. Radmore, and I. P. Giles, "Dynamic response of an all-fiber ring resonator," *Opt. Lett.*, vol. 13, no. 5, pp. 422–424, 1988.

[64] J. W. Park, S. Park, and G. Kim, “Transient analysis of static and dynamic responses for a single ring-resonator-based wdm add/drop filter array,” *Optical and Quantum electronics*, vol. 44, pp. 731–740, 2012.

[65] J. Diaz Reyes, J. Cardona Bedoya, M. Gomez Herrera, J. Herrera, I. Riech, and J. Mendoza Alvarez, “Optical properties of tellurium-doped $\mathrm{In}_x\mathrm{Ga}_{1-x}\mathrm{As}_y\mathrm{Sb}_1 - y$ epitaxial layers studied by photoluminescence spectroscopy,” *Journal of Physics: Condensed Matter*, vol. 15, pp. 8941–8948, 2003.

[66] J. Baliga, “P-i-n rectifiers,” in *Fundamentals of Power Semiconductor Devices*. Springer Science, 2008.

[67] D. Arnov and R. Mamatkulov, “On the theory of transient process after reversal of p-i-n diode current from forward to reverse direction (i),” *physica status solidi (a)*, vol. 15, pp. 351–359, 2006.

[68] W. D. Sacher and J. K. S. Poon, “Dynamics of microring resonator modulators,” *Opt. Express*, vol. 16, pp. 15 741–15 753, 2008.

List of Publications

Published journal papers

1. Fayza K. A, Sooraj Ravindran, Kwangwook Park, Kamal Alameh, Aylin Bengi, Hajara A. V, Yong Tak Lee, *Advanced Realization and Characterization of Directed Optical Logic gates using Electroabsorptive Quantum-Well-based Micro Ring Resonator*, **Optik**, Elsevier, Volume 221, November 2020.
2. Fayza Kizhakkakath, Sooraj Ravindran, Kwangwook Park, Kamal Alameh, Yong Tak Lee, *Realization and Optimization of Optical Logic Gates using Bias Assisted Carrier-Injected Triple Parallel Microring Resonators*, **Results in Optics**, Elsevier, Volume 4, August 2021.
3. Fayza Kizhakkakath, Sooraj Ravindran, *Microring Resonator based Optical Logic Gates*, **Journal of Micro and Smart Systems**, Springer, June 2022.

Conference papers and posters

1. Fayza K. A, Sooraj Ravindran, *Transient Analysis of GaAs based Single MRR Modulator with CI as Modulating Mechanism* at **SOAP 2018**, IISc Bangalore.
2. Fayza K. A, Sooraj Ravindran, *Design optimization of QCSE based ring resonator optical switches* at **ISSMD 2018**, VNIT, Nagpur.
3. Fayza K. A, Sooraj Ravindran, *Variable optical true time delay using cascaded resonator switching activated EA for satellite communication* at **ICSS 2019**, RCI, Hyderabad.
4. Fayza K. A, Sooraj Ravindran, *Parametric Optimization studies on Quantum Confined Stark effect based Microring Resonator Optical Switches* at **SOAP 2019**, IISc Bangalore.